AD-A112 373 OHIO STATE UNIV COLUMBUS ELECTROSCIENCE LAB F/G 9/5
ELEVATION PLANE ANALYSIS OF ON-AIRCRAFT ANTENNAS.(U)
JAN 82 C L YU, W D BURNSIDE N62269-71-C-0296
UNCLASSIFIED ESL-3188-2 NL

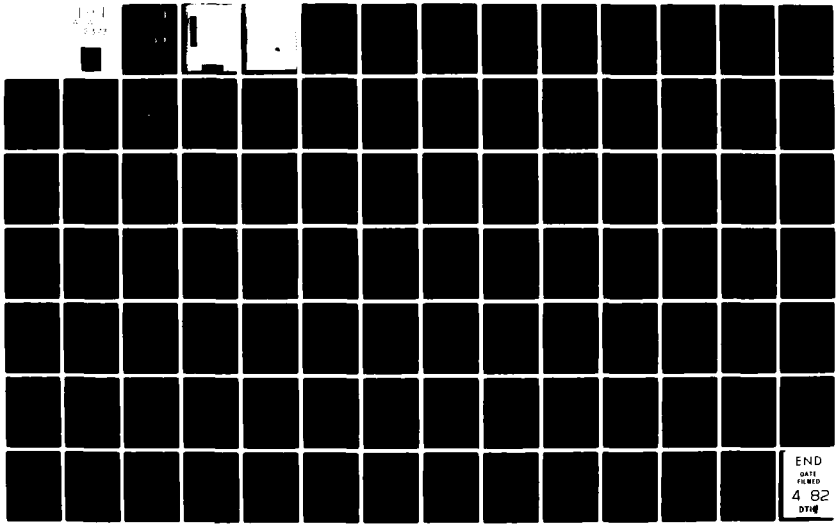

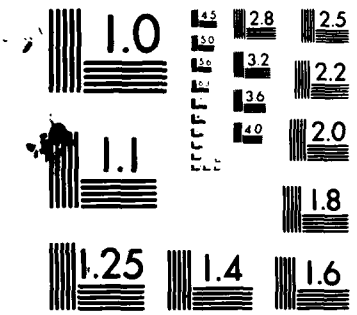

MICROCOPY RESOLUTION TEST CHART
NATIONAL BUREAU OF STANDARDS 1963 A

PHOTOGRAPH THIS SHEET

A112373

DTIC ACCESSION NUMBER

II

LEVEL

INVENTORY

Ohio State Univ., Columbus
ElectroScience Lab.

Elevation Plane Analysis of On-Aircraft Antenns.

DOCUMENT IDENTIFICATION

Jan. 72
ElectroScience Lab. No. 3188-2
Contract N62269-71-C-0296

DISTRIBUTION STATEMENT A
Approved for public release;
Distribution Unlimited

DISTRIBUTION STATEMENT

ACCESSION FOR		
NTIS	GRA&I	☒
DTIC	TAB	☐
UNANNOUNCED		☐
JUSTIFICATION		
Per ltr. on file (FL-88, Acq.# 82-0023, dtd 26 Jan. 82)		
BY		
DISTRIBUTION /		
AVAILABILITY CODES		
DIST	AVAIL AND/OR SPECIAL	
A		

DISTRIBUTION STAMP

DTIC COPY INSPECTED 2

DTIC
ELECTE
S MAR 24 1982 D
D

DATE ACCESSIONED

82 03 20 061

DATE RECEIVED IN DTIC

PHOTOGRAPH THIS SHEET AND RETURN TO DTIC-DDA-2

DTIC FORM OCT 79 70A

DOCUMENT PROCESSING SHEET

AD A112373

ELEVATION PLANE ANALYSIS OF ON-AIRCRAFT ANTENNAS

Chong L. Yu and Walter D. Burnside

TECHNICAL REPORT 3188-2

January 1972

Contract N62269-71-C-0296

Naval Air Development Center
Warminster, Pa. 18974

ABSTRACT

The radiation patterns, in the elevation plane, of airborne antennas mounted on the aircraft fuselage have been analyzed by modern diffraction theory including wedge diffraction theory and creeping wave theory. It is found that the fuselage shape has a dominant effect on the elevation patterns. In order to analyze a general convex shape, a new approach, "section matching method", has been developed in which the fuselage profile is described by a set of points.

This new method is applied to some general geometrical shapes which approximate aircraft fuselage. The composite elliptical cylinder is the most general model considered. The validity of this method has been verified by modal and more rigorous GTD solutions.

TABLE OF CONTENTS

		Page
I.	INTRODUCTION	1
II.	THEORETICAL BACKGROUND	2
	A. Wedge Diffraction Analysis	2
	B. Creeping Wave Analysis	13
III.	ELEVATION PATTERNS FOR SIMPLE FUSELAGE MODELS	18
IV.	ELEVATION PATTERNS FOR GENERAL FUSELAGE MODELS	41
	A. GTD Solution For General Fuselage Models	43
	B. Section Matching Method	51
V.	CONCLUSION	84
REFERENCES		86

I. INTRODUCTION

It is well known that the performance of airborne antenna systems is often affected by the aircraft structure. It is the distortion of the antenna patterns by various structures which is the primary consideration in this report and specifically the effect in the elevation plane. Based on crude models for the aircraft with the antenna mounted on the fuselage, it is found that in the elevation plane the shape of the fuselage has the greatest effect. Thus the main concern in this study is analyzing the effect of the aircraft fuselage on the radiation patterns in the elevation plane.

Modern diffraction theory including wedge diffraction theory and creeping wave theory, which are the extensions of the geometrical theory of diffraction (GTD), is used to analyze the radiation patterns of aircraft antenna systems in the elevation plane. This theory provides an excellent method for calculating the scattering effects of practical structures such as aircraft fuselages in terms of ray optics. This approach allows one to consider a complicated problem in terms of simpler component parts.

First some simple basic models are used to simulate the fuselage such that wedge diffraction techniques can be applied directly to analyze the radiation patterns. In order to introduce the curvature of the actual fuselage, the theoretical models are modified to include curved surfaces. Then a combination of the wedge diffraction technique and creeping wave theory is employed to solve these new problems.

In order to include a more general geometry, a new approach is developed in which the fuselage cross-section is described by a set of points to give a good representation of the actual fuselage. Using this "section matching method" the elevation plane radiation patterns of general airborne antennas such as circumferential slot, axial slot, and monopole are computed. This general method (computer solution) can be applied to any convex body which can be described adequately by a finite number of points.

II. THEORETICAL BACKGROUND

The theoretical technique used to analyze the effect of the aircraft structure on the patterns of antennas mounted on the fuselage is basically a high frequency asymptotic analysis termed "The Geometrical Theory of Diffraction (GTD)". This theory was originated by Keller[1] and extensions by Kouyoumjian,[2] Rudduck[3], and Ryan[4] include wedge diffraction theory and creeping wave analysis. The radiation patterns of antennas mounted on an aircraft fuselage composed of sections of cones and cylinders may be obtained and analyzed by various combinations of these techniques. Since the far field radiation pattern in the elevation plane is of main interest, only the far field form of the electromagnetic waves is considered in this study.

A. Wedge Diffraction Analysis

The basic shapes used to represent the aircraft fuselage are cones and cylinders which, in our two dimensional profile analysis, reduce to a wedge type geometry. Thus wedge diffraction analyses can be employed to analyze the radiated fields in the elevation plane. The diffraction of a plane wave by a conducting wedge was first solved by Sommerfeld.[5] An asymptotic series for the diffraction function (V_B) was introduced by Pauli[6] as a practical formulation to the solution for an arbitrary finite-angle conducting wedge. Recently, Hutchins and Kouyoumjian[7,8] obtained a formulation for the diffraction function (V_B), which significantly improves the accuracy over that of Pauli. The improved form of diffraction function for a wedge defined by [$(2-n)\pi = WA$] is given by (see Fig. 1)

$$V_B(\rho,\theta) = I_{-\pi}(\rho,\theta) + I_{+\pi}(\rho,\theta) \tag{1}$$

where (ρ,θ) is the field point and

$$(2) \qquad I_{\pm\pi}(\rho,\theta) \sim \frac{e^{-j(k\rho+\frac{\pi}{4})}}{jn\sqrt{2\pi}} \sqrt{a}\, \cot\left(\frac{\pi\pm\theta}{2n}\right) \cdot e^{jk\rho a}$$

$$\int_{(k\rho a)^{1/2}}^{\infty} e^{-j\tau^2}\, d\tau + \text{higher order terms.}$$

With

$$(3) \qquad a = 1 + \cos(\theta - 2n\pi N)$$

and N is a positive or negative integer or zero whichever most nearly satisfies the equations

$$(4) \qquad \left.\begin{array}{ll} 2n\pi N - \theta = -\pi & \text{for } I_{-\pi} \\ 2n\pi N - \theta = +\pi & \text{for } I_{+\pi} \end{array}\right\} .$$

Equation (2) contains the leading terms plus higher order terms which are negligible for large values of $k\rho$. For large values of $k\rho a$, Eq. (2) reduces to the form

$$(5) \qquad V_B(\rho,\theta) = \frac{e^{-j(k\rho+\frac{\pi}{4})}}{\sqrt{2\pi k\rho}} \; \frac{\frac{1}{n}\sin\left(\frac{\pi}{n}\right)}{\cos\left(\frac{\pi}{n}\right) - \cos\left(\frac{\theta}{n}\right)}$$

$$= D(\theta)\, \frac{e^{-jk\rho}}{\sqrt{\rho}} = R(\theta)\, \frac{e^{-j(k\rho+\frac{\pi}{4})}}{\sqrt{2\pi k\rho}}$$

where $D(\theta)$ is diffraction coefficient and $R(\theta)$ is the diffracted ray which is given by

$$(6) \qquad R(\theta) = \frac{\frac{1}{n}\sin\left(\frac{\pi}{n}\right)}{\cos\left(\frac{\pi}{n}\right) - \cos\left(\frac{\theta}{n}\right)} \quad .$$

The improved diffraction function has been programmed into a digital computer subroutine for numerical calculations.

The basic wedge diffraction problem is illustrated in Fig. 1.

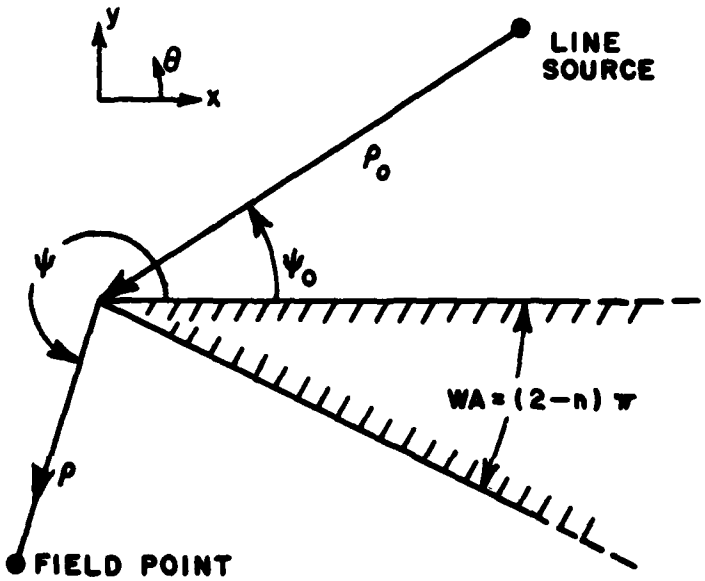

Fig. 1. Basic wedge diffraction geometry.

With a line source located at (ρ_0, ψ_0) with respect to the wedge tip, the far field form of the diffracted field is given by

$$(7) \qquad U_D\ (\rho,\theta) = U_S^i\ [V_B\ (\rho_0, \psi-\psi_0, n) \pm V_B\ (\rho_0, \psi+\psi_0, n)]$$

where (ρ,θ) is the far field observation point and n is related to the wedge angle by $WA = (2-n)\pi$. Note that the diffraction function V_B has been applied via reciprocity to this line source of cylindrical

waves at the antenna location. The relationship between the ray $R(\theta)$ and the field value $U(\rho,\theta)$ is given in Reference [3] by

$$U(\rho,\theta) = R(\theta)\,\frac{e^{-j(k\rho+\frac{\pi}{4})}}{\sqrt{2\pi k\rho}} \quad . \tag{8}$$

Thus, in terms of the ray form, Eq. (7) can be rewritten as

$$R_D(\theta) = R_S^i\,[V_B\,(\rho_o,\psi-\psi_o,n) \pm V_B(\rho_o,\psi+\psi_o,n)] \tag{9}$$

with V_B given by Eq. (5).

Notice that the plus sign applies for the polarization of the electric field perpendicular to the edge with the boundary condition

$$\left(\frac{\partial\overline{E}}{\partial n}\bigg|_{\text{wedge}}\right) = 0 \tag{10}$$

and the minus sign applies for polarization parallel to the edge with the boundary condition

$$\left(\overline{E}\bigg|_{\text{wedge}}\right) = 0 \ . \tag{11}$$

The total field is then, using the superposition principle, the sum of the diffracted and geometrical optics terms. Note that in Fig. 1 cylindrical coordinates are employed with the z-axis coincident with the edge and consequently normal to the plane of diffraction, hence the z-component of the total field is represented by the scalar function U. Note also that the time dependence factor ($e^{j\omega t}$) is suppressed throughout the analysis.

It has been shown in Reference [9] that the radiation patterns in the elevation plane based on the two dimensional analysis would not be adequate for an antenna mounted on finite three-dimensional surfaces, if the effects of discontinuities such as wedge-type

junctions and tips of realistic models are not handled with sufficient accuracy. Hence, the diffraction by curved edges must be introduced in order to adequately analyze the diffraction effects of the cone-cylinder and finite cylinder junctions.

The effects of edge curvature on the behavior of diffracted rays can be described using an extension of Fermat's principle, "A singly diffracted ray connecting two points is a curve whose length is stationary among all curves connecting these two points and having one point on the edge."[1] By applying conservation of energy within the astigmatic energy flux tube of diffracted rays depicted in Fig. 2,

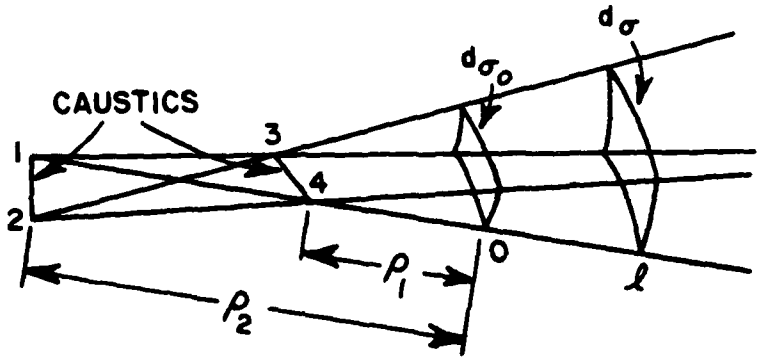

Fig. 2. An astigmatic ray tube.

one obtains the relation

$$A_o^2 d\sigma_o = A^2 d\sigma = \text{constant} \tag{12}$$

where $d\sigma_o$ is the cross section of the flux tube at reference point O, having principal radii of curvature ρ_1 and ρ_2; and $d\sigma$ is the cross section at ℓ, having principal radii of curvature $\rho_1 + \ell$ and $\rho_2 + \ell$. A_o and A are the field amplitudes of the diffracted rays at point O and ℓ. It follows from elementary geometry that

$$\frac{d\sigma_o}{d\sigma} = \frac{(\rho_1+\ell)(\rho_2+\ell)}{\rho_1\rho_2} \quad . \tag{13}$$

Inserting this result into Eq. (12), yields

$$\frac{A}{A_o} = \sqrt{\frac{\rho_1\rho_2}{(\rho_1+\ell)(\rho_2+\ell)}} \tag{14}$$

or

$$A = A_o\sqrt{\frac{\rho_1\rho_2}{(\rho_1+\ell)(\rho_2+\ell)}} \ . \tag{15}$$

This is the equation which governs the behavior of all rays (incident, reflected or diffracted). The expression

$$\sqrt{\frac{\rho_1\rho_2}{(\rho_1+\ell)(\rho_2+\ell)}}$$

is the spatial attenuation factor or "ray divergence factor, (RDF)".

It is interesting to note that, when $\ell = -\rho_1$ or $-\rho_2$, the field amplitude becomes infinite and the ray optics field is invalid. The congruence of rays at the lines 1-2, 3-4 is called a caustic. It has been demonstrated that in the region away from the caustics the GTD solution is correct if a phase shift of $(-\pi/2)$ is introduced upon traversal in the direction of propagation through a caustic line.

Now consider the rays from a line source incident on a curved surface as shown in Fig. 3. It is known that if the incident rays strike the edge obliquely, making an angle β with the curved edge, the diffracted rays lie on the surface of a cone whose half angle is equal to β.[10] It is clear that one of the caustics is at the edge and the other one is located at a distance ρ from the edge. The distance ρ between the edge caustic and the second caustic can be found according to Kouyoumjian[11] by

$$\frac{1}{\rho} = \frac{1}{\ell} - \frac{\hat{n}\cdot(\hat{i}-\hat{d})}{\rho_Q \sin^2\beta} \tag{16}$$

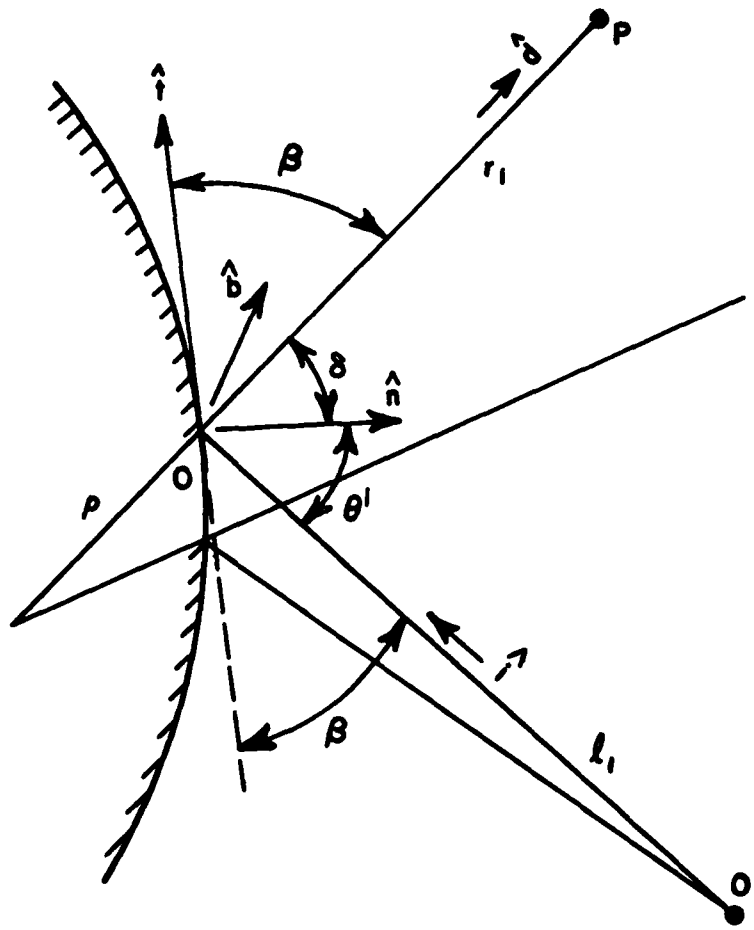

Fig. 3. Vector relations for diffraction by a curved surface.

where

ρ_Q = the radius of curvature of the edge at Q

$\hat{i}$, $\hat{d}$ = directions of incidence and diffraction

$\hat{n}$ = the normal vector of the edge .

The angle β is easily found as

(17) $\cos\beta = \hat{i} \cdot \hat{t} \qquad 0 \leq \beta \leq \pi$

where $\hat{t}$ is the tangent vector of the edge with the tangent and normal vectors in the plane of the figure. Note that the angles θ' and δ are given by

(18) $-\sin\theta' = \hat{i} \cdot \hat{n} \qquad -\pi/2 \leq \theta' \leq 3\pi/2$

(19) $\cos\delta = \hat{d} \cdot \hat{n} \qquad -\pi \leq \delta \leq \pi.$

Equation (16) in combination with ray optics allows the determination of the effects of edge curvature upon the diffracted rays.

Figure 4 illustrates the diffraction of a "tube" of rays

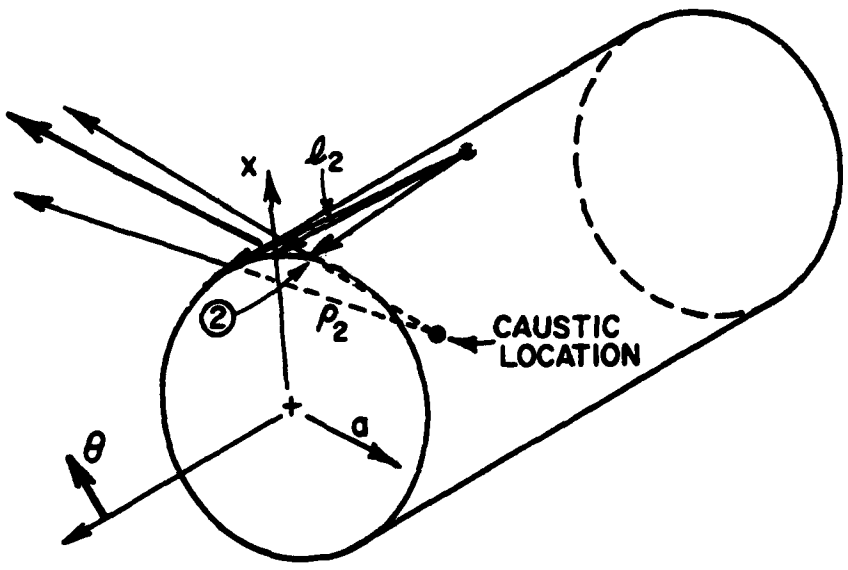

Fig. 4. Diffraction by the end of a finite circular cylinder.

originating on the surface of the cylinder at the antenna location and which propagate to the end of the cylinder. The caustic distance

of these diffracted rays is given by Eq. (16). Applying Eq. (16) we obtain

$$\frac{1}{\rho_2} = \frac{1}{\ell_2} + \frac{\sin\theta}{a}, \tag{20}$$

where ρ_2 is the caustic distance, as illustrated in Fig. 4. One notices that the above equation predicts that the caustic distance is infinite for values of $\theta = \theta_c = \sin^{-1}(\frac{-a}{\ell_2})$ such that

$$\frac{1}{\rho_2} = \frac{a + \ell_2 \sin\theta_c}{a\,\ell_2} = 0 . \tag{21}$$

A similar expression can be derived for planes removed from the $\phi = 0$ plane, in which case the caustic distance is dependent upon both θ and ϕ. However, only the $\phi = 0$ plane is of interest in this study. Note that for $\theta < \theta_c$ the caustic distance ρ_2 becomes negative in sign. This caustic is shown in Fig. 5. The significance of the negative value of ρ_2 is that the diffracted rays pass through the caustic location before proceeding to the far field.

The diffracted field from 2 can be calculated by using ray optics, conservation of energy, and wedge diffraction theory. The form of the three dimensional field incident upon the edge is given approximately by

$$H_\phi^i = H_o\, F(\theta{=}0,\ \phi{=}0)\, \frac{e^{-jk\ell_2}}{\ell_2} = [H_o\, F(\theta{=}0,\ \phi{=}0)\, \frac{1}{\sqrt{\ell_2}}] \cdot \frac{e^{-jk\ell_2}}{\sqrt{\ell_2}} \tag{22}$$

where $F(\theta,\phi)$ is the far field pattern of the antenna in the direction (θ,ϕ) (see Appendix V in Reference [9].) Note that only the case of the magnetic field tangent to the perfectly conducting cylinder is considered here since the boundary condition on the perfectly conducting surface requires that the tangential electric field vanishes

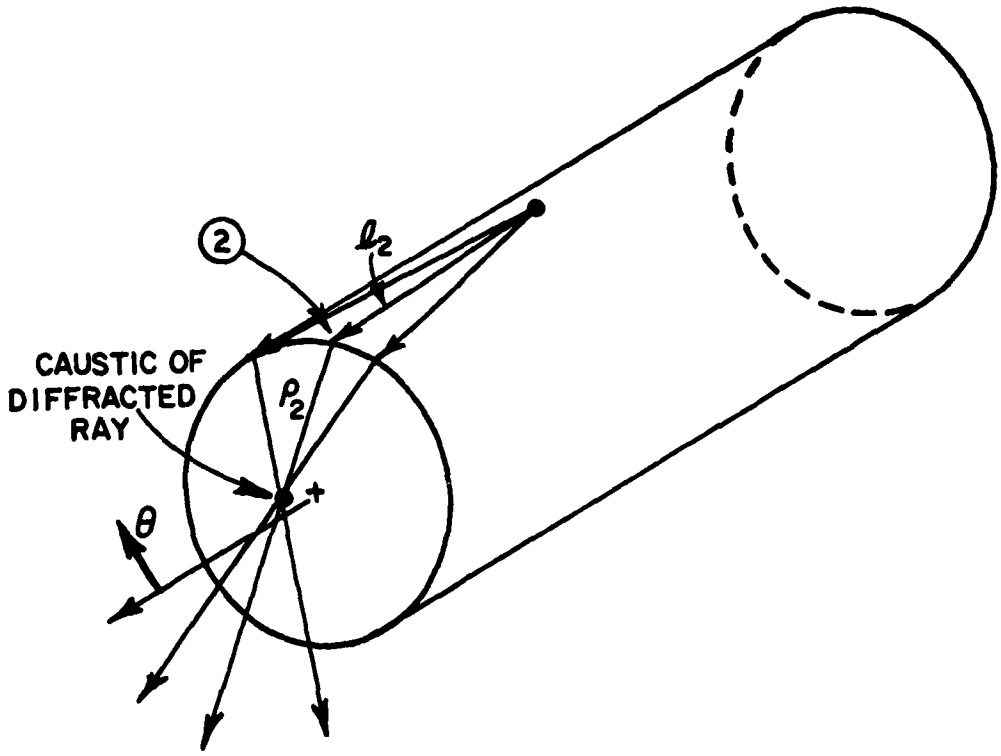

Fig. 5. Caustic caused by the intersection of the diffracted rays.

on the surface, precluding the propagation of a tangential electric field. The factor

$$\frac{e^{-jk\ell_2}}{\sqrt{\ell_2}}$$

outside the brackets in Eq. (22) corresponds to the form of the incident cylindrical wave field for which the two dimensional diffraction function $V_B(\ell_2, \pi-\theta, n_2)$ accounts for the diffraction by the discontinuity in the $\phi=0$ plane. This

$$\frac{e^{-jk\ell_2}}{\sqrt{\ell_2}}$$

field dependence is contained in the functional expression for $V_B(\ell_2, \pi-\theta, n_2)$ and thus this factor appears implicitly when V_B is used. The diffracted magnetic field $H_{\phi 2}^{(1)}$, is now expressed using the wedge diffraction coefficient and ray optics as

$$(23) \qquad H_{\phi 2}^{(1)}(\theta,\phi=0) = [H_o\ F(\theta=0,\ \phi=0)/\sqrt{\ell_2}] \cdot \sqrt{\frac{\rho_2}{\rho_2+r_2}} \cdot V_B(\ell_2,\ \pi-\theta\ n_2) \cdot \frac{e^{-jkr_2}}{\sqrt{r_2}} .$$

The ray divergence factor

$$\sqrt{\frac{\rho_2}{(\ell_2+r_2)}}$$

accounts for the divergence (or convergence) of the diffracted rays in the plane which contains the ray path and is orthogonal to the $\phi=0$ plane. Inserting the expression ρ_2 into this square root gives

$$(24) \qquad RDF_2 = \sqrt{\frac{\rho_2}{(\rho_2+r_2)}} = \sqrt{\frac{a\ell_2}{a\ell_2+r_2(a+\ell_2\sin\theta)}} .$$

In the far field ($r_2 \to \infty$) it becomes

$$(25) \qquad RDF_2 = \sqrt{\frac{a\ell_2}{r_2(a+\ell_2\sin\theta)}} .$$

It is apparent that for $\theta \to \theta_c$, Eq. (25) is singular. Radiation at the angle $\theta=\theta_c$ at which the ray optics picture fails, produces a caustic of the diffracted rays in the far field. This caustic has the form of a parallel "bundle" of diffracted rays. The diffracted field in the caustic region can be analyzed by the equivalent diffraction

currents technique[4] which is outside the scope of this study. Thus, only the ray divergence factor in the illumination region, i.e. $0 \leq \theta \leq \pi$, is encountered in this analysis and that in the shadow region is approximated by the previous expression with θ set equal to π. This approximation gives good results in the prediction of radiation patterns in the elevation plane as will be shown later.

B. Creeping Wave Analysis

When an incident ray strikes a smooth, curved perfectly conducting surface at grazing incidence, i.e., at the shadow boundary, a part of its energy is diffracted into the shadow region. To describe this phenomenon Keller[12] introduced a class of diffracted rays which is now well known as creeping waves. These ray paths include the points Q_1 and Q_2 which form a curve on the diffracting surface. However, the actual concept of creeping waves was introduced by Franz and Depperman.[13,14] A basic creeping wave concept is presented in the following discussion. The context presented below is basically taken from "Asymptotic High-frequency Methods" by Kouyoumjian.[10]

The diffraction by a smooth curved surface is shown in Fig. 6 in which O is the source point and P is the observation point in the shadow region. Applying Fermat's principle, the line OQ_1Q_2P is the shortest distance between O and P which does not penetrate the surface. In detail, a ray incident on the shadow boundary at Q_1 divides; one part of the incident energy continues straight on as predicted by geometrical optics, a second part follows the surface s into the shadow region as a surface ray shedding diffracted rays tangentially as it propagates. With $\hat{t}$, $\hat{n}$ and $\hat{b}$ being the unit vectors in the direction of incidence, normal to the surface s and binormal to the surface ($\hat{b} = \hat{t} \times \hat{n}$), respectively, the incident field $\bar{E}^i(Q_1)$ may be resolved into its normal and tangential components ($\hat{n} \cdot \bar{E}^i(Q_1)$ and $\hat{b} \cdot \bar{E}^i(Q_1)$). It is assumed that these two components induce surface ray fields which propagate independently of each other along the

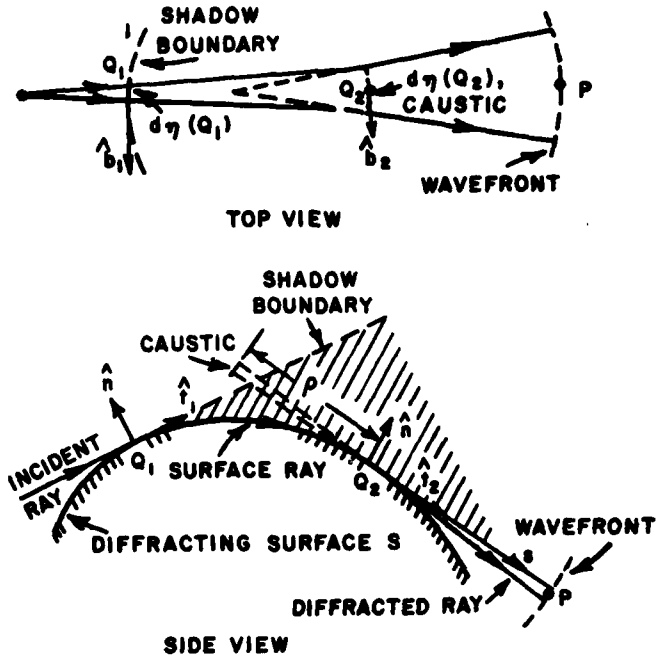

Fig. 6. Diffraction by a smooth curved surface.

geodesic arc between Q_1 and Q_2. From Reference [10] the surface ray field $Ae^{j\phi}$ at Q_1 is related to the incident fields at Q_1 by

$$A(Q_1)\, e^{j\phi(Q_1)} = D_s(Q_1)\, \hat{b}_1 \cdot \bar{E}^i(Q_1) \tag{26}$$

where $D_s(Q_1)$ is the scalar diffraction coefficient for a soft surface. The amplitude of the surface ray is assumed to be governed by the conservation of energy between a pair of adjacent surface rays. Hence, the amplitude behavior of the fields is given as

$$A(Q_2) = A(Q_1) \sqrt{\frac{dn_1}{dn_2}}\; e^{\left[-\int_{Q_1}^{Q_2} \alpha(t')\, dt'\right]} \tag{27}$$

where

dn_1 and dn_2 = the separation between a pair of rays at Q_1 and Q_2, respectively.

$\alpha(t)$ = the attenuation constant which is a function of t, the coordinate along the surface ray, because it depends on the local radius of curvature.

The attenuation constant α is introduced due to the tangential shedding of rays as the surface ray propagates. It is seen from Fig. 6 that Q_2 is a caustic of the diffracted field and the second caustic is located at a distance ρ from Q_2. Thus, the tangential component of the diffracted field which radiates from Q_2 towards P can be found, as in the previous edge diffraction case, with one of the caustics used as a reference point and is given by

$$\hat{b}_2 \cdot \bar{E}^d(P) = D_s(Q_2)\, A(Q_2)\, e^{j\phi(Q_2)} \sqrt{\frac{\rho}{s(\rho+s)}}\; e^{-jks}. \tag{28}$$

From Eqs. (26), (27) and (28) there results

$$\hat{b}_2 \cdot \bar{E}^d(P) = [\hat{b}_1 \cdot \bar{E}^i(Q_1)]\, D_s(Q_1)\, D_s(Q_2) \sqrt{\frac{dn_1}{dn_2}}\; \sqrt{\frac{\rho}{s(\rho+s)}}\; e^{-j\left[k(t+s) + \int_{Q_1}^{Q_2} \alpha(t')\, dt'\right]}. \tag{29}$$

It is found that $\hat{b}_1 \cdot \bar{E}^i(Q_1)$ excites an infinity of surface ray modes each with its own diffraction coefficient and attenuation constant. Thus, the expression in Eq. (29) is replaced by

$$(30) \qquad \hat{b}_2 \cdot \vec{E}^d(P) = [\hat{b}_1 \cdot \vec{E}^i(Q_1)] \sqrt{\frac{d\eta_1}{d\eta_2}} \sqrt{\frac{\rho}{s(\rho+s)}}\, e^{-j[k(t+s)]}$$

$$\left[\sum_m^\infty D_{sm}(Q_1)\, D_{sm}(Q_2)\, e^{-\int_{Q_1}^{Q_2} \alpha_m(t')\, dt'} \right] .$$

Equation (30) relates the diffracted field at P to the incident field at Q_1 for the soft surface boundary condition.

An expression similar to Eq. (30) is also obtained for the normal component of the incident field; in this case, the scalar diffraction coefficients and attenuation constants for the hard surface replace those of the soft surface. Therefore the vector diffracted field at P can be written in terms of the electromagnetic field incident at Q_1 as

$$(31) \qquad \vec{E}^d(P) = [\hat{n}_2\, \hat{n}_1\, v(1,2) + \hat{b}_2\, \hat{b}_1\, u(1,2)] \cdot \vec{E}^i(1) \sqrt{\frac{\rho}{s(\rho+s)}}\, e^{-jks}$$

in which v(1,2), u(1,2) are equal to

$$\sqrt{\frac{d\eta_1}{d\eta_2}}\, e^{-jkt} \sum_m^\infty D_m(1)\, D_m(2)\, e^{-\int_1^2 \alpha_m(t')\, dt'}$$

with the subscripts h, s, respectively, added to D_m and α_m. Note that Q_1 and Q_2 have been replaced by 1 and 2 for the sake of brevity. Finding $d\eta_1$, $d\eta_2$, and ρ is simply a matter of differential geometry involving the rays and surface; this is discussed at length in Levy and Keller.[12] The generalized diffraction coefficient and attenuation constant can be found in Reference [15].

The diffraction thus far discussed is applied to the open curved surface. For a closed surface, each surface ray mode produced

at Q_1 encircles the surface an infinite number of times. The length of the surface ray path for the n-th encirclement is t + nT where T is the circumference of the closed surface. These multiple-encircling rays may be summed to contribute

$$\left[1 - e^{-jkT - \int_0^T \alpha_m(t')\, dt'} \right]$$

to the denominator of the diffracted field. It is interesting to note that there must be another diffraction point Q_3 for the closed surface as shown in Fig. 7. Therefore the field at any point P in the shadow

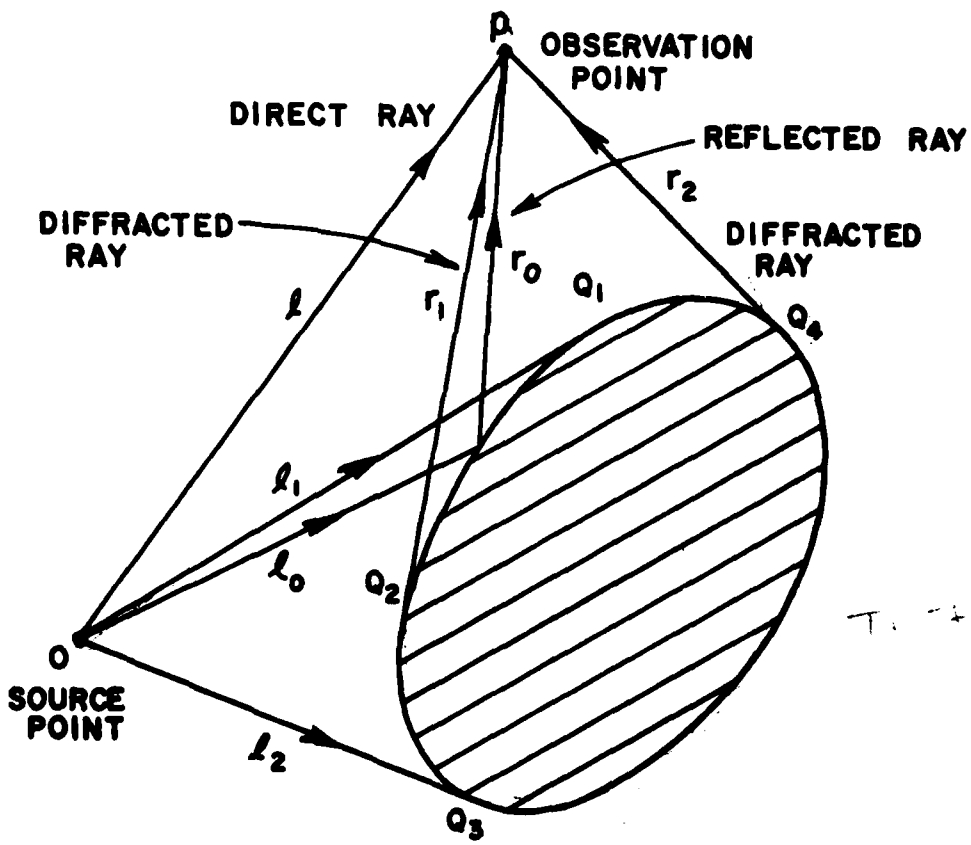

Fig. 7. Diffraction by a smooth closed cylindrical surface.

region is the sum of these two diffracted fields from Q_1 and Q_3. The total field at any point in the illuminated region is, by the superposition principle, the sum of incident, reflected and diffracted field. A detailed discussion of this subject can be found in Reference [15].

III. ELEVATION PATTERNS FOR SIMPLE FUSELAGE MODELS

The fuselage is first approximated by some simple models composed of cylinders, spheres and cones as shown in Fig. 8. These models are simple approximations to the fuselage in which the vertical stabilizer is ignored. More general approximations and the effect of the curvature of aircraft fuselage will be considered in a later section.

Ryan[9] has demonstrated that the radiation pattern of an antenna at an arbitrary location on a finite circular cylinder can be treated as a two-dimensional problem through the use of three dimensional ray optics, wedge diffraction and creeping wave techniques. It also has been shown that the diffraction by a three dimensional cone tip can be approximated as if the tip were a two-dimensional wedge. Especially in the elevation plane, this approximation yields fairly good results. Thus, in the following development we shall use similar approximations to analyze the radiation patterns in the elevation plane for an antenna mounted on the surface of an aircraft fuselage.

In order to illustrate the application of the wedge diffraction analysis let us consider the model in Fig. 9 where a circumferential slot is mounted on the surface at a distance d_s from edge 1 and $(a-d_s)$ from edge 5. This model has a cone capping on a finite circular cylinder. Thus, the hard surface boundary condition is employed. The magnetic field radiated by the antenna is grazingly incident on edge 1 and edge 5 causing single diffractions at these edges, which in turn gives rise to the double diffractions at edge 2 and 4. Subsequently triple diffraction occurs at edge 3 due to the doubly diffracted field

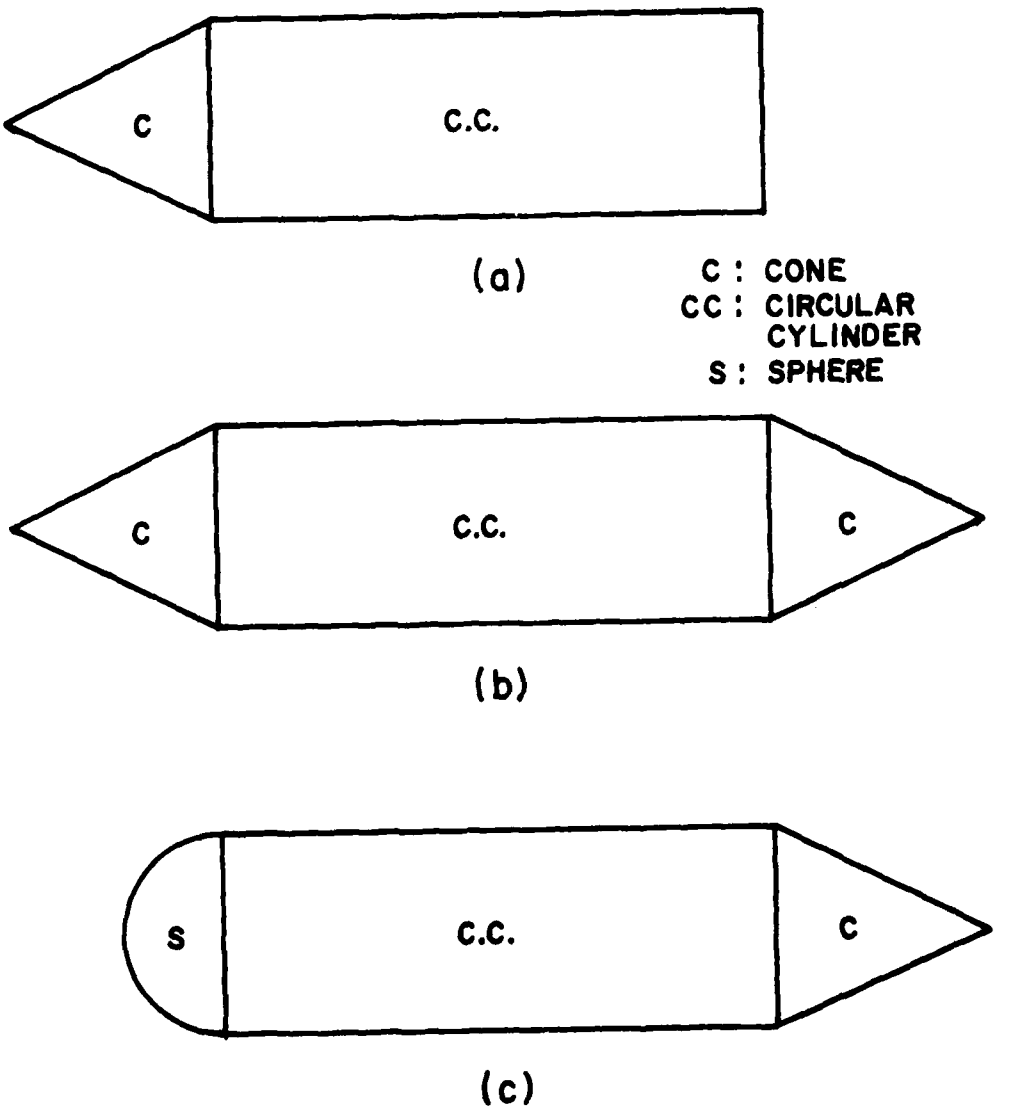

Fig. 8. Simple models for fuselage.

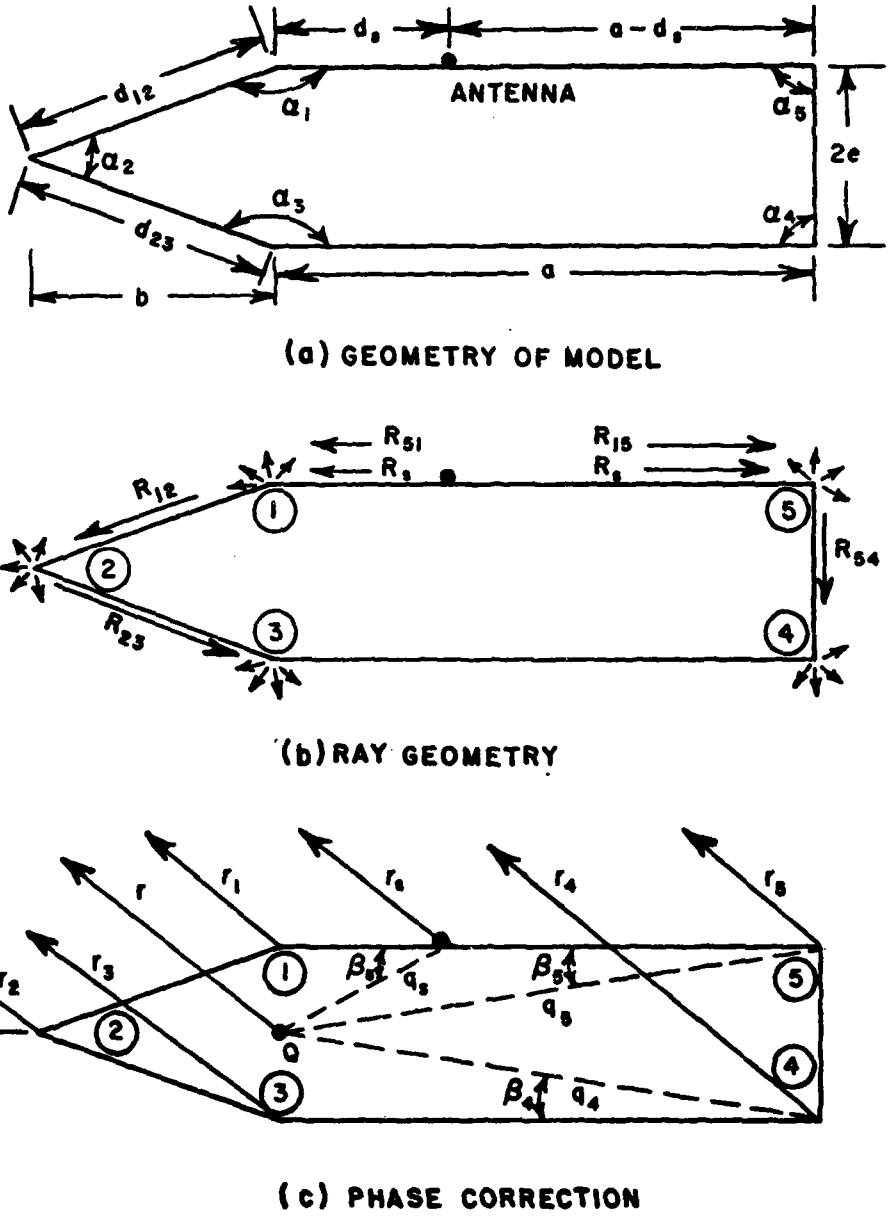

Fig. 9. Simple geometry of an aircraft fuselage.

incident on the discontinuities. The interaction between edge 3 and 4 produces higher-order diffracted terms. However, the effect is so small that one can neglect the higher-order terms without causing any significant change in the radiation patterns. In terms of the far field pattern $F(\theta,\phi)$ of the source the radiated field in the elevation plane is given by

$$(32) \qquad H_s(\theta,\phi=0) = [H_o\ F(\theta,\phi=0)/\sqrt{r_s}]\ \frac{e^{-jkr_s}}{\sqrt{r_s}}$$

where $\quad 0 \leq \theta \leq 180°$

H_o = a normalization factor which is the magnetic field intensity at the pattern maximum at $r_s = 1$ unit, as projected from the far field.

Note that the factor $e^{j\omega t}$ is assumed understood and is suppressed throughout this report. From the relationship given in Reference [3], which relates the field value $H(\rho,\theta)$ to the ray $R(\theta)$, one can express the source field in ray form as

$$(33) \qquad H_s(r,\theta) = \left[\frac{H_o\ F(\theta)}{\sqrt{r}}\right] \frac{e^{-jkr}}{\sqrt{r}} = \left[\frac{R_s(\theta)}{\sqrt{r}}\right] \frac{e^{-j(kr+\frac{\pi}{4})}}{\sqrt{2\pi kr}}$$

$$0 \leq \theta \leq 180°$$

where $R_s(\theta)$ is the incident ray and is given as

$$(34) \qquad R_s(\theta) = [H_o\ F(\theta)]\ \sqrt{2\pi k}\ \ e^{j\frac{\pi}{4}} \qquad 0 \leq \theta \leq 180° \ .$$

Now if we normalize this equation by the quantity

$$(\sqrt{2\pi k}\ \ e^{j\frac{\pi}{4}}\ H_o),$$

then the incident ray is simply expressed by

$$R_s(\theta) = F(\theta) \qquad 0 \leq \theta \leq 180° \quad . \tag{35}$$

This simplifies our analysis, consequently the ray form of the radiation field is employed throughout the following development.

The singly diffracted rays in any direction resulting from diffractions by the incident rays striking the discontinuities at edges 1 and 5 are given at edge 1 by

$$R_1^{(1)}(\theta) = [R_s(\theta=0°)/\sqrt{d_s}]\ V_B\ (d_s,\ 180° - \theta,\ n_1) \cdot RDF_1 \qquad 0° \leq \theta \leq 180° \tag{36}$$

$$R_1^{(1)}(\theta) = [R_s(\theta=0°)/\sqrt{d_s}]\ V_B\ (d_s,\ 540° - \theta,\ n_1) \cdot RDF_1 \qquad 360° - \alpha_1 \leq \theta \leq 360°$$

and at edge 5 by

$$R_5^{(1)}(\theta) = [R_s(\theta=180°)/\sqrt{a-d_s}]\ V_B\ (a-d_s,\ \theta,\ n_5) \cdot RDF_5 \qquad 0° \leq \theta \leq 360° - \alpha_5 \tag{37}$$

where α_1 = the wedge angle of edge 1
α_5 = the wedge angle of edge 5
n_1, n_5 = the constants related to the wedge angles α_1 and α_5, respectively, by the relation
WA = $\alpha = (2-n)\pi$
RDF = ray divergence factor.

The expression for the RDF can be easily obtained; however, it has been modified to avoid the singularity involvement due to the caustic effect as discussed in Section I and is given by

$$(38) \qquad RDF_1 = \begin{cases} \sqrt{\dfrac{e\ d_s}{(e+d_s \sin\theta)\ r}} & 0 \le \theta \le 180° \\ \sqrt{\dfrac{d_s}{r}} & 180° \le \theta \le 360° \end{cases}$$

$$(39) \qquad RDF_5 = \begin{cases} \sqrt{\dfrac{e(a-d_s)}{[e+(a-d_s)\sin\theta]\ r}} & 0 \le \theta \le 180° \\ \sqrt{\dfrac{a-d_s}{r}} & 180° \le \theta \le 360°. \end{cases}$$

This modification has been proved satisfactorily in the radiation pattern prediction as one shall see later. Note that the subscript denotes the edge and the superscript denotes the order of the diffraction.

The doubly diffracted rays at edges 2 and 4 are produced when the singly diffracted rays R_{12} and R_{54} from edges 1 and 5, respectively, arrive at edges 2 and 4. In addition, the singly diffracted rays from edges 1 and 5 travel in the opposite direction and strike edges 5 and 1, respectively, causing another set of doubly diffracted fields. These doubly diffracted rays can be obtained in a similar manner and are given at edge 2 by

$$(40) \qquad R_2^{(2)}(\theta) = \left[\frac{R_1^{(1)}(\theta=360°-\beta_2)}{\sqrt{d_{12}}}\right] V_B(d_{12}, 180°-\beta_2-\theta, n_2) \cdot RDF_2 \qquad 0 \le \theta \le 180°-\beta_2$$

$$= \left[\frac{R_1^{(1)}(\theta=360°-\beta_2)}{\sqrt{d_{12}}}\right] V_B(d_{12}, 540°-\beta_2-\theta, n_2) \cdot RDF_2 \qquad 180°+\beta_2 \le \theta \le 360°$$

at edge 4 by

$$R_4^{(2)}(\theta) = \left[\frac{R_5^{(1)}(\theta=360°-\alpha_5)}{\sqrt{d_{54}}}\right] V_B(d_{54},\theta-\alpha_4,n_4) \cdot RDF_4 \qquad \alpha_4 \leq \theta \leq 360°-\alpha_4 \tag{41}$$

at edge 1 by

$$R_1^{(2)}(\theta) = \left[\frac{R_{51}}{\sqrt{a}}\right] \cdot V_B(a,180°-\theta,n_1) \cdot RDF_{51} \qquad 0 \leq \theta \leq 180° \tag{42}$$

$$= \left[\frac{R_{51}}{\sqrt{a}}\right] \cdot V_B(a,540°-\theta,n_1) \cdot RDF_{51} \qquad 180°+\alpha_1 \leq \theta \leq 360°$$

and at edge 5 by

$$R_5^{(2)}(\theta) = \left[\frac{R_{15}}{\sqrt{a}}\right] \cdot V_B(a,\theta,n_5) \cdot RDF_{15} \qquad 0 \leq \theta \leq 360°-\alpha_5 \tag{43}$$

where

$$R_{51} = R_5^{(1)}(\theta=0°) \tag{44}$$

$$R_{15} = R_1^{(1)}(\theta=180°) \tag{45}$$

$$\beta_2 = \frac{\alpha_2}{2} \tag{46}$$

$$(47) \qquad RDF_{15} = RDF_{51} = \begin{cases} \sqrt{\dfrac{e\ a}{(e+a\ \sin\theta)\ r}} & 0 \le \theta \le 180^\circ \\ \sqrt{\dfrac{a}{r}} & 180^\circ \le \theta \le 360^\circ \end{cases} .$$

Notice that the ray divergence factor RDF_{51} at edge 1 due to the arriving of ray R_{51} is different from RDF_1 simply because of the distance it travels. For the same reason, RDF_{15} is different from RDF_5. However, RDF_{15} is equal to RDF_{51} because of the symmetry of the problem. Since the dimensions of the fuselage are large compared with the wavelength the effect of the RDF at edge 4 is thus insignificant and can be neglected, i.e., $\theta=\pi$ or $RDF_4 = \sqrt{\frac{d_{54}}{r}}$. It is obvious that the ray divergence factor at edge 2, RDF_2, is essentially equal to $\sqrt{\frac{d_{12}}{r}}$.

Similarly the triply diffracted ray at edge 3 can be found and written as

$$(48) \qquad R_3^{(3)}(\theta) = \left[\frac{R_2^{(2)}(\theta=180^\circ+\beta_2)}{\sqrt{d_{23}}}\right] V_B(d_{23},\beta_2-\theta,n_3) \cdot RDF_3 \qquad 0 \le \theta \le \beta_2$$

$$= \left[\frac{R_2^{(2)}(\theta=180^\circ+\beta_2)}{\sqrt{d_{23}}}\right] V_B(d_{23},360^\circ+\beta_2-\theta,n_3) \cdot RDF_3 \qquad 180^\circ \le \theta \le 360^\circ .$$

As we mentioned earlier, the dimensions of the aircraft fuselage are large and also the contribution of the third-order diffractions in the far field radiation pattern are very small, in which case the effect of the RDF at edge 3 is negligible. Thus θ in RDF_3 is again set to π or $RDF_3 = \sqrt{\frac{d_{23}}{r}}$. Here we have also neglected those contributions of the higher-order terms which are due to the multi-interactions among the edges, since they have little effect in the radiation pattern.

With the phase reference point at the point Q, the mid-point of the fuselage as shown in Fig. 9, the rays radiated from the source and the edges are multiplied by appropriate phase correction terms, giving

$$R_s(\theta) = \frac{F(\theta)}{\sqrt{r}} e^{-jkq_s\cos(\beta_s+\theta)} \qquad 0\leq\theta\leq 180° \tag{49}$$

$$R_1(\theta) = \left[F(\theta=0) \cdot V_B(d_s,180°-\theta,n_1)\sqrt{\frac{e}{[e+d_s\sin\theta]r}} + F(\theta=180°) \cdot V_B(a-d_s,0°,n_5) \cdot V_B(a,180°-\theta,n_1)\sqrt{\frac{e}{(e+a\sin\theta)r}}\right] \cdot e^{jke\sin\theta} \qquad 0\leq\theta\leq 180° \tag{50}$$

$$= \left[F(\theta=0) \cdot V_B(d_s,540°-\theta,n_1) + F(\theta=180°)V_B(a-d_s,0°,n_5) \cdot V_B(a,540°-\theta,n_1)\ \frac{e^{jke\sin\theta}}{\sqrt{r}}\right] \qquad 180°\leq\theta\leq 360°$$

$$R_2(\theta) = \left[F(\theta=0°)\right] \cdot V_B(d_s,180°+\beta_2,n_1)\ V_B(d_{12},180°-\beta_2-\theta,n_2) \cdot \frac{e^{jkb\cos\theta}}{\sqrt{r}} \qquad 0\leq\theta\leq 180°-\beta_2 \tag{51}$$

$$= F(\theta=0°)\ V_B(d_s,180°+\beta_2,n_1) \cdot V_B(d_{12},540-\beta_2-\theta,n_2) \cdot \frac{e^{jkb\cos\theta}}{\sqrt{r}} \qquad 180°+\beta_2\leq\theta\leq 360°$$

(52) $$R_3(\theta) = F(\theta=0°)\ V_B(d_s, 180°+\beta_2, n_1) \cdot V_B(d_{12}, 360°-2\beta_2, n_2) \cdot V_B(d_{23}, \beta_2-\theta, n_3)\ \frac{e^{-jke\sin\theta}}{\sqrt{r}} \qquad 0 \le \theta \le \beta_2$$

$$= F(\theta=0°)\ V_B(d_s, 180°+\beta_2, n_1) \cdot V_B(d_{12}, 360°-2\beta_2, n_2)\ V_B(d_{23}, 360°+\beta_2-\theta, n_3) \cdot \frac{e^{-jke\sin\theta}}{\sqrt{r}} \qquad 180° \le \theta \le 360°$$

(53) $$R_4(\theta) = F(\theta=180°) \cdot V_B(a-d_s, 360°-\alpha_5, n_5) \cdot V_B(d_{54}, \theta-\alpha_4, n_4) \cdot \frac{e^{-jkq_4\cos(\theta-\beta_4)}}{\sqrt{r}} \qquad \alpha_4 \le \theta \le 360°-\alpha_4$$

(54) $$R_5(\theta) = \left[F(\theta=180°) \cdot V_B(a-d_s, \theta, n_5)\sqrt{\frac{e}{e+(a-d_s)\sin\theta}} + F(\theta=0°) \cdot V_B(d_s, 0°, n_1) \cdot V_B(a, \theta, n_5)\sqrt{\frac{e}{e+a\sin\theta}}\right] \cdot \frac{e^{-jkq_5\cos(\theta+\beta_5)}}{\sqrt{r}} \qquad 0° \le \theta \le 180°$$

$$R_5(\theta) = [F(\theta=180°) \cdot V_B(a-d_s, \theta, n_5) + F(\theta=0°) \cdot V_B(d_s, 0°, n_1)\ V_B(a, \theta, n_5)] \cdot \frac{e^{-jkq_5\cos(\theta+\beta_5)}}{\sqrt{r}} \qquad 180° \le \theta \le 360°-\alpha_5$$

where

(55) $$\beta_s = \tan^{-1}\left(\frac{e}{d}\right)$$

$$q_s = \sqrt{d^2+e^2}$$

$$q_4 = q_5 = \sqrt{a^2+e^2}$$

$$\beta_4 = \beta_5 = \tan^{-1}\left(\frac{e}{a}\right)$$

α_4, α_5 = the wedge angle of edge 4 and 5, in our case here $\alpha_4=\alpha_5=90°$.

The total field in ray form at any observation point then is simply the superposition of the direct ray and diffracted rays. Hence the radiation pattern in the elevation plane is obtained as

(56) $$R_T(\theta) = R_s(\theta)+R_1(\theta)+R_2(\theta)+R_3(\theta)+R_5(\theta) \qquad 0\leq\theta\leq\beta_2$$

(57) $$R_T(\theta) = R_s(\theta)+R_1(\theta)+R_2(\theta)+R_5(\theta) \qquad \beta_2<\theta<90°$$

(58) $$R_T(\theta) = R_s(\theta)+R_1(\theta)+R_2(\theta)+R_4(\theta)+R_5(\theta) \qquad 90°\leq\theta\leq180°-\beta_2$$

(59) $$R_T(\theta) = R_s(\theta)+R_1(\theta)+R_4(\theta)+R_5(\theta) \qquad 180°-\beta_2<\theta\leq180°$$

(60) $$R_T(\theta) = R_3(\theta)+R_4(\theta)+R_5(\theta) \qquad 180°<\theta<180°+\beta_2$$

(61) $$R_T(\theta) = R_2(\theta)+R_3(\theta)+R_4(\theta)+R_5(\theta) \qquad 180°+\beta_2\leq\theta\leq270°$$

(62) $$R_T(\theta) = R_2(\theta)+R_3(\theta)+R_4(\theta) \qquad 270°<\theta<360°-\beta_2$$

(63) $$R_T(\theta) = R_1(\theta)+R_2(\theta)+R_3(\theta)+R_4(\theta) \qquad 360°-\beta_2\leq\theta\leq360° \quad .$$

A calculated elevation pattern for the model of Fig. 9 with a circumferential slot located at d=8" from the edge 1 is shown in Fig. 10, along with a measured pattern.[9] It is seen that the

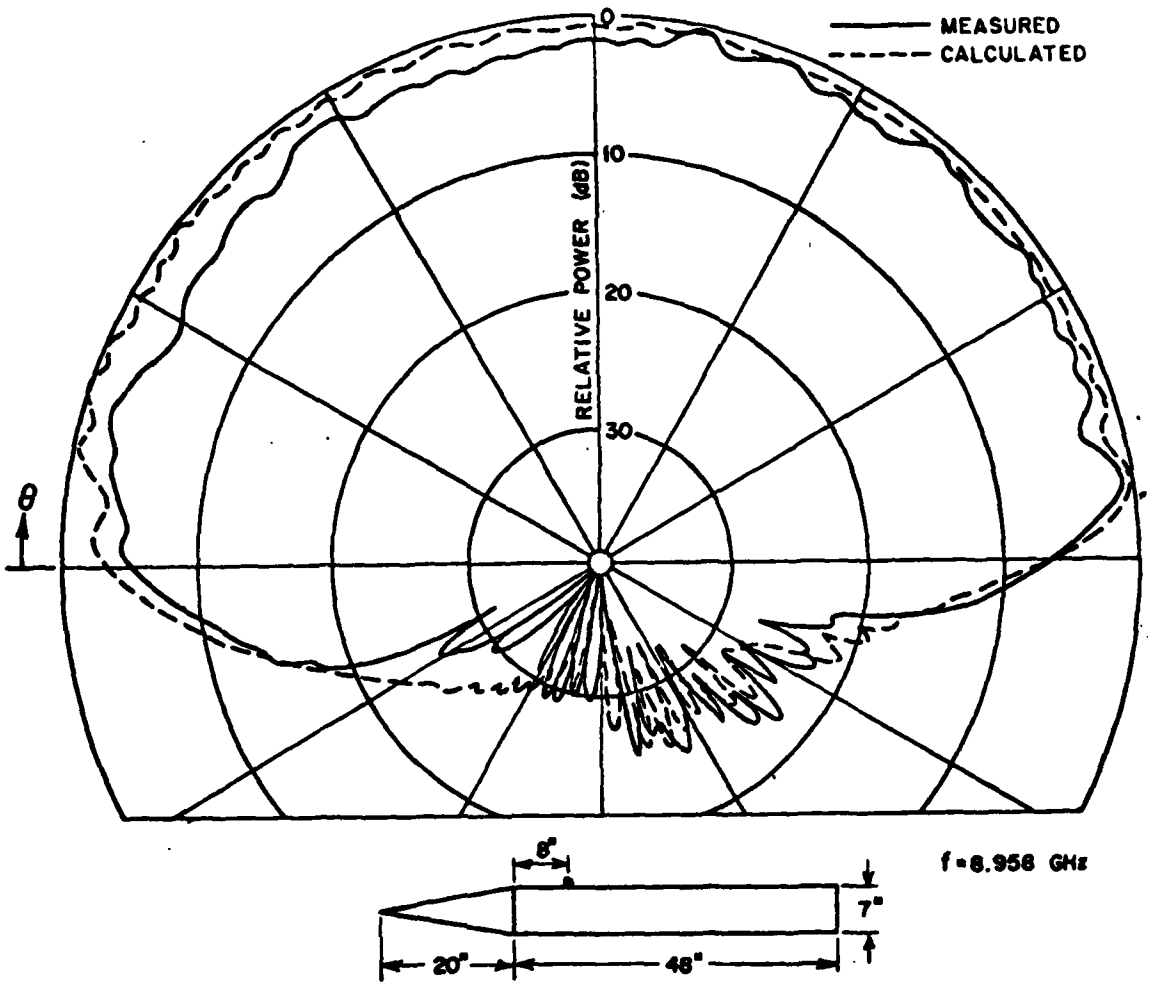

Fig. 10. Elevation plane patterns with a circumferential slot mounted on a simple fuselage model.

theoretically calculated radiation pattern compares very favorably with the measured result. It is noticed that the field pattern has more coverage in the forward region than that in the backward region, this is simply because the source is located in the front portion of the model. As discussed in Reference [16], the pattern has more ripples in the forward direction and less in the backward direction, which is also due to the location of the antenna system with respect to the diffracting edge.

The model shown in Fig. 11 is a m fication to the model described above, in which another cone is mounted on the other end of the circular cylinder. In general, the sizes of these two cones will be different; however, in the following development it is assumed that they are dimensionally the same. Due to the geometrical similarity, the ray components necessary to describe the radiation pattern of this model are similar to those in Eqs. (56) through (63) and are easily obtained with only some minor modifications. For example, the expression for the doubly diffracted field in ray form from edge 5 is given as

$$R_5^{(2)}(\theta) = R_6^{(1)}(180°+\beta_5) \cdot V_B(d_{65},\theta-\beta_5,n_5) \cdot \frac{e^{-jk(a+c)\cos\theta}}{\sqrt{r}} \tag{64}$$

$$= F(\theta=180°) \cdot V_B(a-d,180°+\beta_5,n_6) \cdot V_B(d_{65},\theta-\beta_5,n_5) \cdot \frac{e^{-jk(a+c)\cos\theta}}{\sqrt{r}} \qquad \beta_5 \leq \theta \leq 360°-\beta_5$$

where

$\beta_5 = \frac{1}{2}\alpha_5$, the wedge angle at edge 5.

As in the previous case, we have made some approximations which have simplified our analysis without causing any significant error. Hence, the radiation pattern is obtained by summing all of the rays which contribute in the various regions and is given by

$$R_T(\theta) = R_s(\theta)+R_1(\theta)+R_2(\theta)+R_3(\theta)+R_6(\theta) \qquad 0 \leq \theta \leq \alpha \tag{65}$$

$$R_T(\theta) = R_s(\theta)+R_1(\theta)+R_2(\theta)+R_5(\theta)+R_6(\theta) \qquad \alpha \leq \theta \leq 180°-\alpha \tag{66}$$

$$R_T(\theta) = R_s(\theta)+R_1(\theta)+R_4(\theta)+R_5(\theta)+R_6(\theta) \qquad 180°-\alpha \leq \theta \leq 180° \tag{67}$$

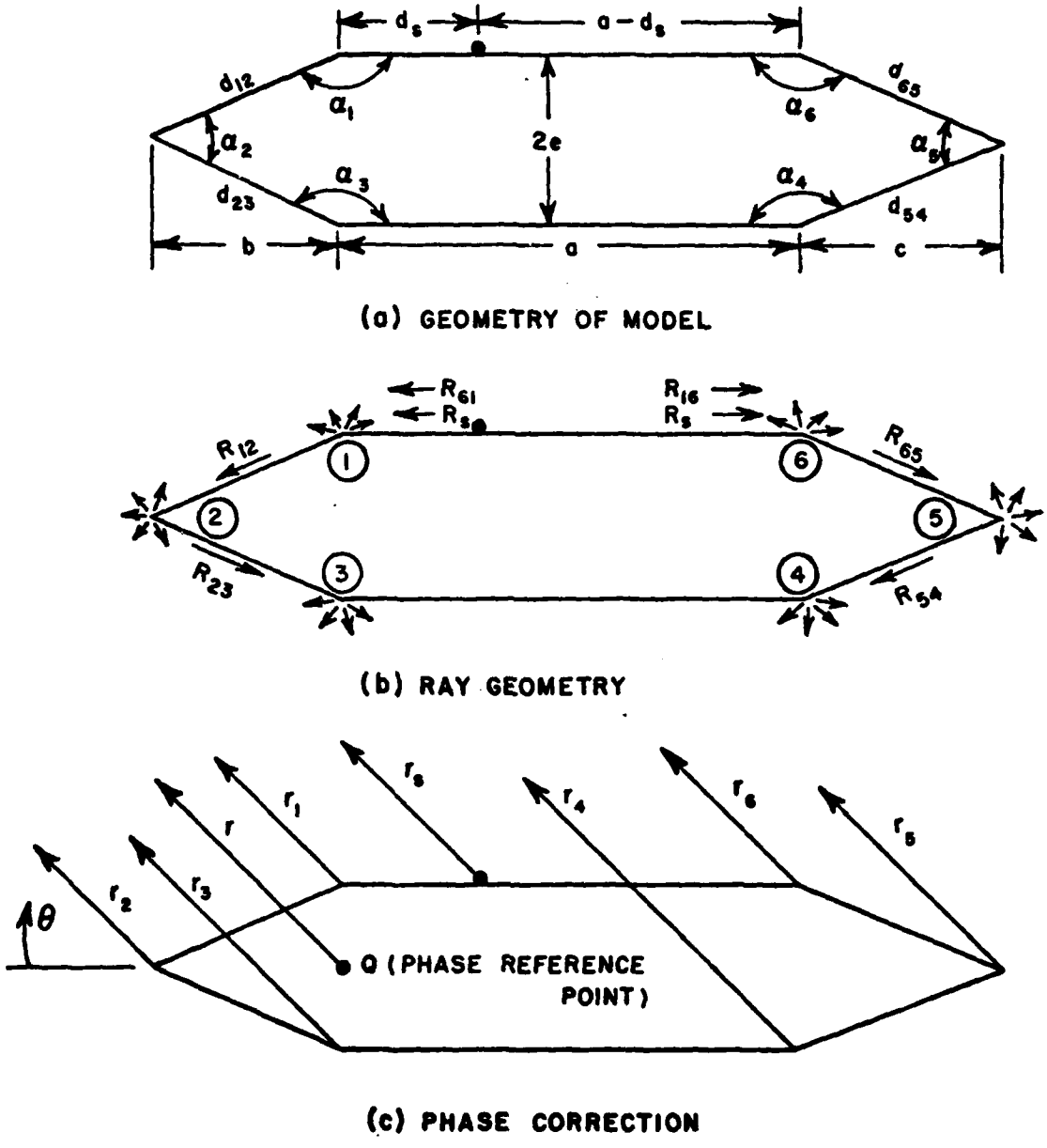

Fig. 11. Simple geometry of aircraft fuselage.

$$R_T(\theta) = R_3(\theta)+R_4(\theta)+R_5(\theta)+R_6(\theta) \qquad 180° \leq \theta \leq 180°+\alpha \tag{68}$$

$$R_T(\theta) = R_2(\theta)+R_3(\theta)+R_4(\theta)+R_5(\theta) \qquad 180°+\alpha \leq \theta \leq 360°-\alpha \tag{69}$$

$$R_T(\theta) = R_1(\theta)+R_2(\theta)+R_3(\theta)+R_4(\theta) \qquad 360°-\alpha \leq \theta \leq 360° \tag{70}$$

where

$\alpha = \alpha_2 = \alpha_5$ = wedge angle of edge 2 or 5.

The calculated radiation pattern in the elevation plane for a circumferential slot mounted on the model of Fig. 11 at a distance d=8" from edge 1 is presented in Fig. 12. Compared with Fig. 10, one sees that the backlobes in the deep shadow region are lower for this model. The reason is apparent, since the addition of the extra cone has reduced the scattering effects at edges 4 and 5 and thus reduced the level of backlobes. The calculated radiation pattern in the elevation plane obtained by replacing the circumferential slot by a $1/4\lambda$ monopole is shown in Fig. 13. In order to see the effects of the fuselage on the antenna performance the radiation pattern of an electric dipole radiating in free space is also presented in Fig. 13. The effect of the aircraft fuselage on the radiation patterns is clearly shown through the comparison between these two patterns. One should expect higher level of sidelobes in the forward region as shown in the pattern because of the location of the antenna which is near the front portion of the fuselage. The ripple shown in the pattern is a result of the scattering by the structure of the fuselage and this is taken into account by the various diffractions among the wedges. Note that the imperfect nulls occur at θ=90° and 270° should be expected because of the un-symmetrical antenna location as mentioned above. Thus, the performance of the antenna is greatly affected by the aircraft structure (especially the fuselage shape).

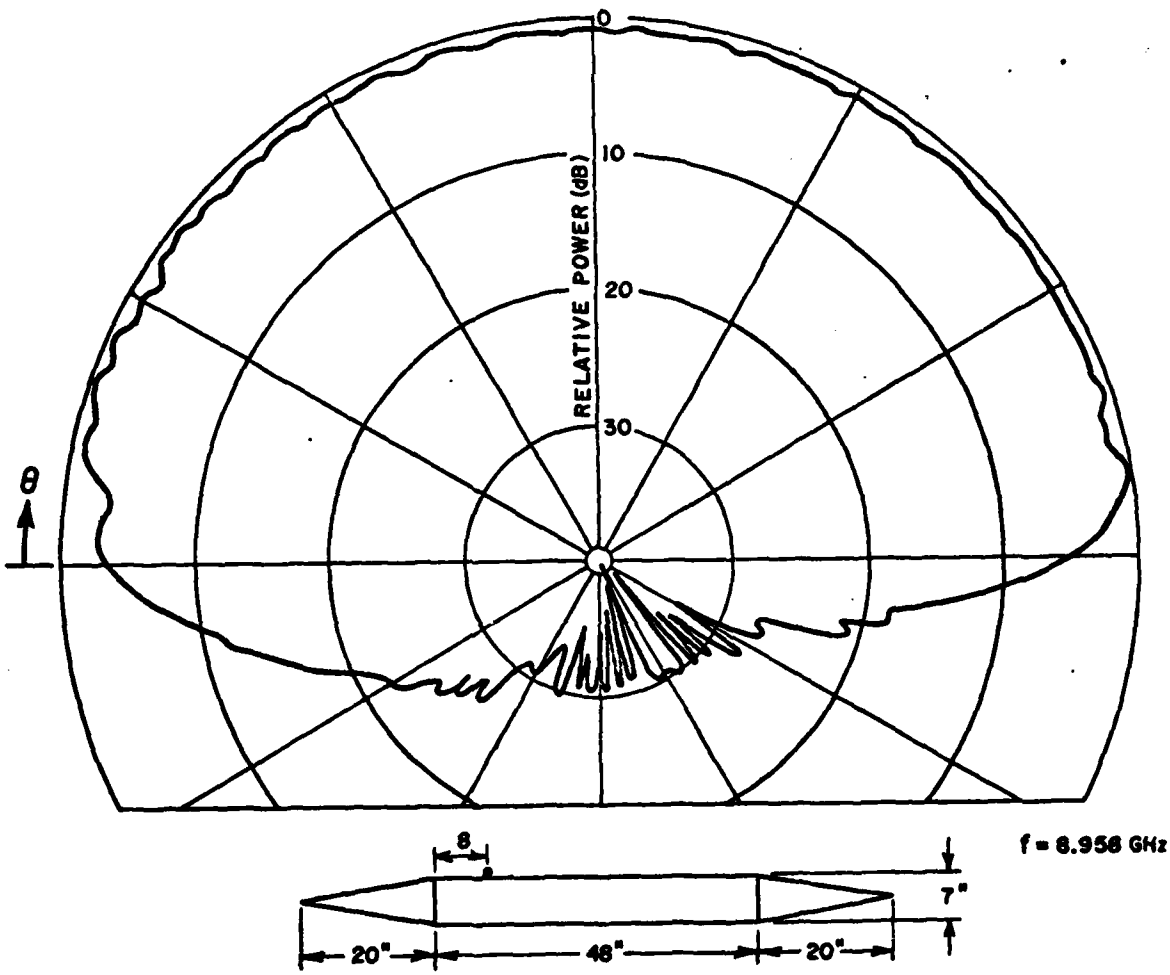

Fig. 12. Elevation plane pattern with a circumferential slot mounted on a simple fuselage model.

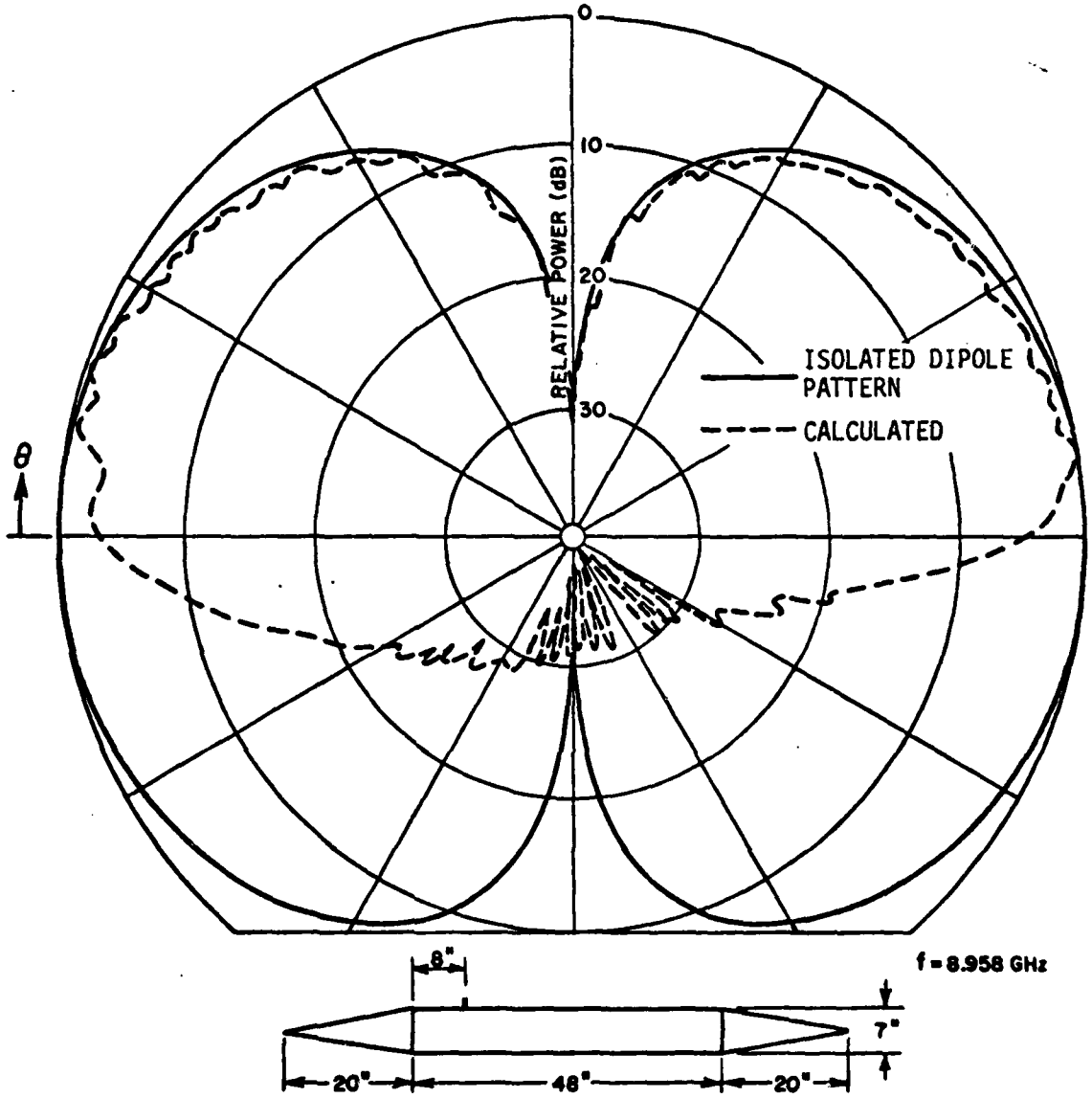

Fig. 13. Elevation plane pattern with a 1/4λ monopole mounted on a simple fuselage model.

In order to improve the theoretical simulation of an aircraft fuselage, a curved leading edge model is introduced. This model is shown in Fig. 14 and has a hemisphere replacing the cone on the leading edge. The sphere has the same radius as that of cylinder. This blunt model might in some cases be a better approximation of an actual fuselage than the previous two models. Creeping wave theory is employed with the wedge diffraction technique to solve this problem. The diffracted fields in ray form from edges 4, 5 and 6 are the same as those in the previous case. But for the leading edge, the creeping wave expression is now applied to describe the lossy surface wave propagating around the curved surface so that the effect of the scattering by the blunt structure could be properly examined. The general form for a diffracted ray radiating from point Q_2, some point on a curved surface, in the scattered field direction with the source located off the curved surface is given by

$$R_{cw}(Q_2) = R_i(Q_1)\left[\sum_{m=0}^{\infty} D_m(Q_1)D_m(Q_2)\, e^{-\int_0^{s_1}\alpha_m(s')ds'}\right] e^{-jks_1} \tag{71}$$

where

Q_1 = the point on the curved surface at which the direct ray from the antenna is grazingly incident.

Q_2 = arbitrary diffracting point on the curved surface.

S_1 = the distance or arc length which the surface ray travels.

$R_i(Q_1)$ = the incident ray at point Q_1.

The incident wave excites an infinity of surface wave modes, as the summation in Eq. (71) indicated, each with its own diffraction coefficient and attenuation constant; only the dominant mode is being considered in this analysis for the sake of simplicity, i.e., m=0. Hence Eq. (71) is reduced to

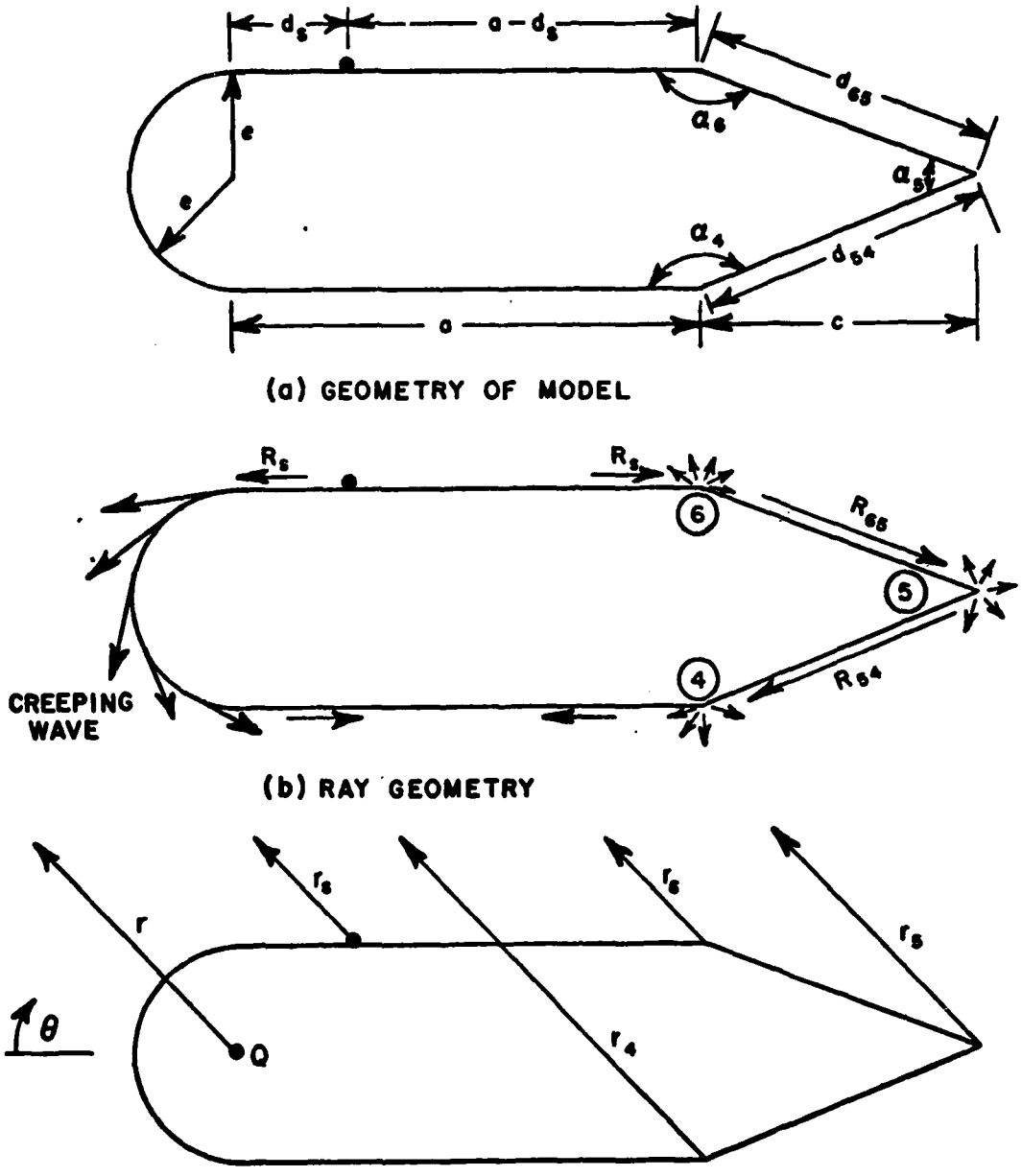

Fig. 14. Simple model for an aircraft fuselage with curved surface.

$$(72) \qquad R_{cw}(Q_2) = R_i(Q_1)D_o(Q_1)D_o(Q_2)\, e^{-\alpha_o s_1}\, e^{-jks_1} .$$

This is a simplified expression for a diffracted surface ray at any arbitrary direction with the source located off the curved surface. Note that the elimination of the integration in Eq. (71) is due to the fact the attenuation constant α_o is not a function of t_1, arc length, but a constant for a circular cylinder or a sphere given by[10]

$$(73) \qquad \alpha_{o_h} \cong \frac{1}{2a}\,(ka)^{1/3}\,[\tfrac{3\pi}{4}]^{2/3}\, e^{j\frac{\pi}{6}} ,$$

where the hard surface boundary condition is employed and "a" is the radius of the sphere. The diffraction coefficient D_{o_h} is given as[10]

$$(74) \qquad D_{o_h}^{\,2} \cong \frac{e^{-j\frac{\pi}{12}}}{\sqrt{k}}\,(ka)^{1/3}\, d_o$$

where d_o is equal to 1.083.[10]

Although the mounting of a hemisphere to a circular cylinder produces a continuous radius of curvature and first derivative, the second derivative of the radius of curvature, however, is by no means continuous. It is discontinuous at the sphere-cylinder junction. Even so, the diffraction at the discontinuity Q_1 is so small that one can neglect its effect since the dimensions of the model are quite large in terms of wavelength. This assumes that the incident ray is equal to the surface ray at Q_1. Based on this approximation, the diffraction coefficient at Q_1 is found by

$$(75) \qquad R_i(Q_1) = F(\theta{=}0°)\, e^{-jkd}$$

$$(76) \qquad R_{cw}(Q_1) = R_i(Q_1)\, D_o^{\,2}(Q_1) = F(\theta{=}0°) \cdot e^{-jkd}\, D_o^{\,2}(Q_1) .$$

By equating these two equations, $D_o(Q_1)$ is given as

(77) $$D_o(Q_1) = 1 \quad .$$

Therefore, the creeping wave expression in any direction can be written as

(78) $$R_{cw}(\theta) \cong F(\ =0°)\ e^{-jkd}\left[\frac{e^{-j\frac{\pi}{12}}}{\sqrt{k}}\ (ka)^{1/3}\ d_o\right]^{1/2} e^{-\theta[\frac{1}{2}(ka)^{1/3}\ (\frac{3\pi}{4})^{2/3}\ e^{j\frac{\pi}{6}} + jka]}$$

$$180° \leq \theta \leq 360° \quad .$$

With the appropriate phase terms included and the various regions considered, the elevation plane radiation pattern is given by

(79) $$R_T(\theta) = R_s(\theta)+R_6(\theta) \qquad 0 \leq \theta < \beta_5$$

(80) $$R_T(\theta) = R_s(\theta)+R_6(\theta)+R_5(\theta) \qquad \beta_5 \leq \theta < 180°-\beta_5$$

(81) $$R_T(\theta) = R_s(\theta)+R_6(\theta)+R_5(\theta)+R_4(\theta) \qquad 180°-\beta_5 \leq \theta \leq 180°$$

(82) $$R_T(\theta) = R_{cw}(\theta)+R_6(\theta)+R_5(\theta)+R_4(\theta) \qquad 180° \leq \theta \leq 180°+\beta_5$$

(83) $$R_T(\theta) = R_{cw}(\theta)+R_5(\theta)+R_4(\theta) \qquad 180°+\beta_5 \leq \theta \leq 360°-\beta_5$$

(84) $$R_T(\theta) = R_{cw}(\theta)+R_4(\theta) \qquad 360°-\beta_5 < \theta \leq 360° \quad .$$

The calculated elevation plane radiation patterns for a circumferential slot and monopole mounted on this particular model are illustrated in Figs. 15 and 16. Those with cone type leading edges are also presented in Figs 15 and 16. From these figures one observes that the ripple level is decreased considerably for the

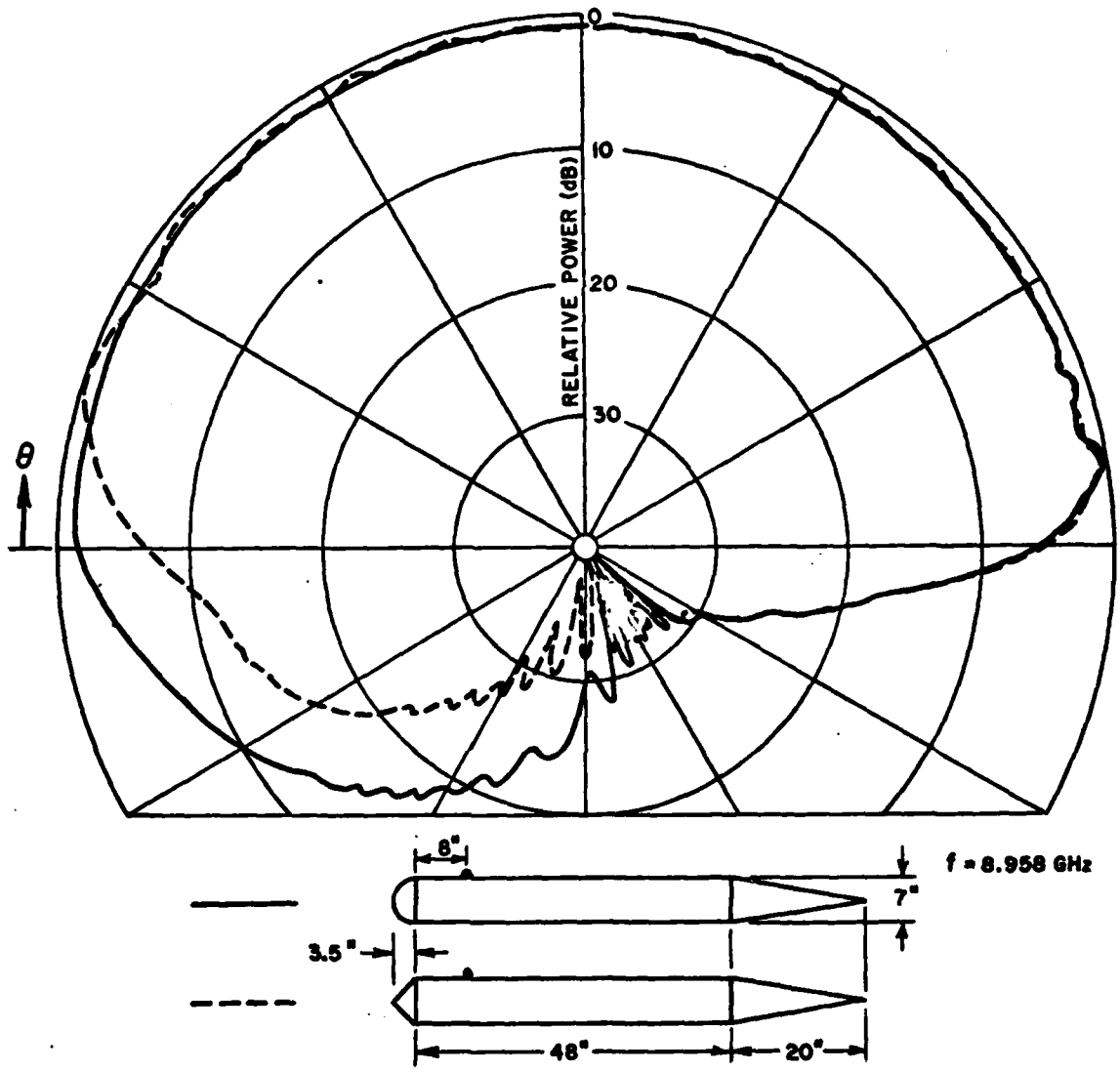

Fig. 15. Elevation plane patterns with a circumferential slot mounted on simple fuselage models.

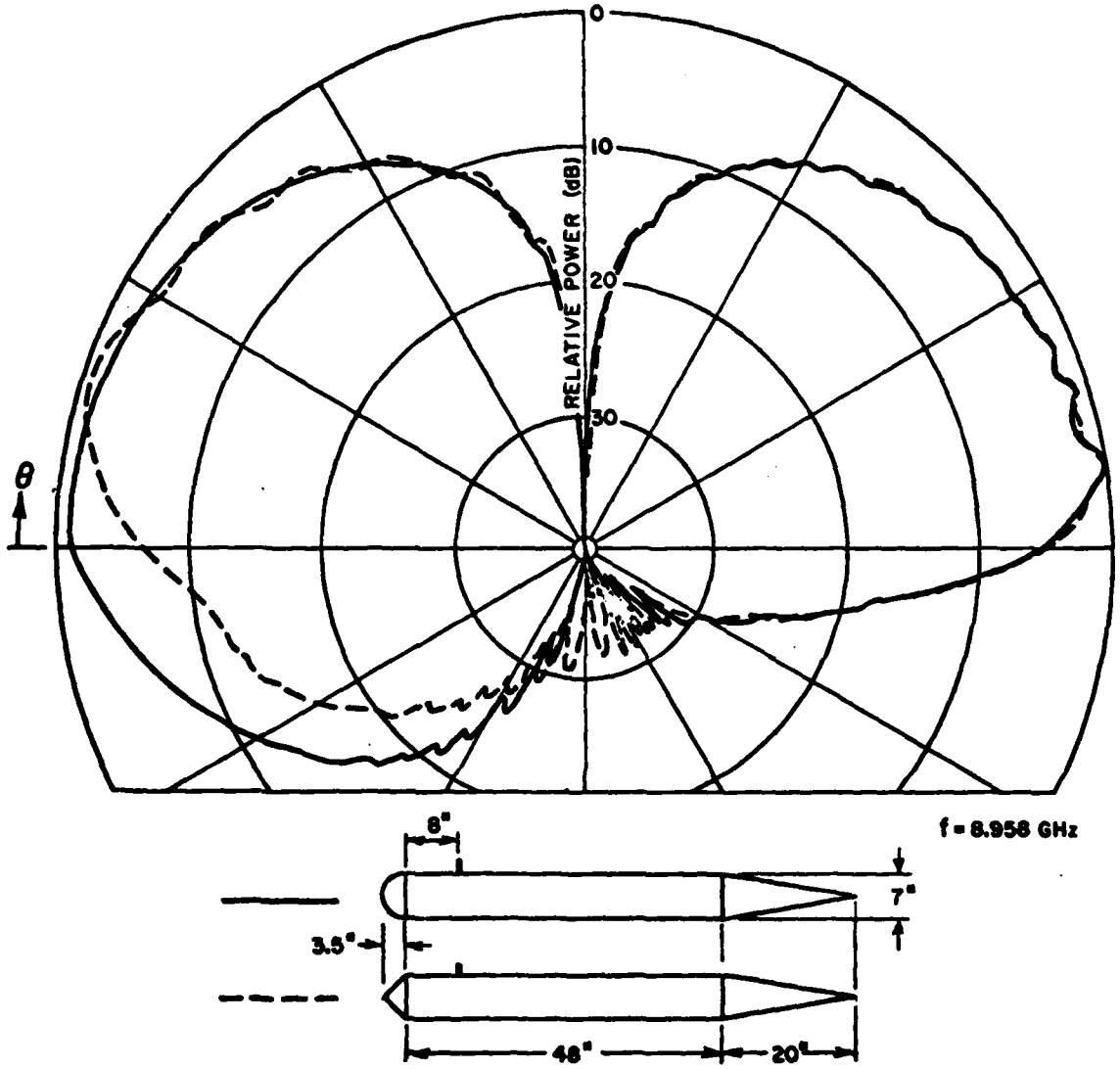

Fig. 16. Elevation plane patterns with a 1/4λ monopole mounted on simple fuselage models.

blunt model. Thus one concludes that the significant effect of the curved surface is reducing the ripple effect and smoothing the pattern.

Summary and conclusion

The radiation patterns in the elevation plane for an antenna mounted on a simple fuselage model, composed of cones, spheres, and cylinders, can be obtained by treating this three dimensional model as a two dimensional problem through the use of modern diffraction techniques. The results obtained, using these techniques and approximations compare very favorably with the measured results. The structure of the aircraft fuselage has a very significant effect on the antenna performance with respect to distortion of antenna patterns. For example, the effect of a cone type structure often increases the ripple on the radiation patterns whereas that of a curved surface tends to smooth the patterns. The location of the antenna is also an important factor in determining the radiation patterns in the elevation plane. In addition, the pattern in the illuminated region of an antenna is simply its direct radiation while that in the shadow region is completely dominated by the scattering of the structure of aircraft fuselage. Although these simple models illustrate the effects of fuselage structure on radiation patterns, they fail to include the general variety of aircraft fuselages encountered in practice. Thus, a more general representation of the aircraft fuselage is presented in the next section in which any convex body (fuselage) can be modelled to a good approximation.

IV. ELEVATION PATTERNS FOR GENERAL FUSELAGE MODELS

The radiation pattern in the elevation plane for an aircraft fuselage was initially studied using a basic model composed of cylinders, spheres, and cones as discussed in the last section. The solutions were based on the two-dimensional analysis which, as demonstrated by Ryan,[9] also is valid for the three dimensional elevation plane patterns. Some of the results of this study were

illustrated in Figs. 10 through 16. Even though those solutions are valid for the simple models, they really are not general enough to include the wide variety of aircraft fuselages encountered in practice. For example, an aircraft fuselage is usually a convex body that can not be completely described by simple mathematical equations. Hence, in practice, an aircraft is often specified by points. Consequently a new approach is developed in which a set of discrete points is used to describe the shape of the fuselage. In this way any convex fuselage shape can be included in our general solution in a rather simple manner.

In addition, more general ellipsoidal models are developed using a more rigorous "GTD" solution. This "GTD" solution is developed specifically for a source located on the curved surface, which is in contrast to the case discussed in section II where the source was located off the curved surface. The most general model being considered is a composite (back to back) ellipsoid, however, elliptical cross-section cylinders are also good models to simulate a fuselage. In order to illustrate the validity of this new method, called "section matching method", the radiation patterns for circular cylinders for slot and monopole antennas are first calculated.

Basically this section is written to illustrate the validity of the "Section Matching Method". The only geometries considered in its application are for those that can be solved using the more rigorous "GTD" solutions. In the future this method will be used beyond the realm of the "GTD" solution taking into account more complex fuselage shapes. Not only is this important in terms of the profile of the fuselage in the elevation plane but also in terms of the cross-sectional shape in the roll plane.

A. GTD Solution For General Fuselage Models

1. Circular cylinder

The far field for various sources such as slot and monopole antennas mounted on an infinitely long perfectly conducting circular cylinder has been analyzed by Kouyoumjian.[17] In this solution the reciprocity theorem is employed so that the radiation pattern is derived from the plane wave scattering by a cylinder. The physical optics approximation for the surface current is used to describe the field in the region in which the source is directly illuminated by the incident plane wave (the lit region). The Fock current approximation[18] is used for the penumbra (transition) region, whereas, in the deep shadow region of the cylinder, the geometrical theory of diffraction solution is applied to give the far field expression. It is noted that a launch coefficient, which relates the creeping wave (GTD field) to the actual surface field or current, is introduced so that the GTD solution can be properly employed. This launch factor is deduced from the exact solution for the surface current on the circular cylinder; and, in its asymptotic form, involves the well-known Airy function.

The far-zone radiation pattern for a thin slot mounted on an infinitely long perfectly conducting circular cylinder, equivalent to a magnetic line source $k\hat{y}$, with radius "a" as shown in Fig. 17 can be obtained by employing the aforementioned GTD asymptotic expressions for the various regions and is given by Reference [17]

1) Lit Region: Geometrical Optics Description

$$R_y(\rho,\theta) = 2\, e^{j\, a \cos(\theta_0-\theta)} \tag{85}$$

2) Transition Region: $M^{-1} \leq \phi \leq \pi - M^{-1}$

$$R_y(\rho,\theta) = \left[g^*(\xi_1)\, e^{-jka\psi_1} + g^*(\xi_2)\, e^{-jka\psi_2}\right] \tag{86}$$

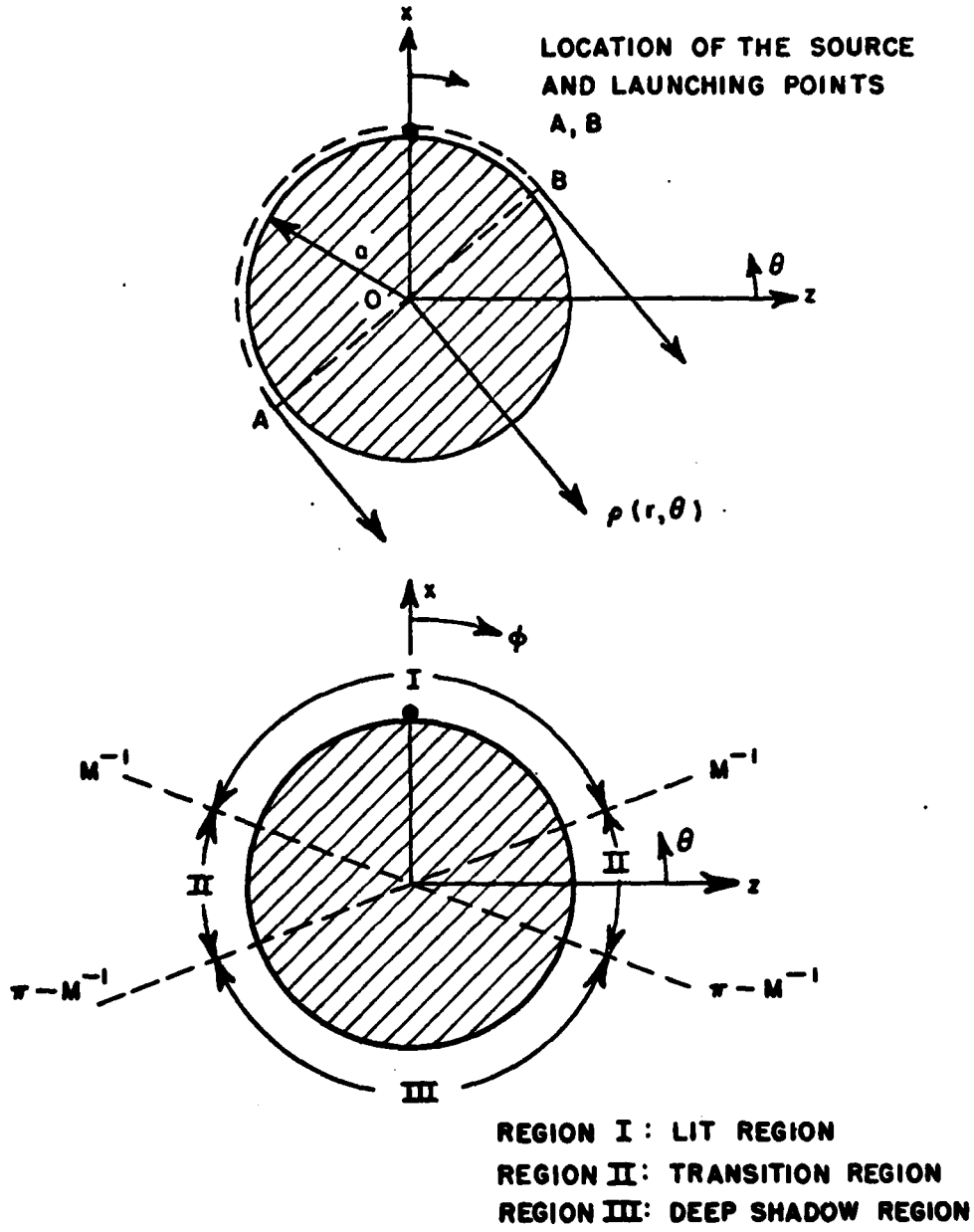

Fig. 17. Antenna mounted on a circular cylinder: GTD solution.

where

(87a) $$\psi_1 = |\theta_o - \theta| - \pi/2$$

$$\psi_2 = \frac{3\pi}{2} - |\theta_o - \theta|$$

$$M = \left(\frac{ka}{2}\right)^{1/3}$$

$$\phi = \theta - \theta_o \qquad \pi/2 \leq \theta \leq 3\pi/2$$

(87b) $$\xi_1 = \left(\frac{ka}{2}\right)^{1/3} \psi_1$$

$$\xi_2 = \left(\frac{ka}{2}\right)^{1/3} \psi_2 \quad .$$

The functions $g^*(\xi_1)$ and $g^*(\xi_2)$ are the conjugate of $g(\xi_1)$ and $g(\xi_2)$, respectively. The function $g(\xi)$ is the so called Fock's function for hard boundary condition ($\partial u/\partial n = 0$) and is given as

(88) $$g(\xi) = \frac{1}{\sqrt{\pi}} \int_{\Gamma_2} \frac{e^{j\xi\tau}}{W_1^2(\tau)} \, d\tau \quad .$$

The magnitude and phase of Fock's function $g(x)$ are given in Reference [18].

3) Deep Shadow Region: Surface Ray Description

(89) $$R_y(\rho,\theta) = (-2\pi) \left(\frac{ka}{2}\right)^{-1/3} e^{j\frac{\pi}{12}} \cdot \sum_{m=1}^{\infty} \left\{ [D_m^h(a)]^2 \, Ai(-\bar{q}_m) \, e^{-[\alpha_m^h(a)]s_1} \, e^{-jks_1} + [D_m^h(a)]^2 \, Ai(-\bar{q}_m) \, e^{-[\alpha_m^h(a)]s_2} \, e^{-jks_2} \right\}$$

where $s_1 = a\psi_1$

$s_2 = a\psi_2$

and ψ_1 and ψ_2 are defined in Eq. (87a) and $\bar{q}_m$ is the root of $Ai'(-\bar{q}_m)$, that is, $Ai'(-\bar{q}_m) = 0$. The diffraction coefficient $[D_m^h(a)]^2$ and the surface propagation constant $\alpha_m^h(a)$ are given below, respectively.[15]

$$(90) \qquad [D_m^h(a)]^2 = \frac{1}{2^{5/6}\sqrt{\pi}} \cdot \frac{a^{1/3}\, e^{-j\frac{\pi}{12}}}{k^{1/6} \cdot \bar{q}_m [Ai(-\bar{q}_m)]^2} \left\{ 1 + \left(\frac{ka}{2}\right)^{-2/3} \left[\frac{\bar{q}_m}{30} - \frac{0.1}{\bar{q}_m^2}\right] e^{-j\frac{\pi}{3}} \right\}$$

$$(91) \qquad \alpha_m^h(a) = \frac{\bar{q}_m}{a}\, e^{j\frac{\pi}{6}} \left(\frac{ka}{2}\right)^{1/3} \left\{ 1 + \left(\frac{ka}{2}\right)^{-2/3} \left(\frac{\bar{q}_m}{60} + \frac{0.1}{\bar{q}_m^2}\right) e^{-j\frac{\pi}{3}} \right\} .$$

The roots $\bar{q}_m$ and $Ai(-\bar{q}_m)$ can be found in Reference [22]. It is noted that the surface ray expression in Eq. (89) can be rewritten in the following way

$$(92) \qquad R_y(\rho,\theta) = (-2\pi) \left(\frac{ka}{2}\right)^{-1/3} e^{j\frac{\pi}{12}} \sum_{m=1}^{\infty} \left\{ [D_m^h(a)]^2\, Ai(-\bar{q}_m)\, e^{-\gamma(a)s_1} + [D_m^h(a)]^2\, Ai(-\bar{q}_m)\, e^{-\gamma(a)s_2} \right\}$$

where $\gamma(a) = \alpha_m^h(a) + jk$, propagation constant of the surface ray.

The calculated radiation patterns using Eqs. (85) to (92) in the xz-plane (elevation plane) of Fig. 17 for various cylinders have been shown to agree very favorably with those obtained from the modal solution, especially for $ka \geq 3.0$. These formulations also predict the

radiation pattern fairly well for small cylinders with radii down to the range from 1/3 to 1/4 wavelength.[19]

2. General cross-section cylinder

The results for the circular cylinder are extended to cylinders with general cross-sectional shape in which the curvature varies along the ray path. This variable curvature has a strong effect on the attenuation constant which in turn affects the energy propagation quite significantly. Thus, the representations for fields in the lit, transition and deep-shadow region are modified to include the variable curvature effect and again are given by

1) Lit Region:

$$R_y(\theta) = 2\, e^{jkr_s \cos(\theta-\theta_o)} \tag{93}$$

2) Transition Region:

$$R_y(\theta) = \left\{ g^*(\xi_A)\, e^{-j\int_A^P k\,ds}\, F(A) + g^*(\xi_B)\, e^{-j\int_B^P k\,ds} \cdot F(B) \right\} \tag{94}$$

3) Deep-Shadow Region:

$$R_y(\theta) = -2\pi j\left[\left(\frac{k\rho_g}{2}\right)^{-1/3}\right]_{\theta=\theta_p} e^{j\frac{\pi}{3}} \left(\frac{jk}{2\pi}\right)^{1/2} \cdot \sum_{m=1}^{\infty} \left\{ D_m^h(P)\, D_m^h(A)\, Ai(-\bar{q}_m)\, e^{-j\int_A^P \gamma_m^h(s)\,ds} \cdot F(A) + D_m^h(P)\, D_m^h(B)\, Ai(-\bar{q}_m)\, e^{-j\int_B^P \gamma_m^h(s)\,ds} F(B) \right\} \tag{95}$$

where A and B are the points that the surface rays launch in the direction of the observation point, θ; r_s is the distance from the

origin to the source location; and ρ_g is the radius of curvature of the curved surface;

$$\xi_A = \int_A^P \left(\frac{k}{2\rho_g^2}\right)^{1/3} ds$$

and

$$\xi_B = \int_B^P \left(\frac{k}{2\rho_g^2}\right)^{1/3} ds \quad .$$

The increment of the arc length along the ray trajectory is ds; F(A), F(B) are the phase correction factors at the launching points A and B; $g^*(\xi_A)$, $g^*(\xi_B)$ are the conjugates of $g(\xi_A)$ and $g(\xi_B)$, Fock's function as defined previously; and $D_m^h(P)$, $D_m^h(A)$, and $D_m^h(B)$ are the diffraction coefficients at the source location, launching points A and B, respectively. The propagation constant is $\gamma_m^h(s) = \alpha_m^h(s) + jk$, where α_m^h is the ray trajectory attenuation factor for the hard boundary case and k is $2\pi/\lambda$. In addition, $Ai(-\bar{q}_m)$ is the Airy function evaluated at $-\bar{q}_m$ where $\bar{q}_m$ is the root of $Ai'(-\bar{q}_m) = 0$. Note that the phase reference point for these formulations is at the origin. Some calculated radiation patterns in xz-plane (the elevation plane) employing these formulations for an elliptical cylinder are also given in Reference [19]. The result compares fairly well with the exact solution obtained by Sinclair[20] as shown in Fig. 18.

The same technique is also employed to derive the generalized expressions for slot antenna with soft boundary condition and infinitesimal monopole antenna. The equations again contain the Fock functions. A summary of the far field expressions for the circumferential slot, axial slot and infinitesimal monopole are presented in Table I.[17]

TABLE I

RADIATION FIELD IN RAY FORM IN THE ELEVATION PLANE OF A GENERAL FUSELAGE

ANTENNA	LIT REGION	TRANSITION REGION	DEEP SHADOW REGION
Slot Antenna (Hard Boundary)	$-2e^{jkr_s\cos(\theta-\theta_o)}$	$\left\{g^*(\varepsilon_A)\,e^{-j\int_A^P k\,ds}\cdot F(A) + g^*(\varepsilon_B)\,e^{-j\int_B^P k\,ds}\cdot F(B)\right\}$	$-2\pi j\left[\left(\frac{k\rho_g}{2}\right)^{-1/3}\right]_{\theta=\theta_p} e^{j\frac{\pi}{3}}\left(\frac{jk}{2\pi}\right)^{1/2}\sum_{m=1}^{\infty}\left\{D_m^h(P)\,D_m^h(A)\,Ai(-\bar{q}_m)\,e^{-j\int_A^P \gamma_m^h(s)\,ds}\cdot F(A) + D_m^h(P)\,D_m^h(B)\,Ai(-\bar{q}_m)\,e^{-j\int_B^P \gamma_m^h(s)\,ds}\cdot F(B)\right\}$
Slot Antenna (Soft Boundary)	$\frac{2}{Z_o}e^{jkr_s\cos(\theta-\theta_o)}$	$-\frac{2}{Z_o}\left[\frac{1}{k\rho_g}\right]_{\theta=\theta_p}\left\{\tilde{g}^*(\varepsilon_A)\,e^{-j\int_A^P k\,ds}\cdot F(A) + \tilde{g}^*(\varepsilon_B)\,e^{-j\int_B^P k\,ds}\cdot F(B)\right\}$	$-\frac{2\pi}{Z_o}\left[\left(\frac{k\rho_g}{2}\right)^{-2/3}\right]_{\theta=\theta_p} e^{-j\frac{\pi}{3}}\left(\frac{jk}{2\pi}\right)^{1/2}\sum_{m=1}^{\infty}\left\{D_m^s(P)\,D_m^s(A)\,Ai'(-q_m)\,e^{-j\int_A^P \gamma_m^s(s)\,ds}\cdot F(A) + D_m^s(P)\,D_m^s(B)\,Ai'(-q_m)\,e^{-j\int_B^P \gamma_m^s(s)\,ds}\cdot F(B)\right\}$
Infinitesimal Monopole	$-2\sin\theta\,e^{jkr_s\cos(\theta-\theta_o)}$	$\sin^{3/2}\theta\left\{g^*(\varepsilon_A)\,e^{-j\int_A^P k\,ds}\cdot F(A) + g^*(\varepsilon_B)\,e^{-j\int_B^P k\,ds}\cdot F(B)\right\}$	$-2\pi j\left[\left(\frac{k\rho_g}{2}\right)^{-1/3}\right]_{\theta=\theta_p} e^{j\frac{\pi}{3}}\left(\frac{jk}{2\pi}\right)^{1/2}\sum_{m=1}^{\infty}\left\{D_m^h(P)\,D_m^h(A)\,Ai(-\bar{q}_m)\,e^{-j\int_A^P \gamma_m^h(s)\,ds}\cdot F(A) - D_m^h(P)\,D_m^h(B)\,Ai(-\bar{q}_m)\,e^{-j\int_B^P \gamma_m^h(s)\,ds}\cdot F(B)\right\}$

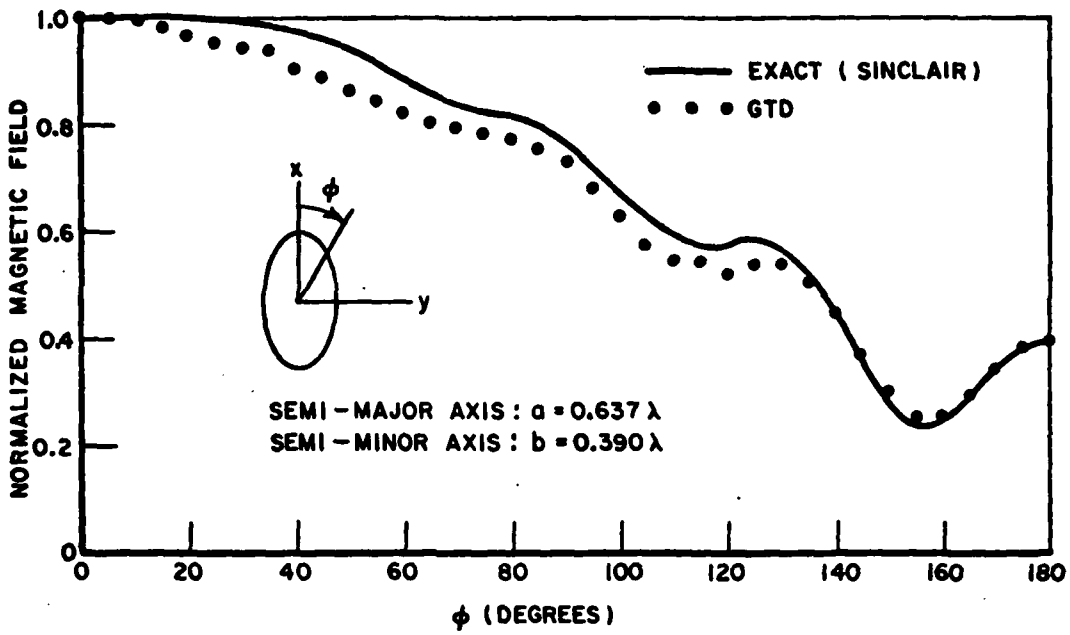

Fig. 18. Elevation plane patterns with a circumferential slot mounted on an elliptical cylinder.

It is noted that the propagation factor in the far field expression has the form $e^{-\gamma(a)s}$ for the circular cylinder case and $e^{-\int\gamma(s)ds}$ for the general convex surface case. Since the general formulations can not be calculated in a closed form due to the complicated expressions $\gamma(s)$ and/or S, the results, then, are often numerically performed via a modern high-speed digital computer. Hence, the integration is often performed through a discrete summation process to obtain the numerical result, i.e.,

$$\gamma(a)\, S \approx \sum_{i=1}^{n} \gamma(a) \cdot \Delta S_i = \gamma(a) \sum_{i=1}^{n} \Delta S_i \tag{96}$$

$$\int\gamma(s)\, ds \approx \sum_{i=1}^{n} \gamma(S_i) \cdot \Delta S_i \quad . \tag{97}$$

Based on the fact that the numerical computation in a digital computer is a discrete process and that an aircraft is generally specified by points in which no simple equation is available to give the complete description of the aircraft shape as mentioned previously, a new approach called "the section-matching method" has been developed. This method, by definition, is to match portions of a general surface through the use of a polynomial interpolation process. This method has proved very satisfactory in solving for the radiation pattern for an antenna mounted on any general convex body such as an aircraft fuselage which is our main interest in this report.

B. Section Matching Method

In order to predict the radiation pattern of an aircraft antenna mounted on a general convex fuselage, the section matching method can be applied. In this method the continuously curved surface of the fuselage is described by a set of discrete points. Thus, the generalized GTD formulations as shown in Table I now have to be modified so that they can be used for the discrete points case. For example, the equations for a circumferential slot are easily modified as follows:

1) Lit Region:

$$R_y(\theta) = 2\, e^{jkr_s\cos(\theta-\theta_o)} \tag{98}$$

2) Transition Region:

$$R_y(\theta) = g^*(\xi_A)\, F(A) \prod_{i=1}^{A} e^{-jk\Delta S_i} + g^*(\xi_B) \cdot F(B) \cdot \prod_{i=1}^{B} e^{-jk\Delta S_i} \tag{99}$$

3) Deep-Shadow Region:

$$R_y(\theta) = -2\pi j\left[\left(\frac{k\rho_g}{2}\right)^{-1/3}\right]_{\theta=\theta_p} e^{j\frac{\pi}{3}} \left(\frac{jk}{2\pi}\right)^{1/2} \tag{100}$$

$$\sum_{m=1}^{\infty} \left\{ D_m^h(P)\, D_m^h(A)\, Ai(-\bar{q}_m) \cdot F(A) \prod_{i=A}^{P} e^{-j\gamma_m^h(S_i)\Delta S_i} + D_m^h(P)\, D_m^h(B)\, Ai(-\bar{q}_m) \cdot F(B) \cdot \prod_{i=B}^{P} e^{-j\gamma_m^h(S_i)\Delta S_i} \right\}$$

where A, B and P are the launching points and source point, respectively; i is the index of the point lying between the launching points A or B and source point P; ΔS_i is the increment of ray path from point i to point (i+1); θ_p is the angle in the direction of the source point refered to the origin; and $\gamma_m^h(S_i)$ equals $[\alpha_m^h(S_i) + jk]$ and is the propagation constant at the point i for the hard boundary condition.

The generalized diffraction coefficient D_m and attenuation constant α_m as presented in Reference [15] are given in Table II below. Note that the diffraction coefficient and attenuation constant are functions of the longitudinal radius of curvature (ρ_g) along the ray trajectory, its first and second derivatives ($\dot{\rho}_g$ and $\ddot{\rho}_g$) with respect to arc length along the ray trajectory, and transverse radius of curvature (ρ_{tn}). In this two-dimensional analysis, ρ_{tn} is assumed to be infinite, hence the terms containing $\frac{1}{\rho_{tn}}$ in the expressions for D_m and α_m can be omitted. It is obvious that the logitudinal radius of curvature can not be obtained analytically from this discrete set of points, since no equation is given. One way to overcome this difficulty is to match sections of the fuselage surface using a numerical interpolatory approximation in which an (n-1)th order polynomial,

TABLE II

GENERALIZED DIFFRACTION COEFFICIENTS AND ATTENUATION CONSTANTS

Surface	Square of Diffraction Coefficient D_m^2 = (Column A) · (Column B)		Attenuation Constant α_m = (Column C) · (Column D)	
	A. Keller's Result	B. Correction Terms	C. Keller's Result	D. Correction Terms
Soft Acoustic and Soft EM	$\pi \dfrac{2^{-1/2} 2^{-5/6} \rho_g^{1/3} e^{-j\pi/12}}{k^{1/6} Ai'(-\bar{q}_m)^2}$	$1 + \left(\frac{2}{k\rho_g}\right)^{2/3} \bar{q}_m \left(\frac{1}{30} + \frac{\rho_g}{4\rho_{tn}} + \frac{\rho_g \bar{\rho}_g}{180}\right) e^{-j\pi/3}$	$\frac{\bar{q}_m}{\rho_g} e^{j\pi/6} \left(\frac{k\rho_g}{2}\right)^{1/3}$	$1 + \left(\frac{2}{k\rho_g}\right)^{2/3} \bar{q}_m \left(\frac{1}{60} - \frac{2}{45} \rho_g \bar{\rho}_g + \frac{4}{135} \rho_g^2\right) e^{-j\pi/3}$
Hard Acoustic	$\pi \dfrac{2^{1/2} 2^{-5/6} \rho_g^{1/3} e^{-j\pi/12}}{k^{1/6} \bar{q}_m (Ai(-\bar{q}_m))^2}$	$1 + \left(\frac{2}{k\rho_g}\right)^{2/3} \left(\bar{q}_m \left(\frac{1}{30} + \frac{\rho_g}{4\rho_{tn}} + \frac{\rho_g \bar{\rho}_g}{180}\right) - \frac{1}{\bar{q}_m^2} \left(\frac{1}{10} + \frac{\rho_g}{4\rho_{tn}} - \frac{\rho_g \bar{\rho}_g}{60}\right)\right) e^{-j\pi/3}$	$\frac{\bar{q}_m}{\rho_g} e^{j\pi/6} \left(\frac{k\rho_g}{2}\right)^{1/3}$	$1 + \left(\frac{2}{k\rho_g}\right)^{2/3} \left(\bar{q}_m \frac{1}{60} - \frac{2}{45} \rho_g \bar{\rho}_g + \frac{4}{135} \rho_g^2\right) + \frac{1}{\bar{q}_m^2} \left(\frac{1}{10} + \frac{\rho_g}{4\rho_{tn}} - \frac{\rho_g \bar{\rho}_g}{60} + \frac{\rho_g^2}{90}\right)\right) e^{-j\pi/3}$
Hard EM		$1 + \left(\frac{2}{k\rho_g}\right)^{2/3} \left(\bar{q}_m \left(\frac{1}{30} + \frac{\rho_g}{4\rho_{tn}} + \frac{\rho_g \bar{\rho}_g}{180}\right) - \frac{1}{\bar{q}_m^2} \left(\frac{1}{10} - \frac{\rho_g}{4\rho_{tn}} - \frac{\rho_g \bar{\rho}_g}{60}\right)\right) e^{-j\pi/3}$		$1 + \left(\frac{2}{k\rho_g}\right)^{2/3} \left(\bar{q}_m \left(\frac{1}{60} - \frac{2}{45} \rho_g \bar{\rho}_g + \frac{4}{135} \rho_g^2\right) + \frac{1}{\bar{q}_m^2} \left(\frac{1}{10} - \frac{\rho_g}{4\rho_{tn}} - \frac{\rho_g \bar{\rho}_g}{60} + \frac{\rho_g^2}{90}\right)\right) e^{-j\pi/3}$

which passes through n points in a given section, is determined. In other words, a continuous polynomial function is found numerically to approximate the actual curve so that at the points x_i, $i=1, 2, \cdots, n$, the approximation function agrees with the actual function $f(x)$. Once this polynomial is obtained, the radius of curvature can be determined without difficulty. The first and second derivatives of the radius of curvature can also be obtained simply by numerically differentiating with respect to the arc length. Hence, the diffraction coefficient and attenuation constant are known and Eqs. (98), (99), and (100) can be employed to calculate the radiation patterns.

In order to determine the required polynomial $y(x)$, the exact Lagrangian interpolation formula[20] is used. To interpolate n discrete points, the Lagrangian polynomial $y(x)$ should be of degree less than n with the property $y(a_i) = f(a_i)$, $i=0, \cdots, n-1$, where $f(x)$ is the original function or actual curve and a_i are the discrete points. Thus, the polynomial $y(x)$ can be written as

$$y(x) = c_0+c_1x+c_2x^2+\cdots+c_{n-1}x^{n-1} \quad . \tag{101}$$

At the discrete points a_i, $i=0, \cdots, n-1$,

$$y(a_i) = c_0+c_1a_i+c_2a_i^2+c_3a_i^3+\cdots+c_{n-1}a_i^{n-1} = f(a_i) \tag{102}$$

or

$$\begin{aligned} f(a_0) &= c_0+c_1a_0+c_2a_0^2+c_3a_0^3+\cdots+c_{n-1}a_0^{n-1} \\ f(a_1) &= c_0+c_1a_1+c_2a_1^2+c_3a_1^3+\cdots+c_{n-1}a_1^{n-1} \\ f(a_2) &= c_0+c_1a_2+c_2a_2^2+c_3a_2^3+\cdots+c_{n-1}a_2^{n-1} \\ &\cdot \\ &\cdot \\ f(a_{n-1}) &= c_0+c_1a_{n-1}+c_2a_{n-1}^2+c_3a_{n-1}^3+\cdots+c_{n-1}a_{n-1}^{n-1} \end{aligned} \tag{103}$$

where $f(a_i)$ is known.

Equation (103) is a system of n equations in terms of the n unknown c_i's. This system can be expressed in matrix form as

$$
(104) \qquad \begin{bmatrix} f(a_o) \\ f(a_1) \\ f(a_2) \\ \cdot \\ \cdot \\ \cdot \\ f(a_{n-1}) \end{bmatrix} = \begin{bmatrix} 1 & a_o & a_o^2 & a_o^3 & \cdots & a_o^{n-1} \\ 1 & a_1 & a_1^2 & a_1^3 & \cdots & a_1^{n-1} \\ 1 & a_2 & a_2^2 & a_2^3 & \cdots & a_2^{n-1} \\ \cdot & \cdot & \cdot & \cdot & & \cdot \\ \cdot & \cdot & \cdot & \cdot & & \cdot \\ \cdot & \cdot & \cdot & \cdot & & \cdot \\ 1 & a_{n-1} & a_{n-1}^2 & a_{n-1}^3 & \cdots & a_{n-1}^{n-1} \end{bmatrix} \begin{bmatrix} c_o \\ c_1 \\ c_2 \\ \cdot \\ \cdot \\ \cdot \\ c_{n-1} \end{bmatrix}
$$

or

$$
(105) \qquad y = Ac
$$

with

$$
(106) \qquad y = \begin{bmatrix} f(a_o) \\ f(a_1) \\ f(a_2) \\ \cdot \\ \cdot \\ \cdot \\ f(a_{n-1}) \end{bmatrix}
$$

$$
c = \begin{bmatrix} c_o \\ c_1 \\ c_2 \\ \cdot \\ \cdot \\ \cdot \\ c_{n-1} \end{bmatrix}
$$

$$A = \begin{bmatrix} 1 & a_0 & a_0^2 & \cdots & a_0^{n-1} \\ 1 & a_1 & a_1^2 & \cdots & a_1^{n-1} \\ 1 & a_2 & a_2 & \cdots & a_2^{n-1} \\ \cdot & \cdot & & & \cdot \\ \cdot & \cdot & & & \cdot \\ \cdot & \cdot & & & \cdot \\ 1 & a_{n-1} & a_{n-1}^2 & \cdots & a_{n-1}^{n-1} \end{bmatrix}$$

This linear system of equations can be solved by taking the inverse of matrix A, in which case

$$c = A^{-1}y \tag{107}$$

Once the unknowns c_i are found, the polynomial $y(x)$ is determined as in Eq. (101). The radius of curvature may be obtained from these equations using[21]

$$\rho_g = \frac{\left[1+\left(\frac{dy}{dx}\right)^2\right]^{3/2}}{\pm \frac{d^2y}{dx^2}} \tag{108}$$

or

$$\rho_g = \frac{\left[1+\left(\frac{dx}{dy}\right)^2\right]^{3/2}}{\pm \frac{d^2x}{dy^2}} \quad . \tag{109}$$

The ambiguous sign in Eqs. (108) and (109) is chosen so that ρ_g is always positive since the curve is convex.

Further, the first and second derivatives of the radius of curvature as required in the expressions of diffraction coefficient and attenuation constant are calculated by numerically differentiating the radius of curvature ρ_g with respect to the arc length s. Hence Eqs. (98) to (100) can now be applied. Consequently, the radiation patterns for an antenna mounted on a general convex fuselage can be obtained.

In order to illustrate the accuracy of this solution, the radiation patterns for an antenna mounted on circular, elliptical, and composite elliptical cylinders are calculated using this method. First these cylinders are described by discrete points which are generated by equations for a circle and ellipse. The points are generated in such a way that the angle difference between the tangent direction at any two adjacent points is less than 2 degrees. This is due to the fact that the surface ray sheds energy in the tangent direction and a reliable radiation pattern is likely to be obtained only if computed at intervals less than or equal to 2 degrees. The shedding angle (tangent angle) at any point on the fuselage can be found approximately by the following relation (see Fig. 19).

$$\theta = \alpha - \beta. \tag{110}$$

where

$$\alpha = \tan^{-1} \frac{|y_{i+1} - y_i|}{|x_{i+1} - x_i|}$$

$$\beta = \sin^{-1} \sqrt{\frac{(x_{i+1} - x_i)^2 + (y_{i+1} - y_i)^2}{2\rho_{gi}}}$$

and ρ_{gi} is the radius of curvature at point i. However, ρ_{gi} is an unknown quantity but it can be found easily as will be discussed later. Therefore, one should use a trial and error method to generate and

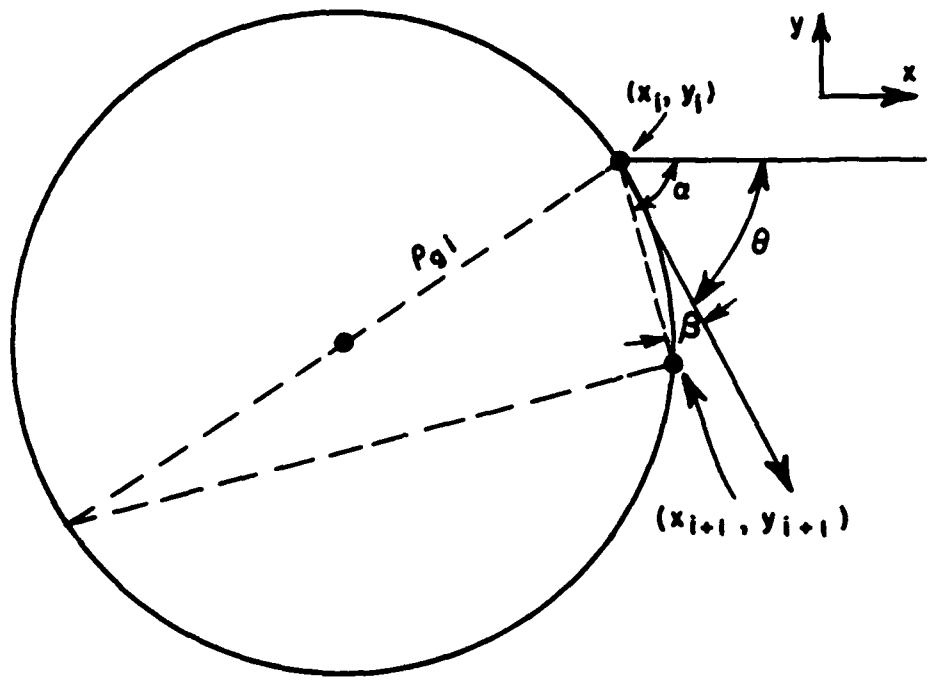

Fig. 19. Determination of shedding angle.

test the discrete set of points from the analytic equations in order to obtain a sufficient number of points to describe the model. After obtaining the required discrete points, the radius of curvature ρ_g and its first two derivatives $\dot{\rho}_g$ and $\ddot{\rho}_g$ are found according to the method just discussed.

A Lagrangian interpolation polynomial of degree n-1, where n is chosen to be an odd number for our application, is used to approximate the function which passes through any n sequential points on the surface. In other words, one is trying to match a section, which contains these n points, of the geometry of particular interest (fuselage) by an (n-1)th order polynomial approximation. After the desired polynomial is obtained, Eq. (108) or Eq. (109) is employed to find the radius of curvature at the center point of this section. The

same procedure is applied and continued until the radius of curvature at every point on the surface is found. It is noted that the degree of Lagrangian polynomial must be n-1 or less for this interpolation to be exact, i.e., the error at these n points is zero. Note also that the computer time required to solve n linear equations is proportional to n^3. Using the Crout method to solve the n x n matrix, the computer time is reduced and proportional to n^2. It takes approximately one-fourth the time to solve n/2 equations than it does to solve n equations. Thus, for the sake of computer time, it is wise to choose the number n as small as possible. However, the accuracy with which the polynomial function approximates the actual surface also should be taken into careful consideration. Since the geometry of our interest is quite smooth, high-order polynomials are not necessarily required. A polynomial of degree 4 (or n=5) is thus chosen to interpolate the sections of our present fuselage models.

To illustrate the accuracy of our section matching interpolation, the calculated results of radius of curvature and its first two derivatives from a set of discrete points generated from a composite ellipse with two different semi-ellipses placed back to back is presented in Table III. Due to the symmetry, only half of the data is shown. Notice that the radius of curvature ρ_d calculated from discrete points compares well with ρ_c of the analytic equation of the ellipses except at θ=90° where the two ellipses are joined together. The inaccurate data for the derivatives around θ=90° and θ=270° resulted from the error accumulation due to the discontinuous radii of curvature used in the differentiations. In practice, this data can be set to equal to zeros, since its effect is so small that one can ignore it. Using these results for the radius of curvature and its derivatives along with Eqs. (98), (99), and (100), the radiation pattern in the elevation plane for various antennas mounted on circular cylinders with radius a=1λ and a=5λ are calculated and presented in Figs. 20 to 25. Only the dominant creeping wave terms with the first two modes are considered in these patterns. Notice that excellent agreement is

TABLE III

COMPOSITE ELLIPSE (a=2.0 b=0.5 c=4.0)

$\theta°$	ρ_c	ρ_d	$\dot{\rho}_c$	$\dot{\rho}_d$	$\ddot{\rho}_c$	$\ddot{\rho}_d$
0	0.125000	0.125000	0.0	0.00	22.5	22.493027
5	0.535155	0.535156	-3.507460	-3.506249	10.832942	10.840757
10	1.829328	1.829360	-5.298786	-5.296271	3.087004	3.099108
15	3.385806	3.385434	-5.611507	-5.602857	-0.518659	-0.453016
20	4.680069	4.680116	-5.250263	-5.248033	-2.413772	-2.402165
25	5.624736	5.624709	-4.684848	-4.680745	-3.501232	-3.535900
30	6.291131	6.291201	-4.102222	-4.100489	-4.169641	-4.178182
40	7.100539	7.100552	-3.078533	-3.077841	-4.898717	-4.893385
50	7.530519	7.530523	-2.260492	-2.260237	-5.255688	-5.253419
60	7.771503	7.771510	-1.590659	-1.590547	-5.447772	-5.446614
70	7.907789	7.907797	-1.015261	-1.015208	-5.554036	-5.553343
80	7.978184	7.978191	-0.494959	-0.494937	-5.608276	-5.607783
90	7.999997	12.800099	-0.000001	-824.250901	-5.624997	11834.8320
100	31.977036	31.977060	0.520462	0.520457	-5.901922	-5.901795
110	31.902405	31.902448	1.072628	1.072616	-5.887842	-5.887655
120	31.755432	31.755494	1.696152	1.696123	-5.860015	-5.859694
130	31.487198	31.487221	2.451000	2.450929	-5.808909	-5.808264
140	30.979645	30.979704	3.442989	3.442778	-5.711161	-5.709542
150	29.907730	29.907842	4.885924	4.885040	-5.499908	-5.494330
160	27.146667	27.147224	7.257616	7.250326	-4.922618	-4.900683
170	17.579269	17.581758	11.146346	11.122554	-2.387525	-2.318478
175	6.324325	6.301114	11.098542	10.779890	3.471679	2.321958
180	0.062500	0.062500	0.000119	-0.000000	47.250000	47.241440

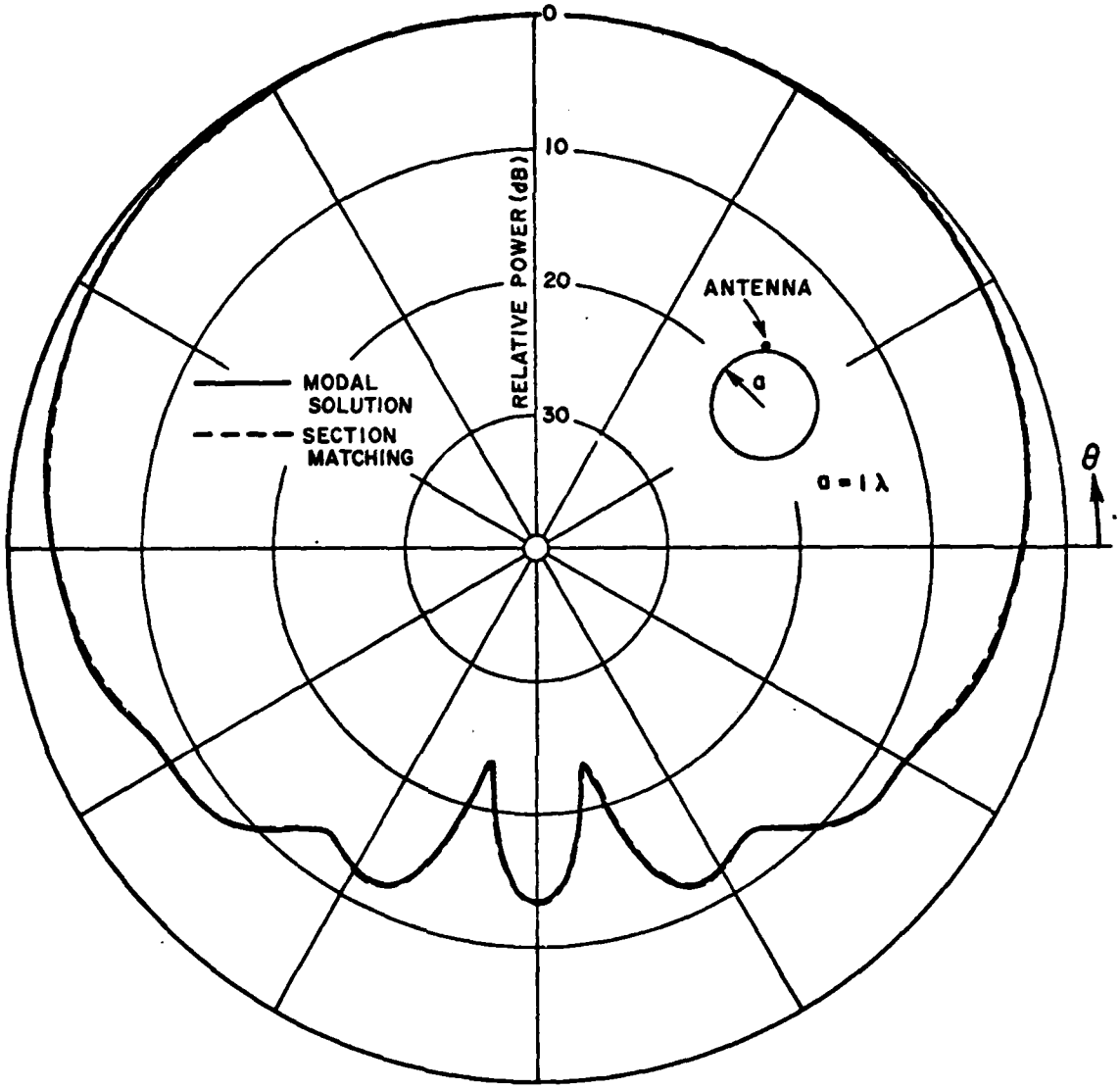

Fig. 20. Elevation plane patterns with a circumferential slot mounted on a circular cylinder.

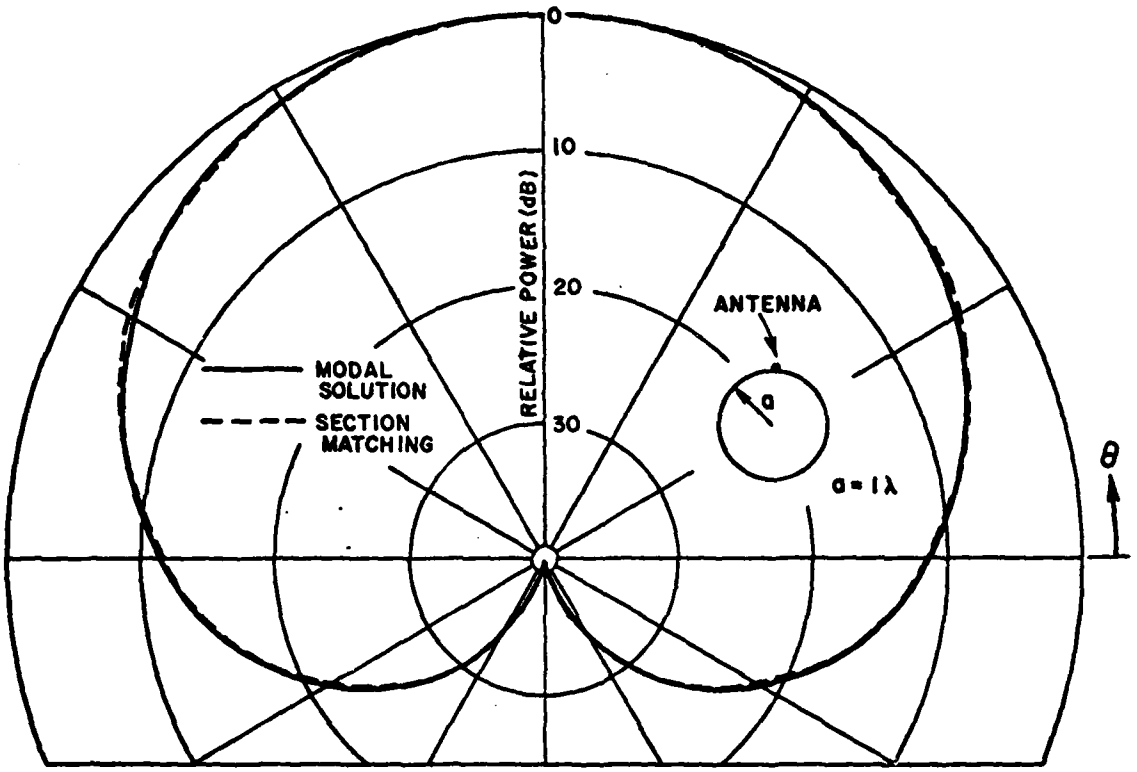

Fig. 21. Elevation plane patterns with an axial slot mounted on a circular cylinder.

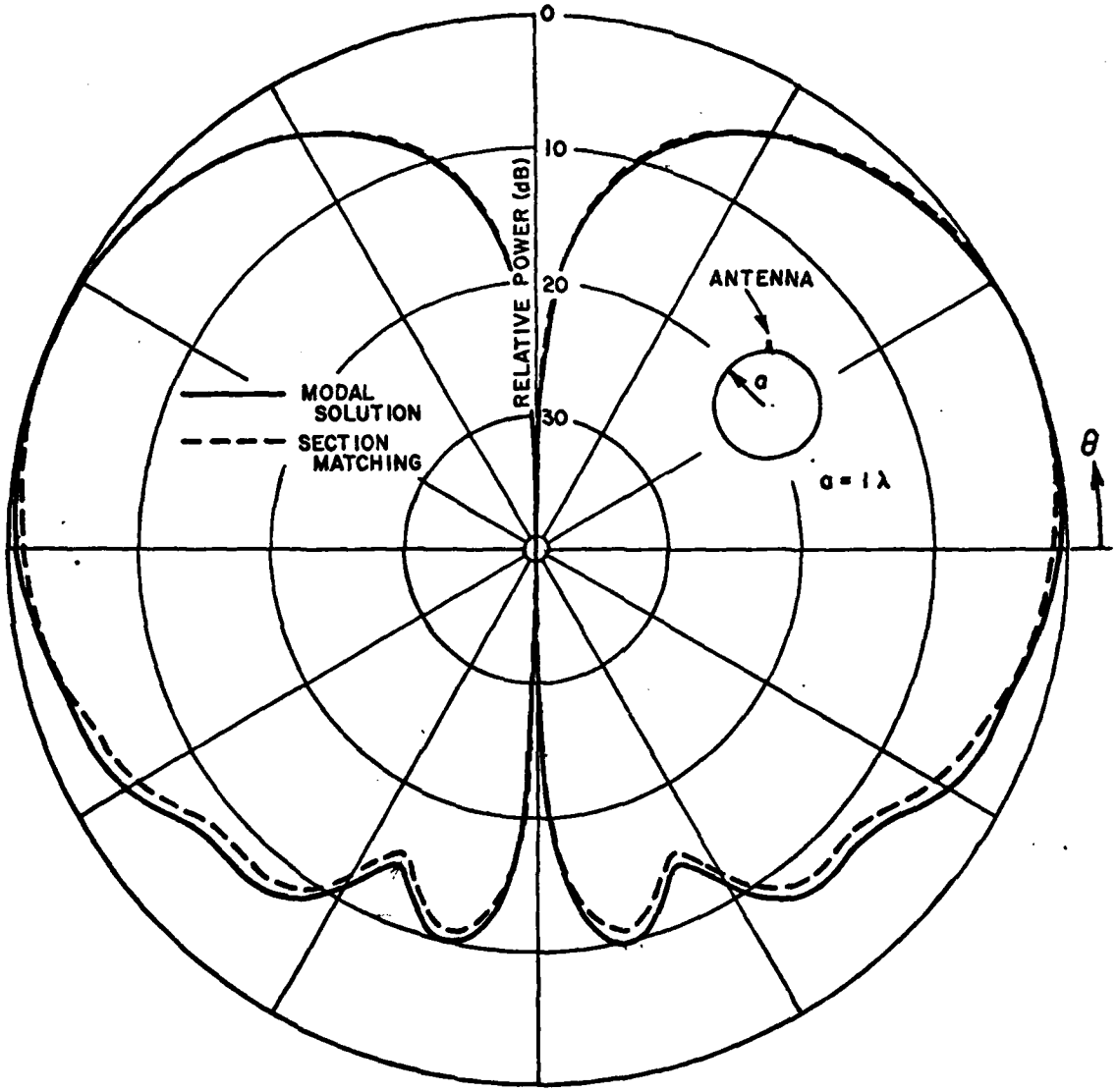

Fig. 22. Elevation plane patterns with an infinitesimal monopole mounted on a circular cylinder.

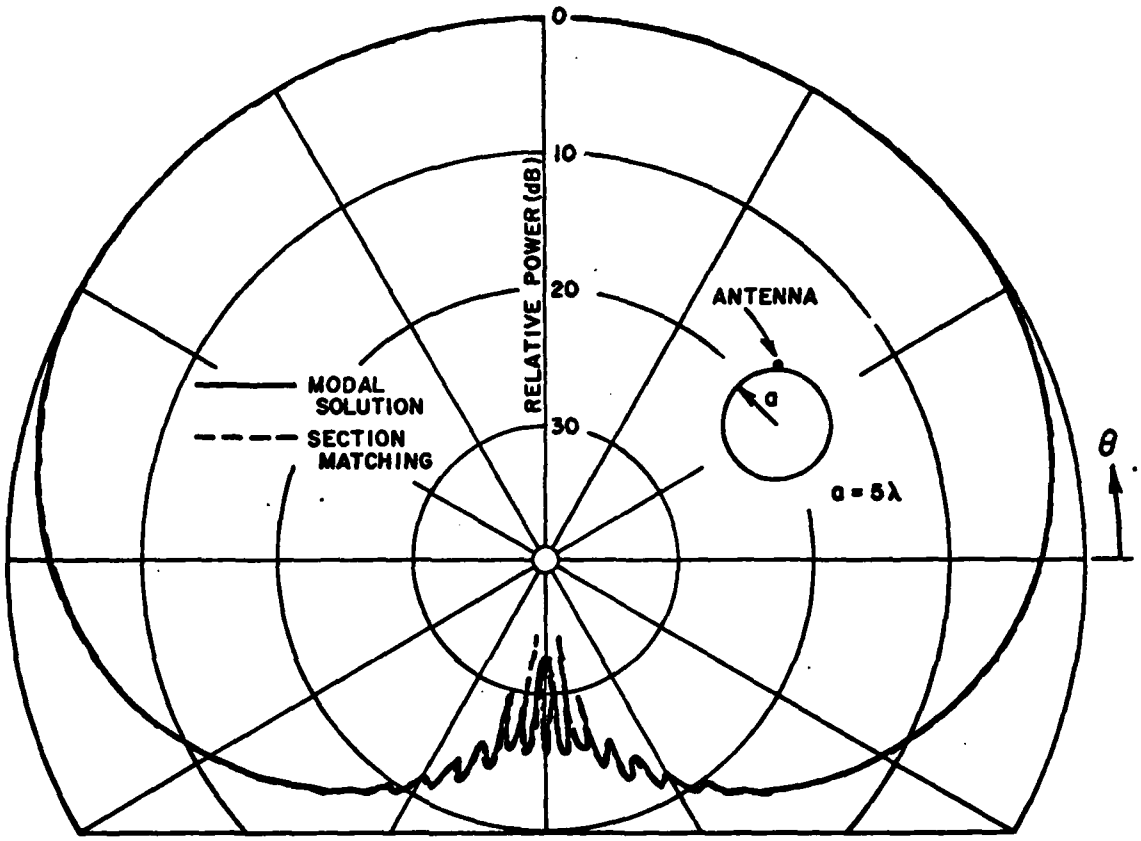

Fig. 23. Elevation plane patterns with a circumferential slot mounted on a circular cylinder.

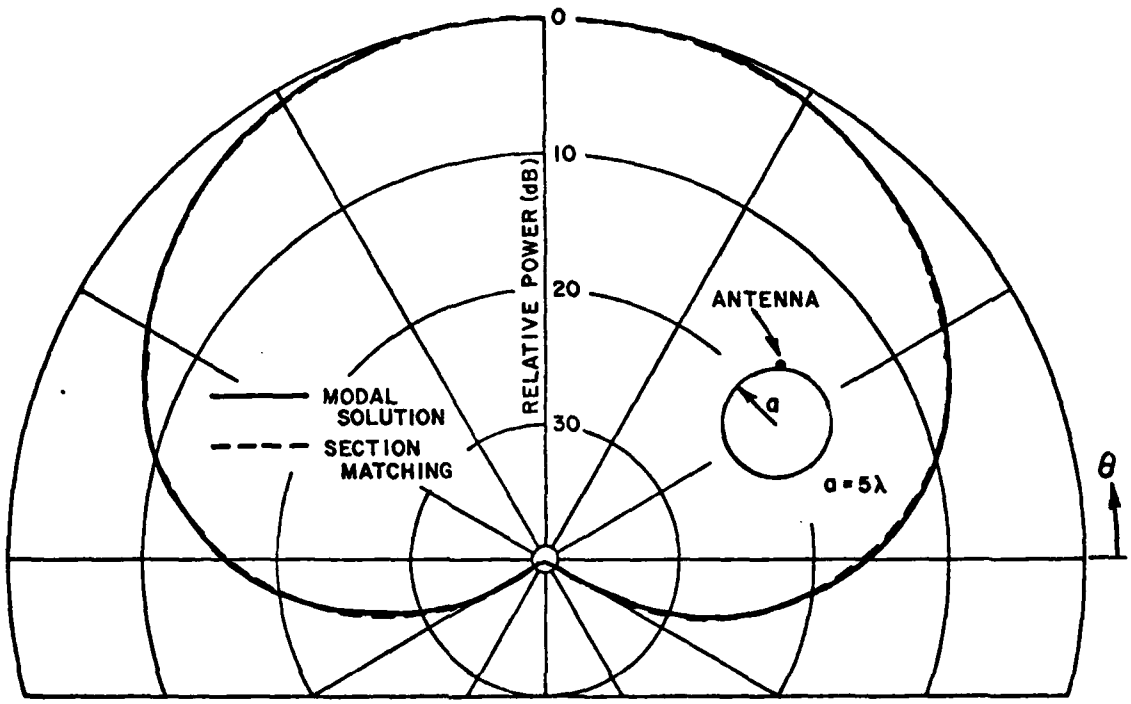

Fig. 24. Elevation plane patterns with an axial slot mounted on a circular cylinder.

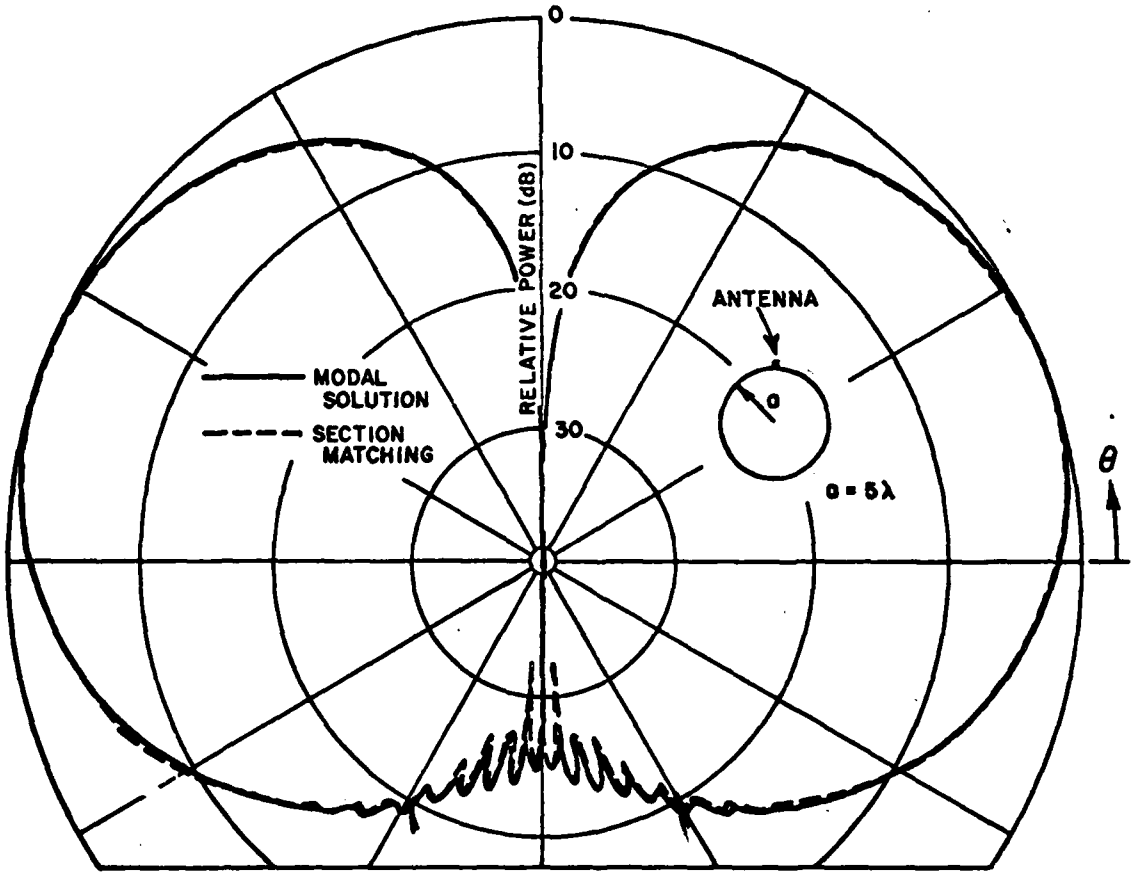

Fig. 25. Elevation plane patterns with an infinitesimal monopole mounted on a circular cylinder.

observed between these patterns and those obtained using the modal solution. These results illustrate the validity of the section matching method for this simple model.

This section matching method now is extended to obtain radiation patterns in the elevation plane for a simulated fuselage model with an elliptical profile. The calculated radiation patterns for general antennas such as circumferential slot, axial slot and infinitesimal monopole mounted on an infinitely long elliptical cylinder with a semi-major axis $a=0.637\lambda$ and semi-minor axis $b=0.390\lambda$ are shown in Figs. 26 to 28. The comparison between the continuous GTD solution and the section matching method, again, is very satisfactory. In addition this latter method has been applied to more general fuselage models such as composite elliptical cylinders. The radiation patterns in the elevation plane for a circumferential slot mounted at various locations on a composite elliptical cylinder are shown in Fig. 29. The results, again, compare very favorably with the more rigorous GTD solution [19]. The elevation plane patterns for axial slot and infinitesimal monopole are also shown in Figs. 30 and 31, respectively. Based on these results, the pattern in the illumination region is simply the direct radiation by the antenna itself. On the other hand, the pattern in the shadow region is completely dominated by the fuselage structure through the diffraction mechanisms. Thus, the complete radiation pattern for an antenna mounted on a fuselage is greatly affected by the fuselage as one should expect. The location at which the antenna is mounted is also an important factor in predicting the radiation pattern. Therefore, one should foresee a better forward coverage for slot antennas located at the front portion of the fuselage. The radiation patterns in the elevation plane for a smaller composite elliptical fuselage, such as $a_1=1.5\lambda$ and $a_2=2.0\lambda$ and $b=0.5\lambda$, are presented in Fig. 32. From the comparison between Figs. 29a, 30a, 31a, and 32 one notices that there are fewer backlobes but more energy radiated in the shadow region for the smaller cylinder. The larger cylinder has more backlobes at a lower average energy

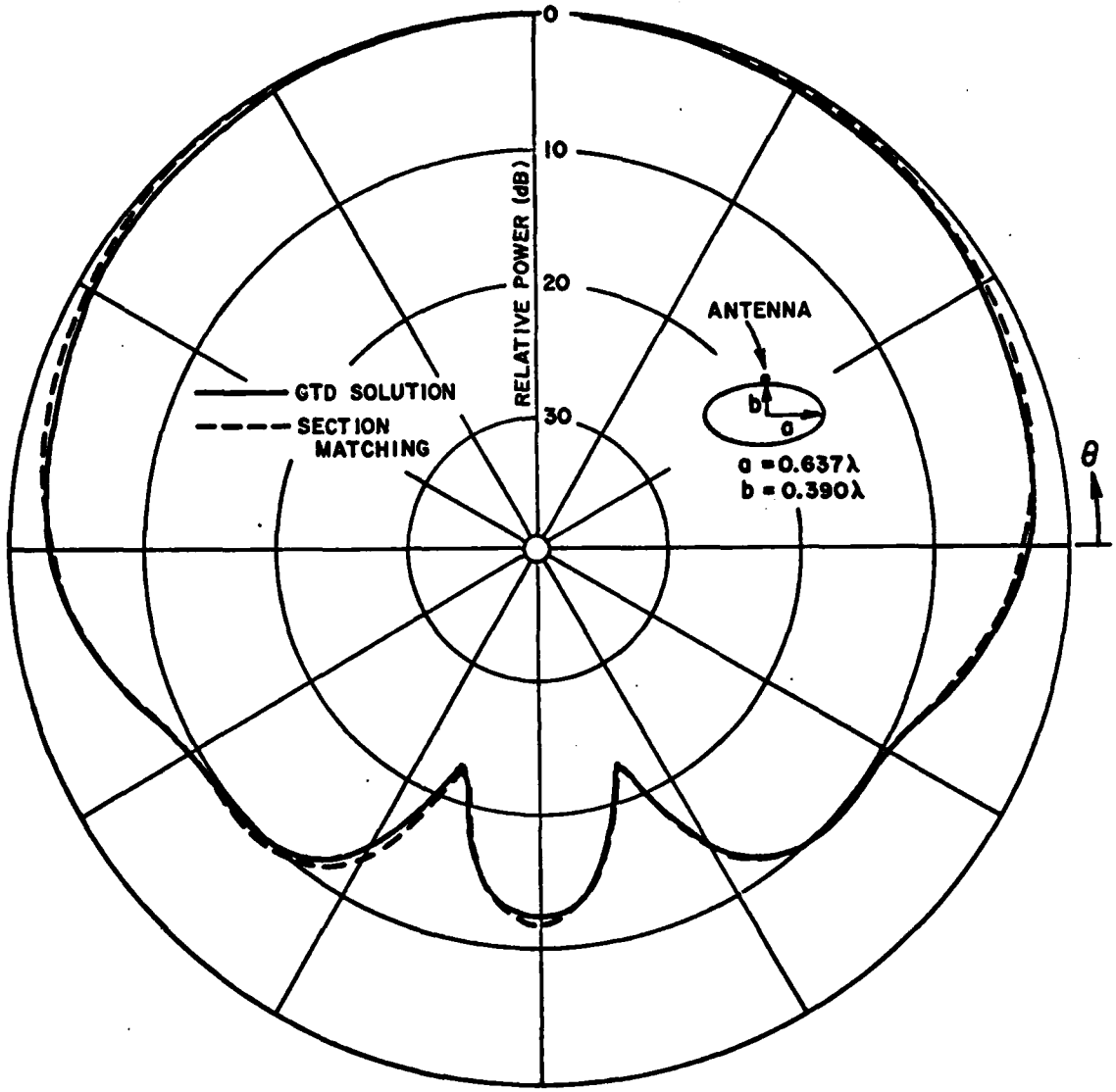

Fig. 26(a). Elevation plane patterns with a circumferential slot mounted on an elliptical cylinder.

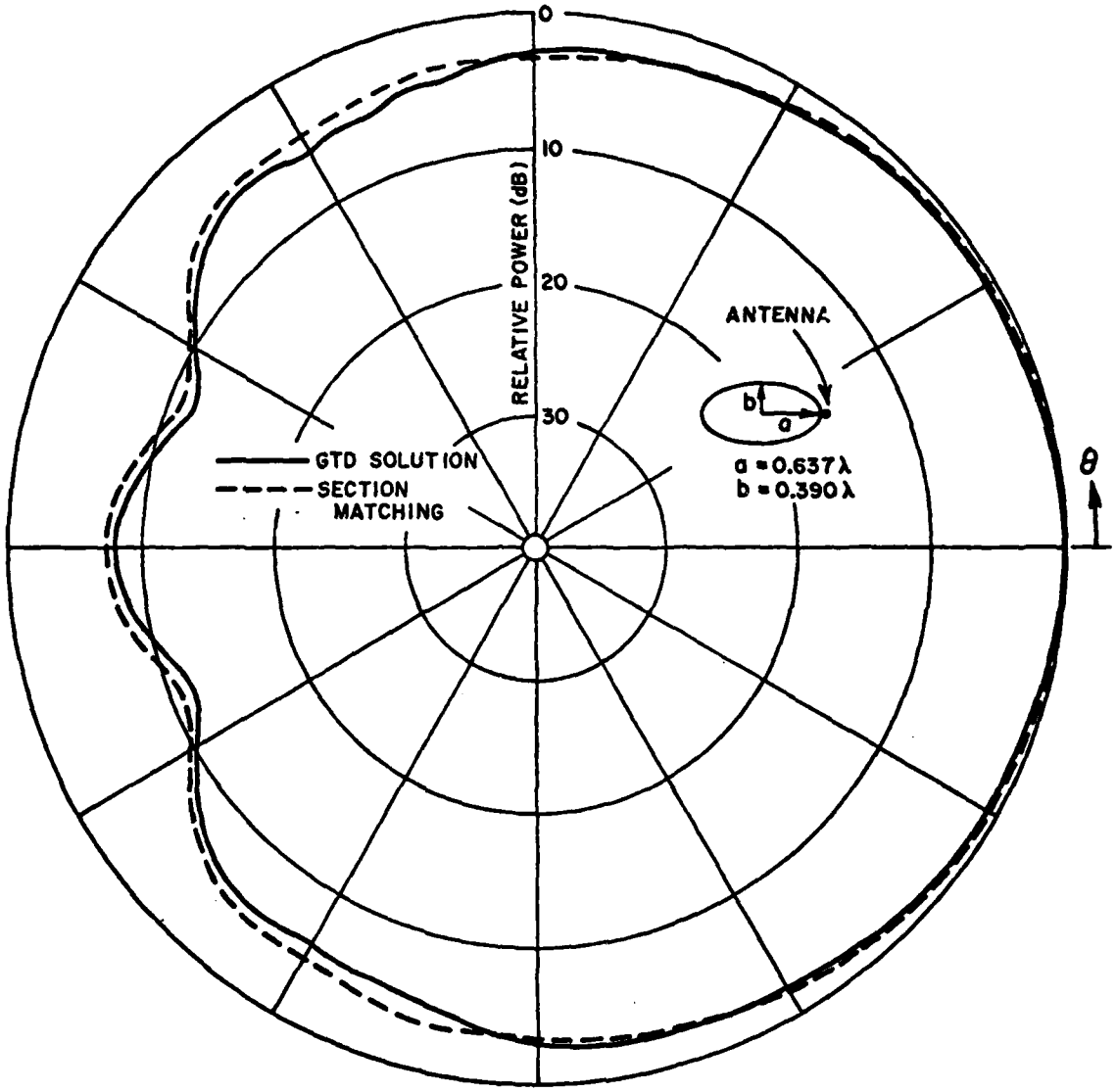

Fig. 26(b). Elevation plane patterns with a circumferential slot mounted on an elliptical cylinder.

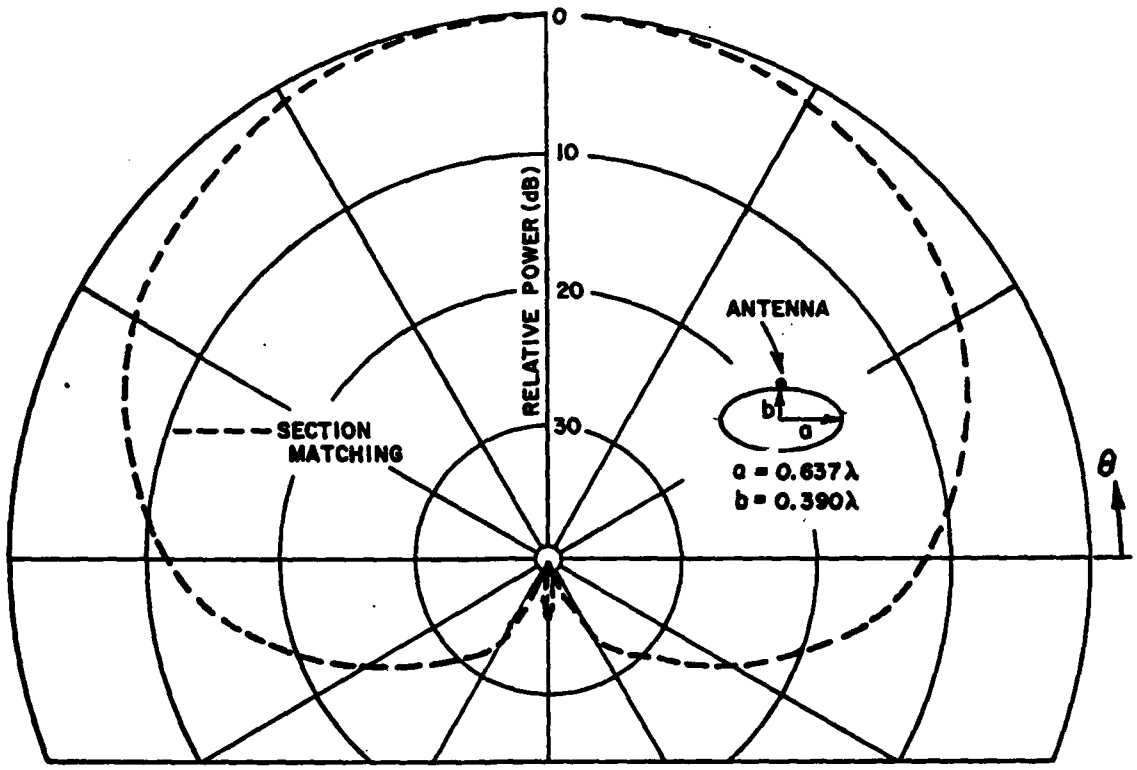

Fig. 27. Elevation plane pattern with an axial slot mounted on an elliptical cylinder.

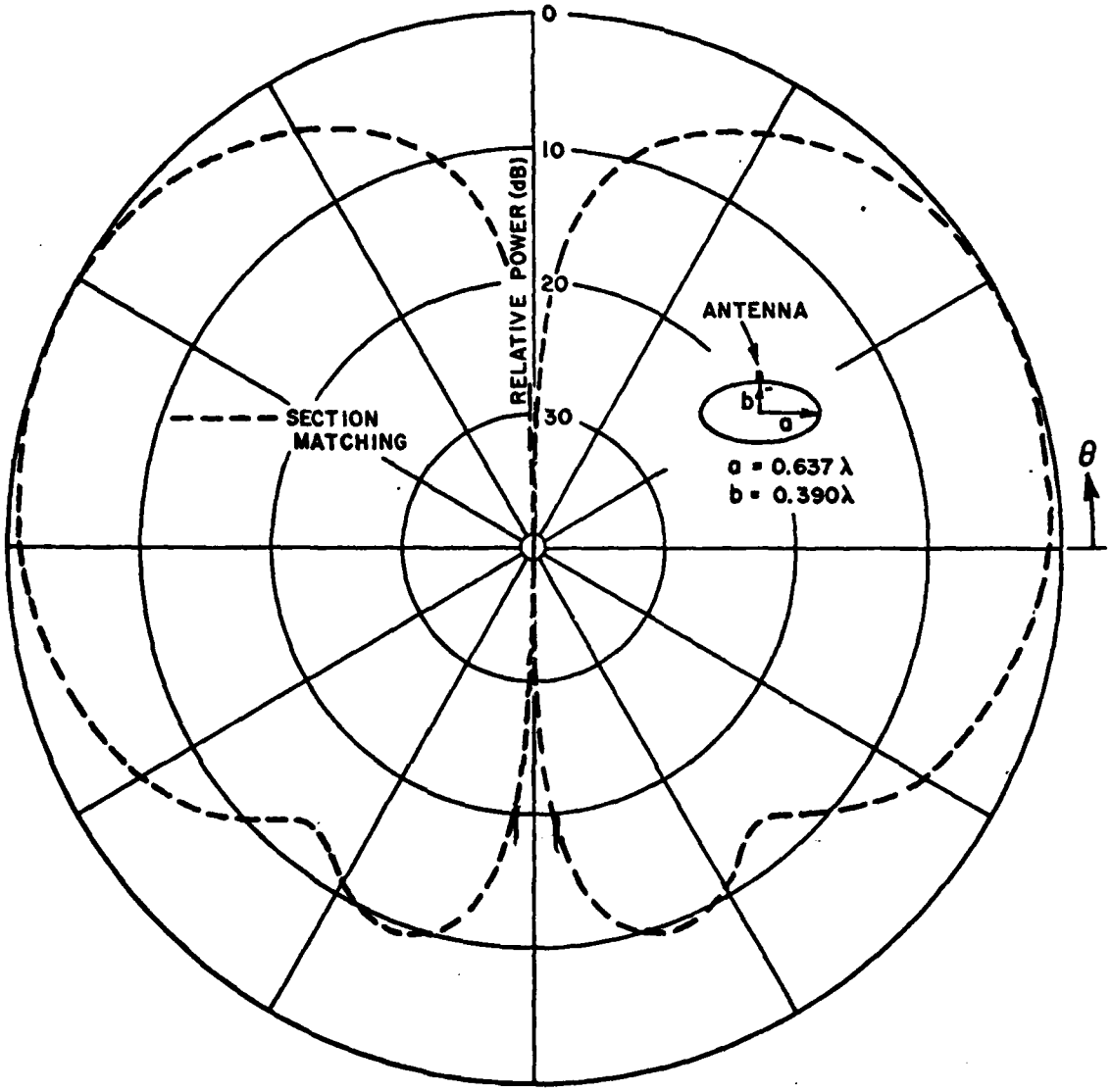

Fig. 28. Elevation plane pattern with an infinitesimal monopole mounted on an elliptical cylinder.

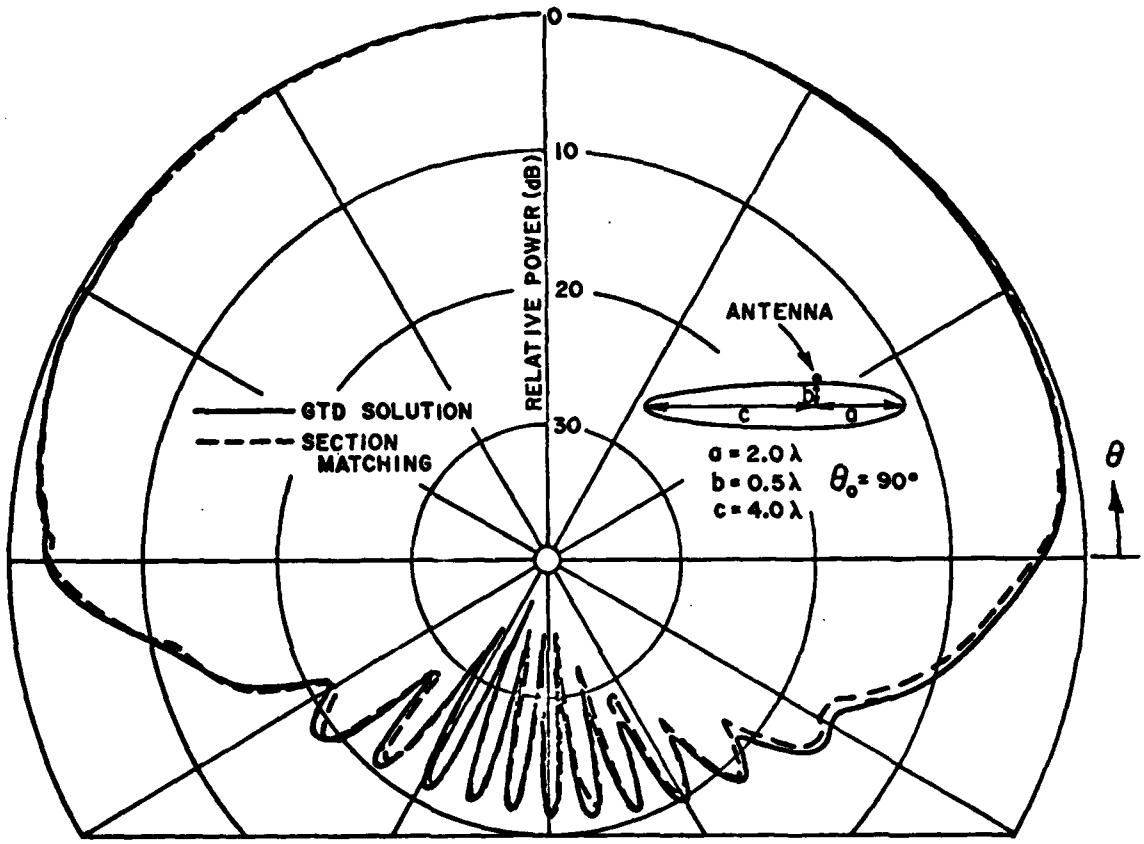

Fig. 29(a). Elevation plane pattern with a circumferential slot mounted on a composite ellipse model.

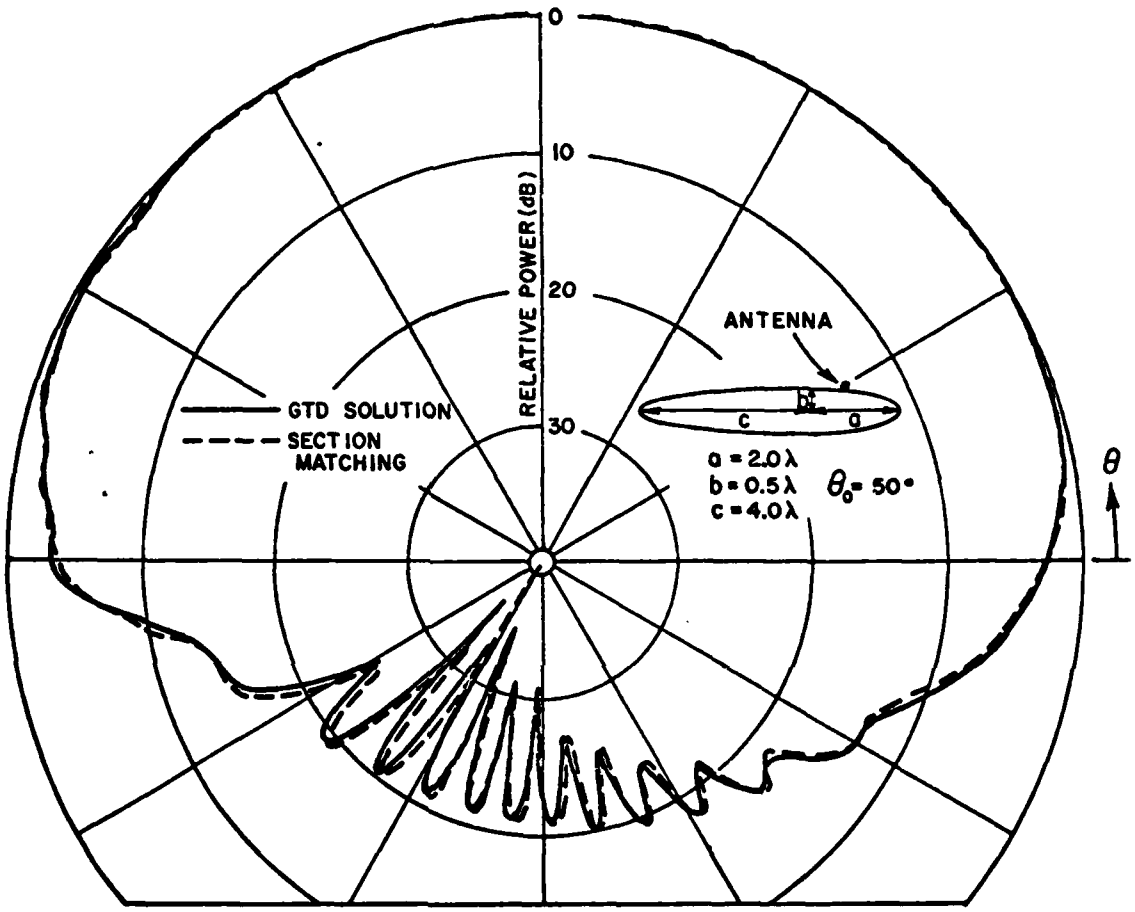

Fig. 29(b). Elevation plane pattern with a circumferential slot mounted on a composite ellipse model.

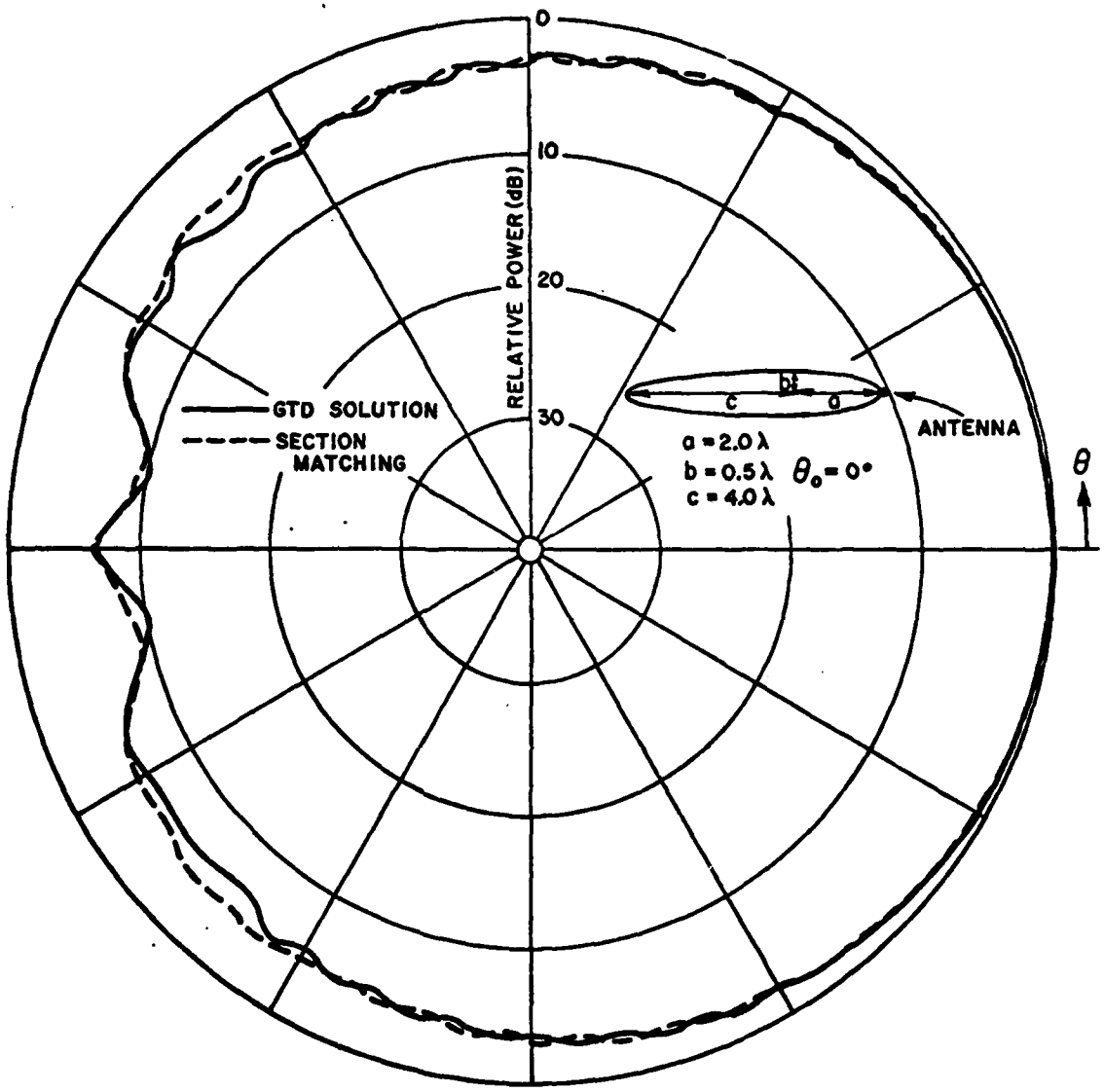

Fig. 29(c). Elevation plane pattern with a circumferential slot mounted on a composite ellipse model.

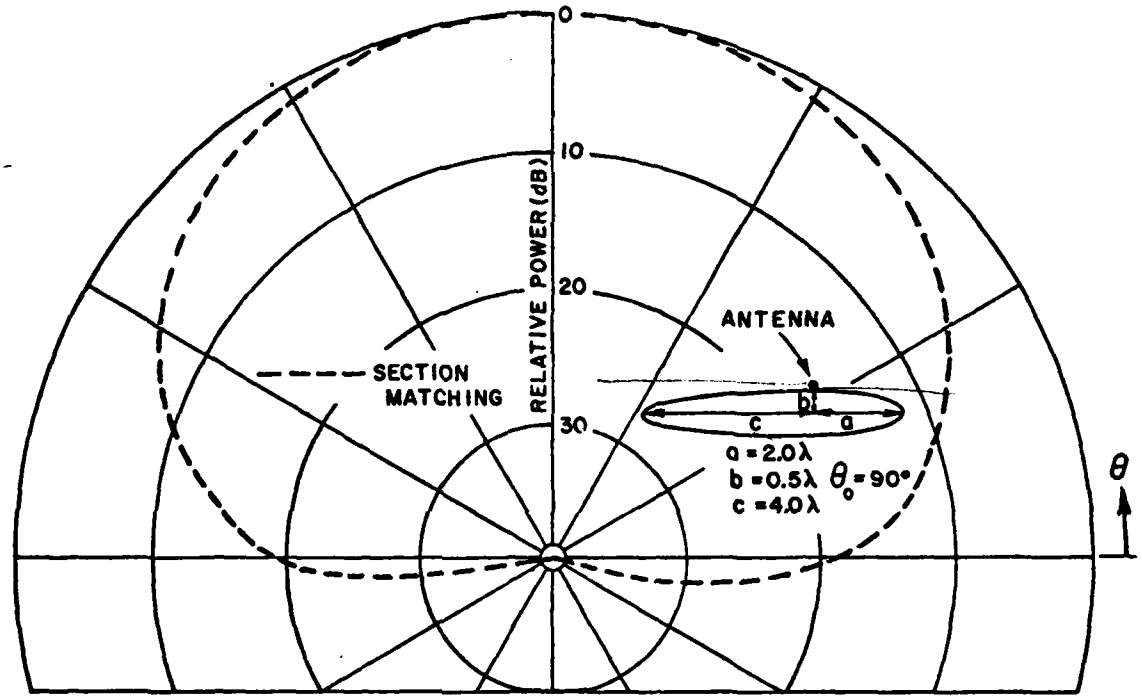

Fig. 30(a). Elevation plane pattern with an axial slot mounted on a composite ellipse model.

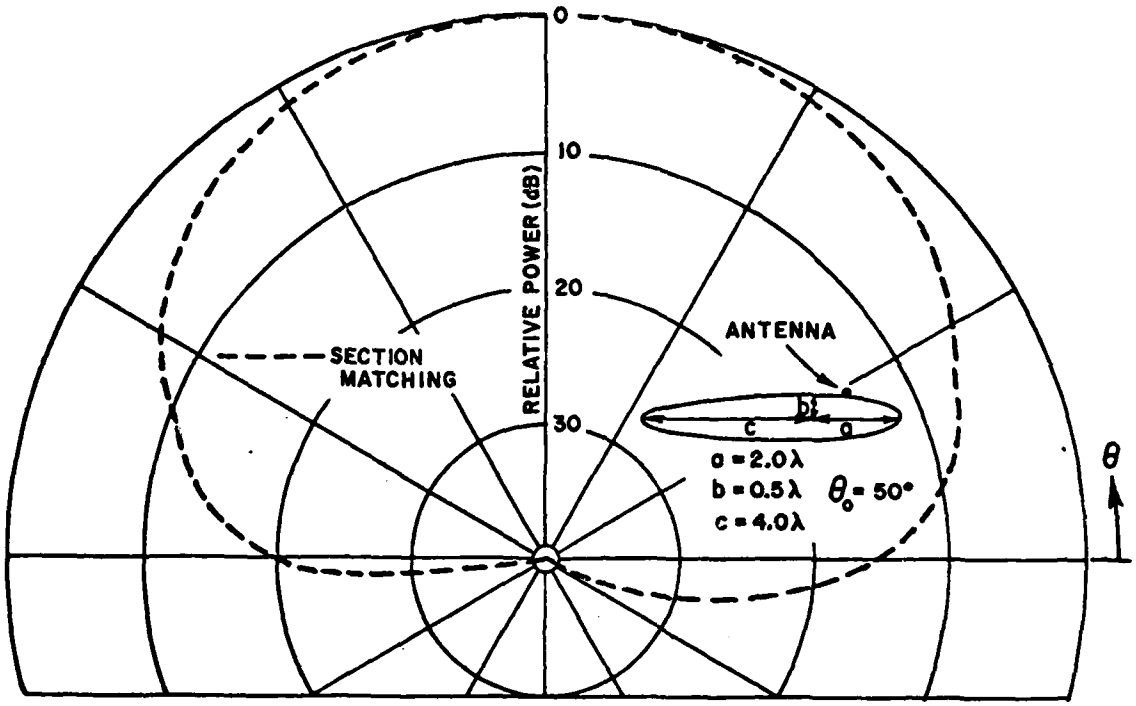

Fig. 30(b). Elevation plane pattern with an axial slot mounted on a composite ellipse model.

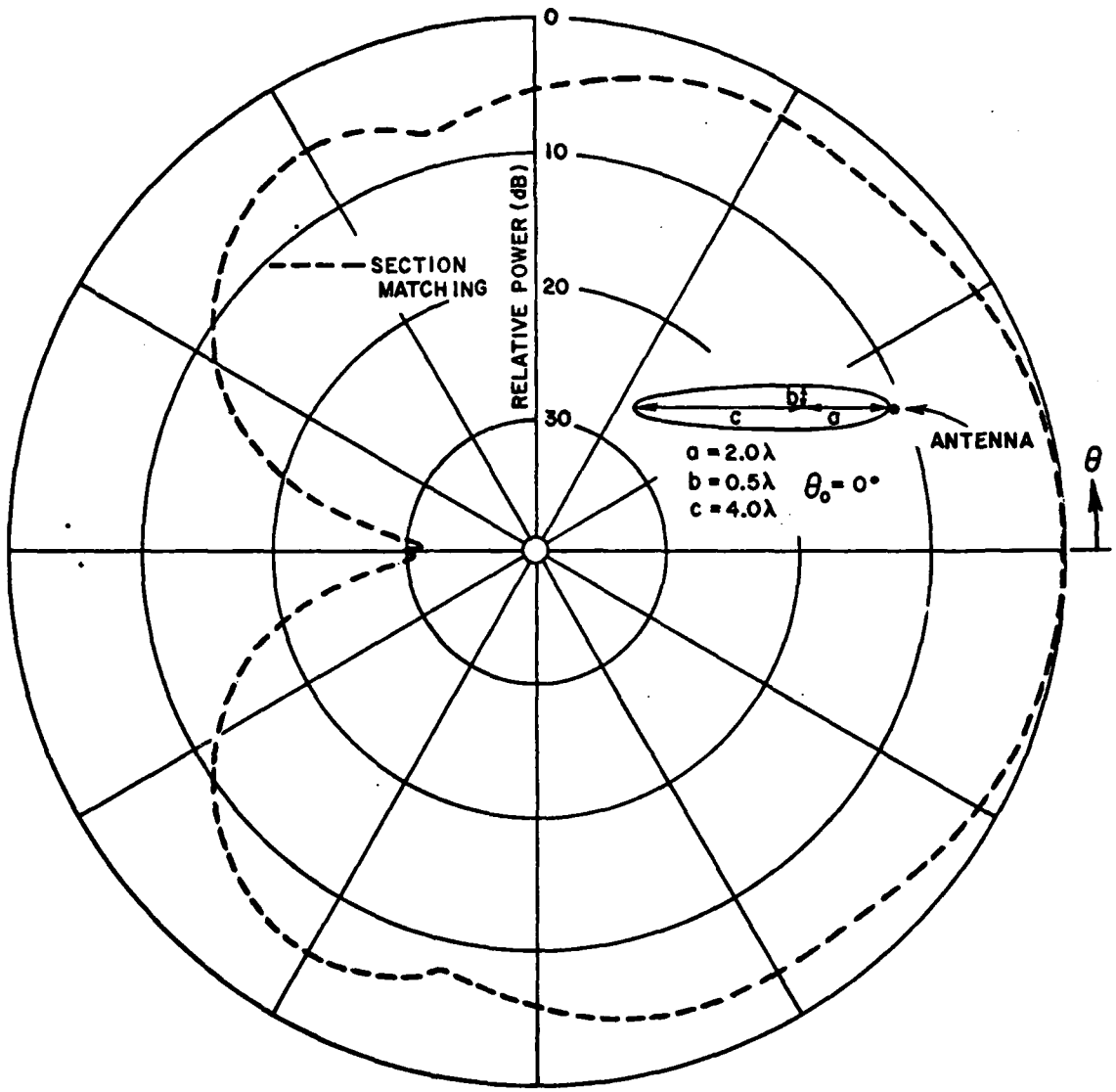

Fig. 30(c). Elevation plane pattern with an axial slot mounted on a composite ellipse model.

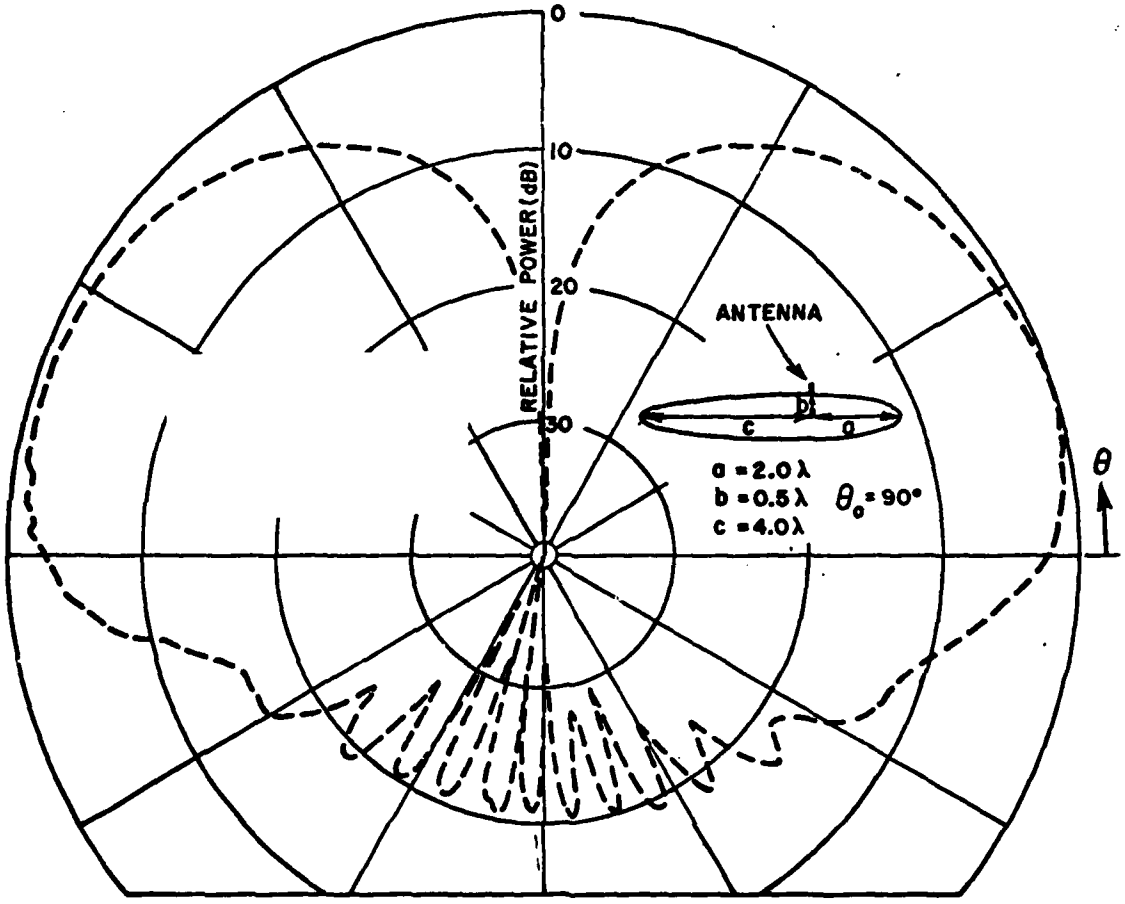
0
10
20
30
RELATIVE POWER (dB)
ANTENNA
b
c
a
a = 2.0 λ
b = 0.5 λ
c = 4.0 λ
θ_0 = 90°
θ

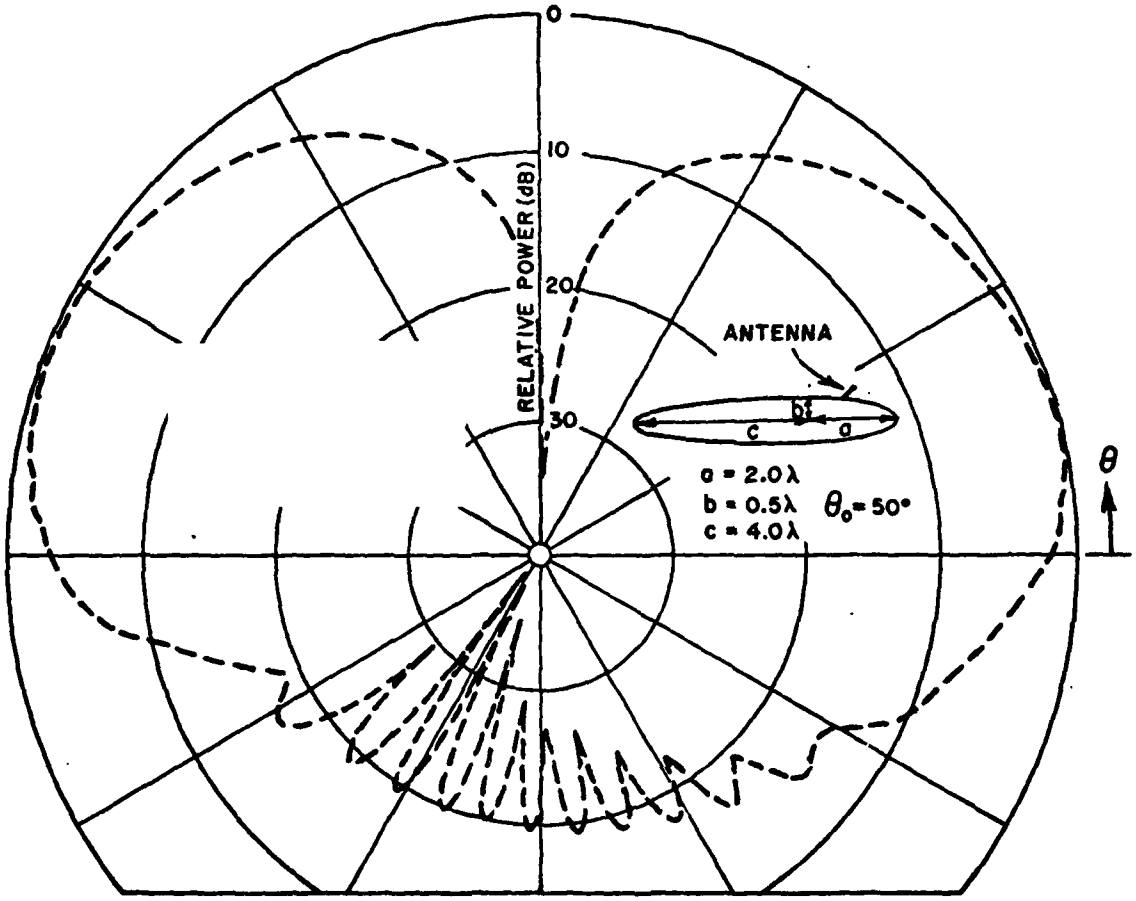
0
10
20
30
RELATIVE POWER (dB)
ANTENNA
b
c
a
a = 2.0λ
b = 0.5λ
c = 4.0λ
θ_0 = 50°
θ

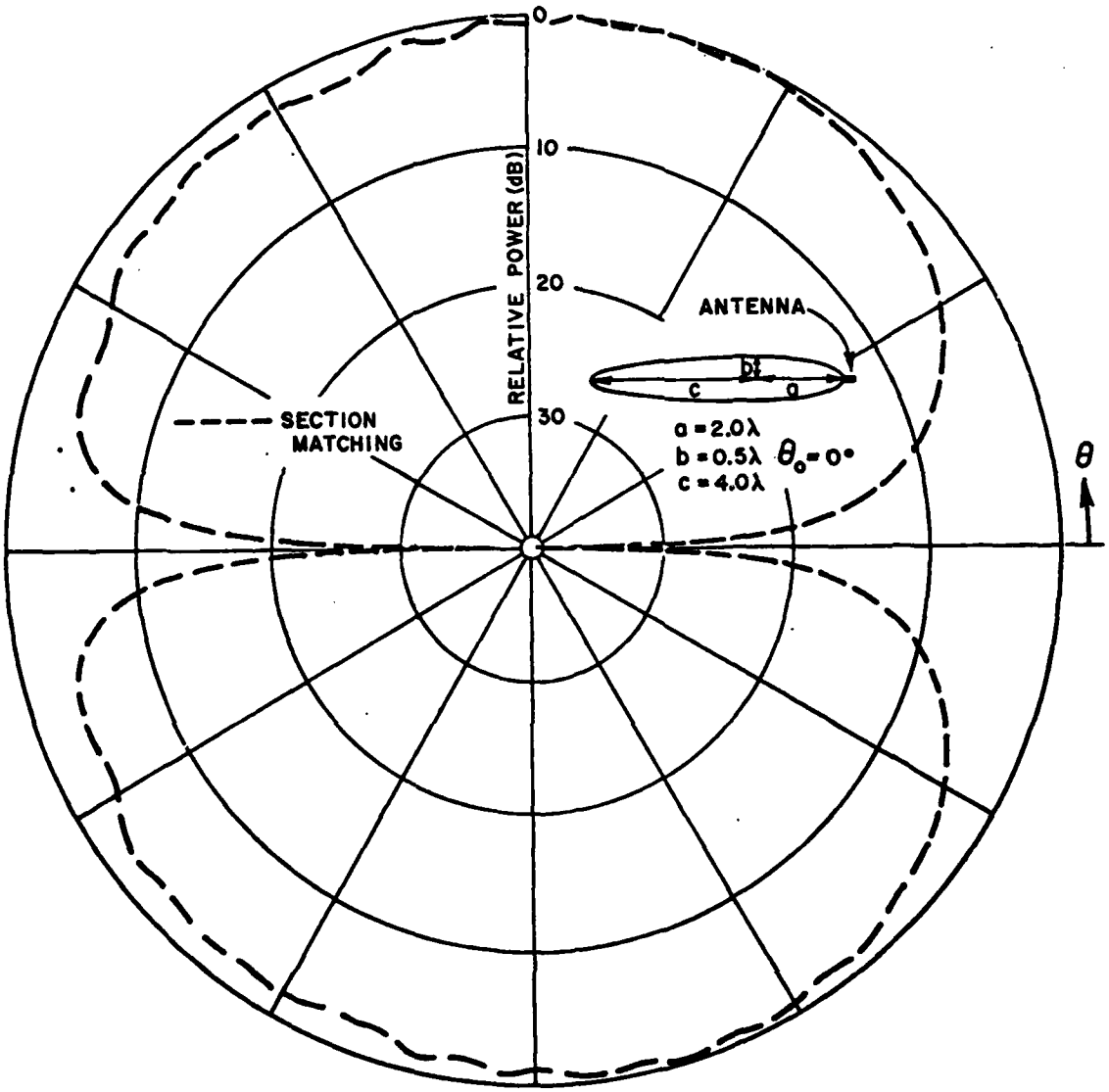

Fig. 31.(c). Elevation plane pattern with an infinitesimal monopole mounted on a composite ellipse model.

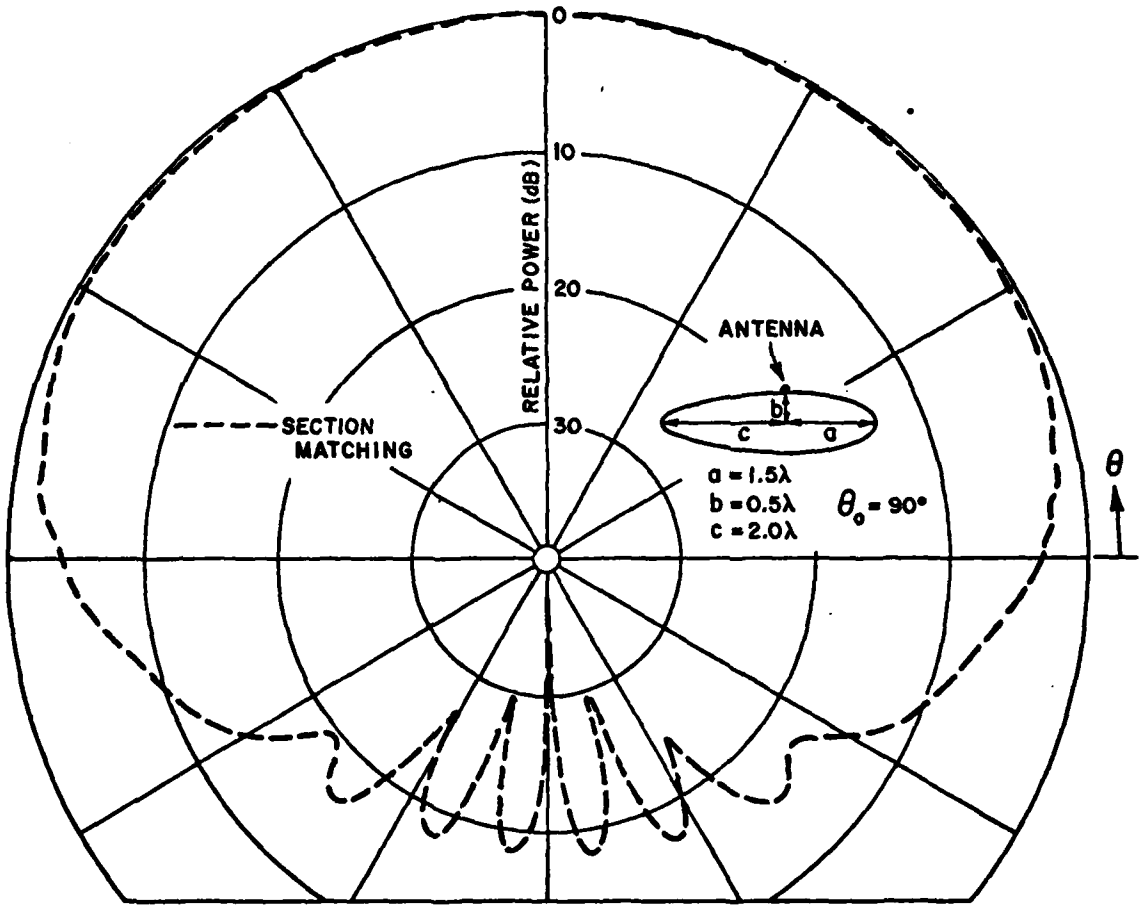

Fig. 32(a). Elevation plane pattern with a circumferential slot mounted on a composite ellipse model.

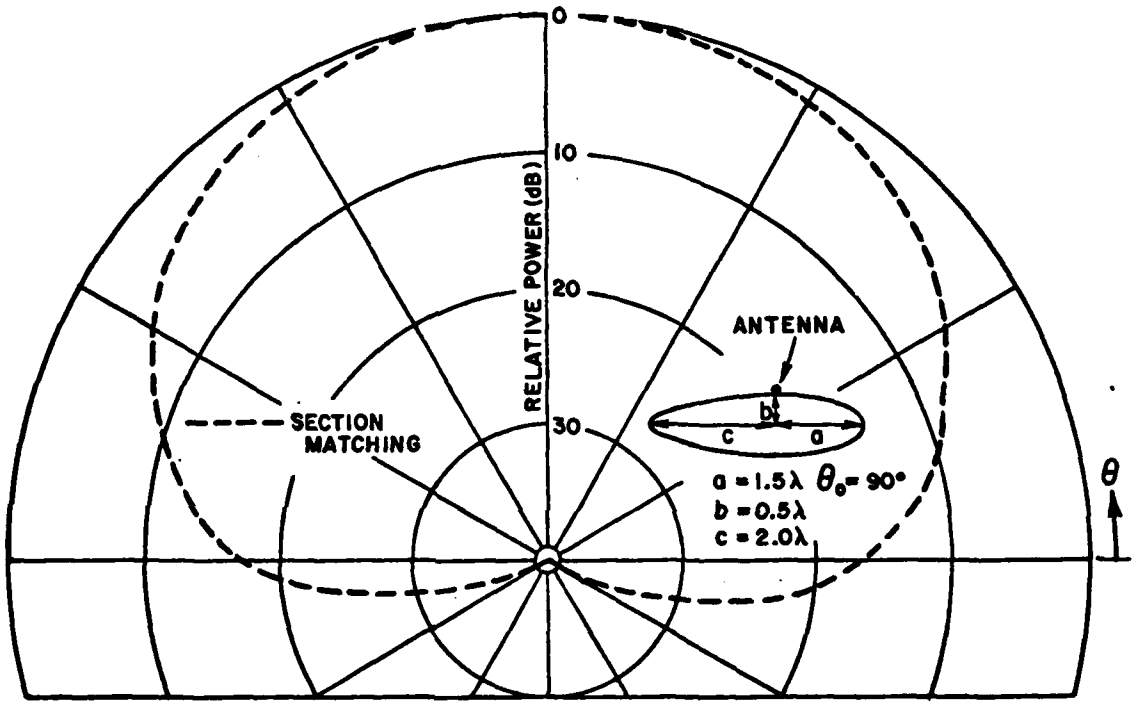

Fig. 32(b). Elevation plane pattern with an axial slot mounted on a composite ellipse model.

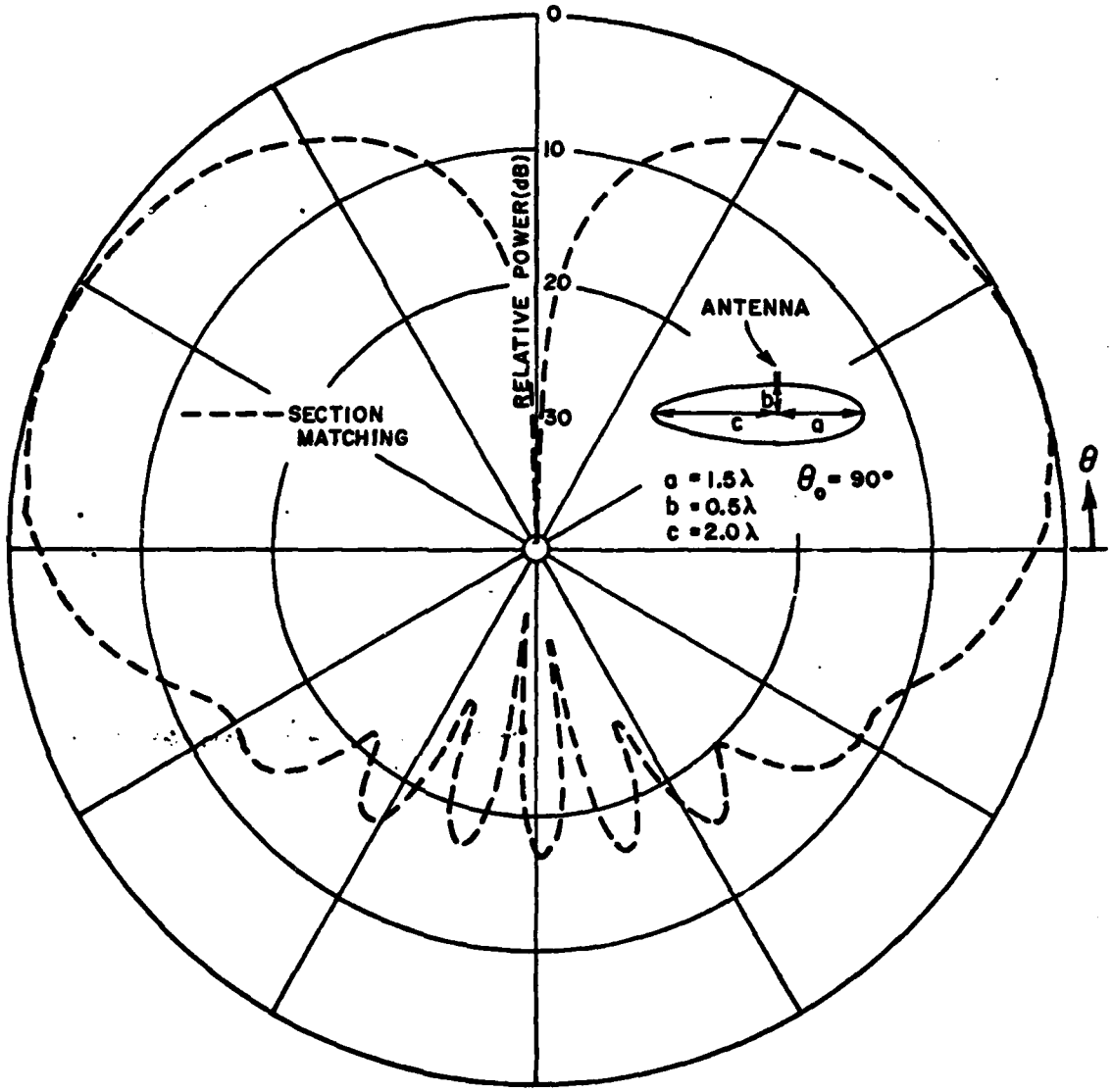

Fig. 32(c). Elevation plane pattern with an infinitesimal monopole mounted on a composite ellipse model.

level. This is simply due to the size of the fuselage and the interaction between the two surface waves propagating in the opposite directions from the source in which case the two ray paths play a most important role. That is, the longer the ray path is, the more the surface ray attenuates. Again, this shows the significant effect which the structure of the aircraft fuselage plays in terms of the antenna's performance. Therefore, an antenna designer should take the structure of aircraft into careful consideration in the design of airborne antennas in order to achieve his specific needs for a given application.

V. CONCLUSIONS

Modern diffraction theory in the form of the geometrical theory of diffraction (GTD) and its extensions including wedge diffraction theory and creeping wave theory is employed to analyze the elevation patterns of airborne antennas mounted on the aircraft fuselage. Some simple models composed of cylinders and cones are first used to simulate the fuselage so that wedge diffraction theory could be applied to calculate the radiation patterns in the elevation plane for antennas, such as a circumferential slot, an axial slot and a radial monopole, mounted on the fuselage. Based on this study, it was found that the fuselage shape has a dominant effect on the elevation plane radiation pattern. The radiation patterns calculated through these models compare very favorably with the measured results. In order to introduce the curvature of an actual fuselage, the theoretical models are modified to include curved surfaces. A combination of wedge diffraction techniques and creeping wave theory, then, was applied to solve the new geometry. Again, the effect of fuselage is clearly shown in the radiation patterns.

In order to include a more general geometry for a fuselage, a new approach has been developed in which the fuselage profile is described by a set of points. With this and a more rigorous "GTD" solution, the radiation pattern in the elevation plane for an antenna

mounted on the fuselage can be calculated. This method, called "the section matching method," is essentially a numerical interpolation in sections described by a set of points which defines the profile of the aircraft fuselage. With this interpolating technique the radius of curvature and its first two derivatives at the discrete points are found numerically. Consequently, the generalized "GTD" solution which is a function of the radius of curvature of the fuselage can be modified to obtain the radiation patterns for a fuselage outlined by discrete points.

In order to illustrate the accuracy of this solution, the section matching method is applied to circular, elliptical and composite elliptical cylinders in which the composite elliptical cylinder is considered to be a convenient model for simulating an aircraft fuselage. With the radiation patterns calculated from this method and a modal solution, excellent agreement is achieved for the circular cylinder case. The results for elliptical and composite elliptical cylinders also compare very favorably with the more rigorous continuous GTD solutions. These good results verify the validity of this section matching method. Based on this study one concludes that the pattern in the illuminated region is simply the direct radiation by the antenna itself whereas that in the shadow region is completely dominated by the fuselage structure through the diffraction mechanisms. Thus, the aircraft structure has a significant and, often, dominant effect on the antenna system performance especially when the fuselage is strongly illuminated. Therefore, in designing antenna systems for airborne applications, the antenna designers should take the aircraft structure into careful consideration in order to achieve their specific objectives.

REFERENCES

1. Keller, J.B., "Geometrical Theory of Diffraction," J. Opt. Soc. Am., Vol. 52, No 2, February 1962, pp. 116-130.

2. Kouyoumjian, R.G., "An Introduction to Geometrical Optics and the Geometrical Theory of Diffraction," Antenna and Scattering Theory: Recent Advances Short Courses, Department of Electrical Engineering, The Ohio State University, August 1965 and August 1966.

3. Rudduck, R.C., "Application of Wedge Diffraction to Antenna Theory," Report 1691-13, 30 June 1965, ElectroScience Laboratory, Department of Electrical Engineering, The Ohio State University; prepared under Grant NsG-448, for National Aeronautics and Space Administration.

4. Ryan, C.E., Jr. and Peters, L., Jr., "Evaluation of Edge Diffracted Fields Including Equivalent Currents for the Caustic Regions," IEEE Transactions on Antennas and Propagation, Vol. AP-17, No. 3, May 1969.

5. Sommerfeld, A., Optics - Lectures on Theoretical Physics, Vol. IV, Academic Press, New York, 1964, p. 245.

6. Pauli, W., "An Asymptotic Series for Functions in the Theory of Diffraction of Light," Phys. Rev., 54, 1 December 1938, pp. 924-931.

7. Hutchins, D.L. and Kouyoumjian, R.G., "A New Asymptotic Solution to the Diffraction by a Wedge," URSI 1967 Spring Meeting, Ottawa, Canada, pp. 154-155.

8. Hutchins, D.L., "Asymptotic Series Describing the Diffraction of a Plane Wave by a Two-Dimensional Wedge of Arbitrary Angle," Ph.D. Dissertation, The Ohio State University Electrical Engineering Department, 1967.

9. Ryan, C.E., Jr., "Analysis of Radiation Patterns of Antennas on Finite Circular Cylinders and Conically-Capped Cylinders," Report 2805-2, 25 September 1970, ElectroScience Laboratory, Department of Electrical Engineering, The Ohio State University; prepared under Contract DAAA21-69-C-0535 for Picatinny Arsenal, Dover, New Jersey.

10. Kouyoumjian, R.G., "Asymptotic High-Frequency Methods," Proceedings of the IEEE, Vol. 53, No. 8, August 1965, pp. 864-876.

11. Kouyoumjian, R.G., "A Note on the Caustic Associated with Edge Diffraction," to be submitted for publication.

12. Levy, B.R. and Keller, J.B., "Diffraction by a Smooth Object," Institute of Mathematical Sciences, New York University, published under Contract Number AF19(604)-1717; December 1957. Also in Comm. Pure Appl. Math., 12, 1959, pp. 159-209.

13. Franz, W. and Depperman, K., "Theorie der Beugang Am Zylinder unter Berücksichtigung der Kreichwelle," Ann. Physik, Vol. 10, June 1952, pp. 361-373.

14. Franz, W. and Depperman, K., "Theorie der Beugang der Kugel unter Berücksichtigung der Kreichwelle," Ann Physic, Vol. 14, June 1954, pp. 253-264.

15. Voltmer, D.V., "Diffraction by Doubly Curved Convex Surfaces," Ph.D. Dissertation, The Ohio State University, 1970.

16. Yu, C.L., "Wedge Diffraction Analysis of Antennas on Simulated Wing Models," Report 2836-3, September 1970, ElectroScience Laboratory, Department of Electrical Engineering, The Ohio State University; prepared under Contract No. N62269-69-C-0533 for Naval Air Development Center, Johnsville, Warminister, Pa. 18974.

17. Kouyoumjian, R.G., Notes in preparation for publication.

18. Fock, V.A., Electromagnetic Diffraction and Propagation Problems, Pergamon Press, 1965.

19. Don, C., "Radiation Patterns of Narrow Slots on Cylindrical Surfaces," Internal Memorandum, July 1971, ElectroScience Laboratory, The Chio State University.

20. Sinclair, G, "The Patterns of Antennas Located Near Cylinders of Elliptical Cross Section," Proceedings of IRE, Vol. 39, No. 6, June 1951.

21. Ralston, A., A First Course in Numerical Analysis, McGraw-Hill Book Co., Inc., New York, 1965.

22. Thomas, G.B., Jr., Calculus and Analytic Geometry, Addison-Wesley Publishing Co., Inc., 1960.

23. National Bureau of Standards, Handbook of Mathematical Functions, 1964.

UNCLASSIFIED
Security Classification

DOCUMENT CONTROL DATA - R&D

(Security classification of title, body of abstract and indexing annotation must be entered when the overall report is classified)

1. ORIGINATING ACTIVITY *(Corporate author)* ElectroScience Laboratory
Department of Electrical Engineering, The Ohio State University, Columbus, Ohio

2a. REPORT SECURITY CLASSIFICATION
Unclassified

2b. GROUP

3. REPORT TITLE
ELEVATION PLANE ANALYSIS OF ON-AIRCRAFT ANTENNAS

4. DESCRIPTIVE NOTES *(Type of report and inclusive dates)*
Technical Report

5. AUTHOR(S) *(Last name, first name, initial)*
Chong L. Yu and Walter D. Burnside

6. REPORT DATE
January 1972

7a. TOTAL NO. OF PAGES
87

7b. NO. OF REFS
23

8a. CONTRACT OR GRANT NO.
N62269-71-C-0296

b. PROJECT NO.

c. TASK

d.

9a. ORIGINATOR'S REPORT NUMBER(S)
ElectroScience Laboratory 3188-2

9b. OTHER REPORT NO(S) *(Any other numbers that may be assigned this report)*

10. AVAILABILITY/LIMITATION NOTICES
DISTRIBUTION STATEMENT A
Approved for public release;
Distribution Unlimited

11. SUPPLEMENTARY NOTES

12. SPONSORING MILITARY ACTIVITY
Naval Air Development Center
Warminster, Pa. 18974

13. ABSTRACT

The radiation patterns, in the elevation plane, of airborne antennas mounted on the aircraft fuselage have been analyzed by modern diffraction theory including wedge diffraction theory and creeping wave theory. It is found that the fuselage shape has a dominant effect on the elevation patterns. In order to analyze a general convex shape, a new approach, "section matching method", has been developed in which the fuselage profile is described by a set of points.

This new method is applied to some general geometrical shapes which approximate aircraft fuselage. The composite elliptical cylinder is the most general model considered. The validity of this method has been verified by modal and more rigorous GTD solutions.

DD FORM 1 JAN 64 1473

Unclassified
Security Classification

UNCLASSIFIED
Security Classification

14. KEY WORDS	LINK A ROLE	LINK A WT	LINK B ROLE	LINK B WT	LINK C ROLE	LINK C WT
Radiation pattern						
Elevation plane						
Wedge diffraction theory						
Creeping wave theory						
Fuselage-mounted antennas						
Section matching method						
Composite elliptical cylinder						

INSTRUCTIONS

1. ORIGINATING ACTIVITY: Enter the name and address of the contractor, subcontractor, grantee, Department of Defense activity or other organization *(corporate author)* issuing the report.

2a. REPORT SECURITY CLASSIFICATION: Enter the overall security classification of the report. Indicate whether "Restricted Data" is included. Marking is to be in accordance with appropriate security regulations.

2b. GROUP: Automatic downgrading is specified in DoD Directive 5200.10 and Armed Forces Industrial Manual. Enter the group number. Also, when applicable, show that optional markings have been used for Group 3 and Group 4 as authorized.

3. REPORT TITLE: Enter the complete report title in all capital letters. Titles in all cases should be unclassified. If a meaningful title cannot be selected without classification, show title classification in all capitals in parenthesis immediately following the title.

4. DESCRIPTIVE NOTES: If appropriate, enter the type of report, e.g., interim, progress, summary, annual, or final. Give the inclusive dates when a specific reporting period is covered.

5. AUTHOR(S): Enter the name(s) of author(s) as shown on or in the report. Enter last name, first name, middle initial. If military, show rank and branch of service. The name of the principal author is an absolute minimum requirement.

6. REPORT DATE: Enter the date of the report as day, month, year, or month, year. If more than one date appears on the report, use date of publication.

7a. TOTAL NUMBER OF PAGES: The total page count should follow normal pagination procedures, i.e., enter the number of pages containing information.

7b. NUMBER OF REFERENCES: Enter the total number of references cited in the report.

8a. CONTRACT OR GRANT NUMBER: If appropriate, enter the applicable number of the contract or grant under which the report was written.

8b, 8c, & 8d. PROJECT NUMBER: Enter the appropriate military department identification, such as project number, subproject number, system numbers, task number, etc.

9a. ORIGINATOR'S REPORT NUMBER(S): Enter the official report number by which the document will be identified and controlled by the originating activity. This number must be unique to this report.

9b. OTHER REPORT NUMBER(S): If the report has been assigned any other report numbers *(either by the originator or by the sponsor)*, also enter this number(s).

10. AVAILABILITY/LIMITATION NOTICES: Enter any limitations on further dissemination of the report, other than those imposed by security classification, using standard statements such as:

(1) "Qualified requesters may obtain copies of this report from DDC."

(2) "Foreign announcement and dissemination of this report by DDC is not authorized."

(3) "U. S. Government agencies may obtain copies of this report directly from DDC. Other qualified DDC users shall request through _____."

(4) "U. S. military agencies may obtain copies of this report directly from DDC. Other qualified users shall request through _____."

(5) "All distribution of this report is controlled. Qualified DDC users shall request through _____."

If the report has been furnished to the Office of Technical Services, Department of Commerce, for sale to the public, indicate this fact and enter the price, if known.

11. SUPPLEMENTARY NOTES: Use for additional explanatory notes.

12. SPONSORING MILITARY ACTIVITY: Enter the name of the departmental project office or laboratory sponsoring *(paying for)* the research and development. Include address.

13. ABSTRACT: Enter an abstract giving a brief and factual summary of the document indicative of the report, even though it may also appear elsewhere in the body of the technical report. If additional space is required, a continuation sheet shall be attached.

It is highly desirable that the abstract of classified reports be unclassified. Each paragraph of the abstract shall end with an indication of the military security classification of the information in the paragraph, represented as *(TS), (S), (C), or (U)*.

There is no limitation on the length of the abstract. However, the suggested length is from 150 to 225 words.

14. KEY WORDS: Key words are technically meaningful terms or short phrases that characterize a report and may be used as index entries for cataloging the report. Key words must be selected so that no security classification is required. Identifiers, such as equipment model designation, trade name, military project code name, geographic location, may be used as key words but will be followed by an indication of technical context. The assignment of links, rules, and weights is optional.

UNCLASSIFIED
Security Classification

DA

FILM

4